A PROGRAMMABLE LIQUID COLLIMATOR FOR BOTH CODED APERTURE ADAPTIVE IMAGING AND MULTIPLEXED COMPTON SCATTER TOMOGRAPHY

THESIS

Jack G. M. FitzGerald, 2d Lt, USAF

AFIT/NUCL/ENP/12-M01

DEPARTMENT OF THE AIR FORCE
AIR UNIVERSITY

AIR FORCE INSTITUTE OF TECHNOLOGY

Wright-Patterson Air Force Base, Ohio

DISTRIBUTION STATEMENT A

APPROVED FOR PUBLIC RELEASE; DISTRIBUTION UNLIMITED

A PROGRAMMABLE LIQUID COLLIMATOR FOR BOTH CODED
APERTURE ADAPTIVE IMAGING AND MULTIPLEXED COMPTON
SCATTER TOMOGRAPHY

THESIS

Presented to the Faculty

Department of Engineering Physics

Graduate School of Engineering and Management

Air Force Institute of Technology

Air University

Air Education and Training Command

in Partial Fulfillment of the Requirements for the

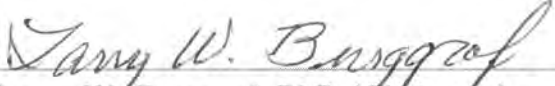Degree of Master of Science

Jack G. M. FitzGerald, BS

2d Lt, USAF

March 2012

A PROGRAMMABLE LIQUID COLLIMATOR FOR BOTH CODED APERTURE ADAPTIVE IMAGING AND MULTIPLEXED COMPTON SCATTER TOMOGRAPHY

Jack G. M. FitzGerald, BS
2d Lt, USAF

Approved:

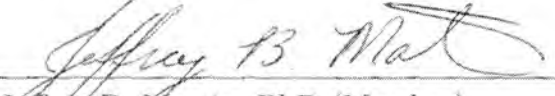|	
Larry W. Burggraf	*13 Mar 2012*
Larry W. Burggraf, PhD (Chairman)	Date
[signature]	*13 Mar 2012*
Maj Benjamin R. Kowash (Member)	Date
[signature]	*13 March 2012*
Jeffrey B. Martin, PhD (Member)	Date

AFIT/NUCL/ENP/12-M01

Abstract

A novel, fully reconfigurable collimator device for γ-ray and X-ray imaging was built and tested as a coded aperture. The device consisted of 10x10, 5x5x5 mm^3 chambers. Each chamber either was filled with an attenuating liquid, stopping photons, or evacuated of the attenuating liquid, allowing the photons to pass through. As the pattern of "on" and "off" chambers was manipulated, different, semi-independent views of the γ-ray source were found. Noise in reconstructed images decreased in all tests. Image reconstruction was performed with correlation methods and Maximum Likelihood Expectation Maximization (ML-EM). With ten mask patterns, the signal-to-noise ratio (SNR) in images of a Co-57 point source increased by a factor of 4.3 using correlation methods and by a factor of at least 50 using ML-EM. SNR in images of a Cd-109 source with high background increased by a factor of 3.0 using correlation methods and by a factor of 1.8 with ML-EM. Two extended sources were imaged, and the images improved when more masks were used. The Multiplexed Compton Scatter Tomography (MCST) forward problem using a PHDs Co high purity germanium (HPGe) detector was tested and evaluated. Potential applications are discussed in detail.

Acknowledgements

I welcome this opportunity to thank, first, my beautiful bride for all of her support and love during my time at AFIT. Secondly, I give thanks to my parents for raising me up into the man I am today. I thank my thesis advisor, my committee and involved faculty, most notably Dr. Larry Burggraf and Maj Benjamin Kowash. I am indebted to the men of the AFIT model shop, as well as to laboratory technician Eric Taylor. I would like to thank Daniel Ryan, specifically, for the weekends and unpaid overtime he put in to my project. A huge thanks to the PHDs Co for loaning us an extra HPGe strip detector to use for my work. They were the *de facto* sponsors of this project. Without their generosity my progress would have been severely hampered. Finally I extend my gratitude to my classmates, who have made this experience a fun one.

Above all, I humbly thank God, not only for creating a universe full of wonder and mystery, but for providing us with interesting problems worth solving. To Him be the glory.

<div align="right">Jack G. M. FitzGerald</div>

Table of Contents

List of Figures

List of Tables

List of Abbreviations

A PROGRAMMABLE LIQUID COLLIMATOR FOR BOTH CODED APERTURE ADAPTIVE IMAGING AND MULTIPLEXED COMPTON SCATTER TOMOGRAPHY

I. Introduction

1.1 Overture

Numerous scientific and engineering endeavors rely on the ability to image radioactive sources that emit high-energy photons, either X-rays or γ-rays. Detection of fissile material, nondestructive material testing, medical imaging and astronomy are a few notable examples. This paper focuses on γ-rays, although all of the principles and techniques are equally valid for X-rays, particularly hard X-rays. γ-ray imaging is difficult for two main reasons. First, significant depth is required to stop a given photon fully in order to measure the energy deposited. The mean free path in a detector can be longer than the detector's depth, resulting in low detection efficiency. The charge displaced by the incoming photons must be collected by equipment that can be bulky, increasing the overall size of the device. γ-ray detectors never will have the pixel density of a visible light detector. Secondly, high-energy photons cannot effectively be diffracted and focused by a lens. The wavelength is many orders of magnitude smaller than the characteristic sizes of a detection device. For photons above about 30 keV, diffraction may be ignored [27, 45].

Since the photons cannot be focused, they must be constrained in some other way. Often a pinhole collimator is used. A pinhole collimator is simply a small hole drilled into a sheet of high-Z material. When the pinhole collimator is placed between a γ-ray

source and a position-sensitive detector, all of the γ-rays are blocked except for those that pass through the pinhole. An inverted image is projected onto the detector. As the pinhole diameter decreases, the spatial resolution of the system increases. The image becomes sharper. However, decreased pinhole diameter also causes decreased throughput. A smaller pinhole corresponds to increased detection durations since a minimum number of detected photons are needed to form a good image.
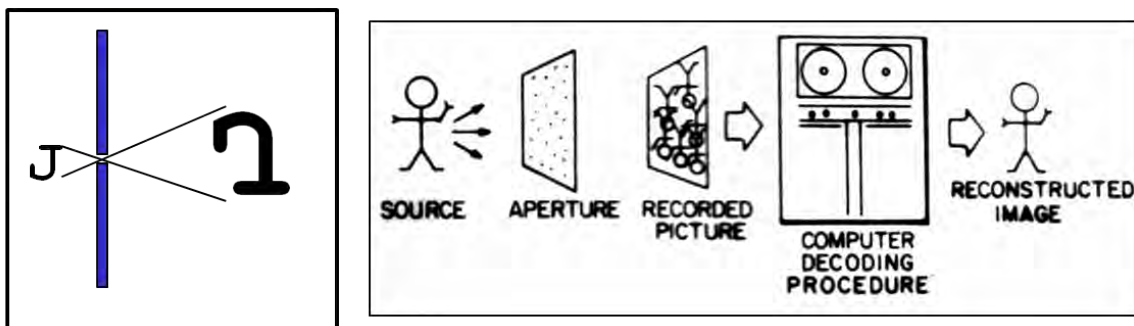
Figure 1. Left: A pinhole collimator. Right: Basic overview of the coded aperture imaging procedure [26].

One way to increase throughput, while maintaining good image resolution, is to drill more holes in the sheet of high-Z material. This is called a coded aperture. The raw data from the detector consists of the projections from each of the pinholes, all summed together. Knowing the positions of the pinholes relative to the detector, a computer routine can be used to unfold all of the projections and reconstruct an image of the source [21, 2]. The coded-aperture technique has been used successfully for many decades. The main drawback to the technique is that no computer routine can reconstruct an image of the source perfectly. All reconstruction routines introduce what is termed *inherent noise* to the final image. Some inherent noise is related to the pinhole positions whereas some inherent noise is randomly placed. In either case, if different mask patterns are used, and the reconstructed images from the different

2

patterns are summed together, the inherent noise will cancel out. Therein lies the purpose of the programmable collimator. By reconfiguring the coded-aperture during data collection, the inherent noise cancels out in the final image.

In 2010, at the Air Force Institute of Technology (AFIT), Dr. Larry Burggraf conceived of the programmable aperture collimator concept. Confirmation of a programmable collimator's feasibility and utility was provided by Maj Benjamin Kowash. They pictured a device that would use a liquid, high-Z metal to block γ-rays, juxtaposed with a low-Z plastic through which γ-rays could pass. If the high-Z metal and the low-Z plastic could be moved around relative to each other, incident γ-rays would be blocked in different patterns. To achieve this goal, a grid was drilled out of a 5x5x5 cm^3 steel block. Small plastic plugs were fabricated to snugly fit in to each grid chamber. The plugs are pushed or pulled back and forth in the chambers. From one side of the grid block, the liquid, high-Z metal is allowed to flow freely. By pushing the plug backward, the high-Z liquid metal is displaced from the chamber, leaving only air and plastic to attenuate a given γ-ray. If the plug is pulled forward in a given chamber, the chamber fills with the liquid metal so that γ-rays are blocked in that particular chamber. In effect this setup can be thought of as a 10x10 matrix, where each element of the matrix can be turned either "on" or "off" to γ-ray transmission.

Two potential uses for this device are presented in this document:

- Coded-Aperture Imaging: As mentioned above, a coded-aperture provides good throughput and resolution comparable to a pinhole collimator. The computer routine introduces noise into the reconstructed image. By using different pinhole configurations, or mask patterns, the noise and artifacts from the reconstruction process cancel out in the final image.

- Multiplexed Compton Scatter Tomography: A radionuclide and a γ-ray detector are placed on one side of a sample. γ-rays are Compton scattered within

a material of interest. The scattered γ-rays are collected by a position and energy sensitive detector. An image of the electron density in the sample is found, which is useful in nondestructive testing or medical imaging, especially bone density studies. The problem is ill-conditioned, and could benefit from constraints through physical collimation. Current commercial systems are highly collimated and examine one voxel in the sample at a time. By viewing multiple voxels simultaneously, acquisition time decreases and/or required source activity decreases.

1.2 Coded Aperture Application

The coded aperture system was first suggested by Dicke [21] and Ables [2] in 1968. X-ray astronomers had been seeking a system in which heavenly X-ray sources could be imaged with good resolution and in the shortest time possible. A pinhole collimator is used to increase the resolution of an X-ray camera system. The smaller the pinhole diameter is, the better the resolution will be. However, with a smaller pinhole the number of counts incident on the detector decreases. Dicke and Ables suggested that an array of pinhole collimators could be placed in front of the detector. The pinholes are small so as to provide good resolution. The greater quantity of pinholes increases the count rate. This pinhole array, or coded-aperture, can be configured in a variety of ways. As light from a source travels through the pinholes, it is cast onto the detector in a different way from each pinhole. Each pinhole causes a unique projection onto the detector. A computer must be used to interpret the data from the detector, unfolding all the pinhole projections to arrive at an image that reasonably recreates the original object. A coded aperture increases the Signal-to-Noise Ratio (SNR) of a standard detector [21]. The SNR advantage of the coded-aperture scheme

4

is most prominent with point sources and becomes less pronounced as more sources are placed in the Field-of-View (FOV).

Multiple coded-aperture mask configurations have been used to increase the fidelity of a reconstructed image [16]. Alternatively, the mask and/or detector can be moved to different locations around the object to increase the number of unique views. Prefabricated masks have been used for γ-ray coded-apertures, hitherto. Often tungsten is used, or other heavy metals such as lead. For γ-rays in the 100's to 1000's of keV, a coded-aperture thickness on the order of centimeters is required. The closed portions of the coded-aperture collimator must be thick enough to attenuate a large portion of the γ-rays. The programmable collimator of this study is a 10x10 array, where each array element can be turned "on," meaning that γ-rays are allowed through, or "off," meaning that γ-rays are attenuated. The ability to configure the collimator in different ways allows for multiple, semi-independent views to be made of the object, increasing image fidelity over a given, total measurement time.

As a dynamic coded-aperture, the programmable collimator has many potential applications in the Department of Defense (DoD) and elsewhere. These applications are discussed further in Sections 2.6.5 and 6.2.6.

- The programmable collimator could be mated with a position and energy sensitive detector and employed as an imaging γ-ray detector on an unmanned, ground-based robot or aerial vehicle. The SNR advantage from the coded-aperture technique would be advantageous in environments where a source is either weak or shielded. A vehicle of this type could survey large areas after a nuclear attack or a nuclear reactor accident, as well as find certain radioactive nuclides in effluents for treaty monitoring applications.

- A passive sensor could continuously search for radioactive material in passing vehicles at ports, gates, etc.

- The lessons learned from programmable collimation could be applied to surveillance satellites. A future system might consist of a number of detectors, placed on one satellite or several satellites, watching the Earth for nuclear events. The same research conducted for choosing the best mask sequence for the programmable collimator is applicable to space surveillance systems.

- The device could allow for more effective γ-ray or X-ray, space-based astronomy. Coded-apertures have a long history with astronomy. Sometimes SNR is increased by spinning the satellite. Programmable collimation removes the need to spin, since spinning can introduce difficulties in satellite design.

- Medical tomographical imaging could be improved by increasing image quality and/or decreasing the radioactive dose given to patients.

- The device could be used to give position sensitivity to a position-*in*sensitive detector. Such functionality has been explored with Rotating Mask Collimators (RMC) mated with Sodium Iodide (NaI) detectors [74]. A programmable collimator/NaI system would be cheaper than most energy and position sensitive detectors. Such a system could be used in any of the applications mentioned above, among others.

1.3 Multiplexed Compton Scatter Tomography Application

Another type of application for the programmable collimator is the improvement of Multiplexed Compton Scatter Tomography (MCST). MCST was first investigated at AFIT by Brian Evans and Matt Lange in research advised by Professors Jeffrey Martin and Larry Burggraf [25, 41]. That research demonstrated multiplexed imaging in a single discretized slice of material. MCST is a methodology for one-sided non-destructive investigation of materials. It differs from other tomographic techniques

because the source and detector can be placed on the same side of the object, rather than on opposite sides. In many industrial cases, access to opposite sides of the object to be imaged is not available. MCST could be applied effectively toward the detection of cracks and structural failures in airfoils, composite structures, and other aircraft systems. MCST also could be used for improved medical tomography. Probably it would complement existing tomographic techniques, like Computed Tomography (CT) or Positron Emission Tomography (PET), allowing for better resolution and/or a lower total dose to patients. In MCST, a monoenergetic radionuclide is placed near an object, beside a position and energy sensitive detector. Shielding is placed between the source and detector. Photons emitted by the source are Compton scattered in the sample. Some of these scattered photons are detected. By knowing the position and energy of the received photons, spatial and compositional information about the sample is ascertained. MCST is well suited for two-dimensional applications. The programmable collimator would serve to produce three-dimensional images by constraining the highly multiplexed problem, allowing for solutions to be found quickly and accurately.

1.4   Research Goals

The goal of this research was the characterization of the programmable collimator given the coded-aperture and MCST setups. To the best knowledge of the author and his committee, a liquid metal never has been used to attenuate γ-rays in quickly programmable patterns. An evaluation of the viability of this device for different applications was wanted. Recommendations from this proof-of-concept study will be used to direct future investigations into programmable collimation.

II. Theory and Background

2.1   Coded-Aperture Theory

The coded aperture system was first suggested by Dicke and Ables in 1968 [21, 2].
In γ-ray imaging, a single pinhole collimator is used to increase the resolution of a
detector. With coded apertures the single pinhole is replaced by numerous pinholes
in an array. As high-energy light shines upon the array, each pinhole causes a unique
projection onto a spatially-sensitive detector. Knowing the configuration of the pin-
hole array, mathematical techniques are used to unfold all the projected images from
each other, reconstructing the original image. The term *multiplex advantage* is used
to describe the greater SNR in reconstructed images produced by a coded-aperture
array versus those from a single pinhole (SNR is explained thoroughly in Section
5.3). For point sources the SNR improvement goes roughly as $\sqrt{N}$, where N is the
number of pinholes [21]. As more point sources are imaged, the multiplex advantage
decreases. A coded-aperture works better for point sources than for extended sources.

Coded-aperture problems usually are approximated as three parallel planes. Fen-
imore and Cannon outlined a basic coded-aperture methodology in their 1978 paper
[26]. The sources exist in the object plane, O. The radiation moves through a col-
limator in the aperture plane, A, where A is the mask pattern. The light moving
through the aperture plane is projected onto the detector or picture plane, P, given
by

$$P = (O * A) + N \tag{1}$$

As with all real detector experiments, noise, N, always is summed with the true
signal and must be considered. Sources of noise include, but are not limited to, low
counting statistics, background scattering, transmission through closed portions of
the array, imprecisions in the detector and electronics noise. In most applications, all

three planes are discretized into two-dimensional matrices. Notice that O is convolved with A in Equation 1, where $*$ is the convolution operator. An estimate of the object, $\hat{O}$, can easily be found as

$$\hat{O} = R\mathcal{F}^{-1}\left[\frac{\mathcal{F}(P)}{\mathcal{F}(A)}\right] \tag{2}$$

where $\mathcal{F}$ is the Fourier transform and R is the reflection operator. This method is typically flawed, because $\mathcal{F}(A)$ contains regions of frequency with small magnitudes. In these regions the true signal easily is lost in the noise. Woods *et al.* showed that deconvolution techniques can be used in conjunction with a two-dimensional Wiener filter [77]. Often correlation techniques are preferred. Here $\star$ is the correlation operator. *Matched filtering* is another term used to describe correlation decoding.

In the correlation methodology, the object reconstruction is defined as

$$\begin{aligned}
\hat{O} &= P \star G \\
&= RO \star (A \star G) + N \star G
\end{aligned} \tag{3}$$

G is called the postprocessing array, or matched filter, and is only a mathematical construct. It does not exist physically. G is chosen such that $A \star G$ approximates a two-dimensional Dirac δ-function. If this δ-function were perfect, the object estimate would reduce to

$$\hat{O} = O + (N \star G) \tag{4}$$

Notice that the noise cannot be removed from the estimated object. Unfortunately, $A \star G$ will deviate from a true δ-function in any real application, introducing artifacts into the estimated object.

In the original astronomy application, a point source is assumed to be infinitely far away. A star is much more distant than the scale of the detector apparatus. If the source is at infinity, the aperture pattern is projected onto the detector plane at the

9
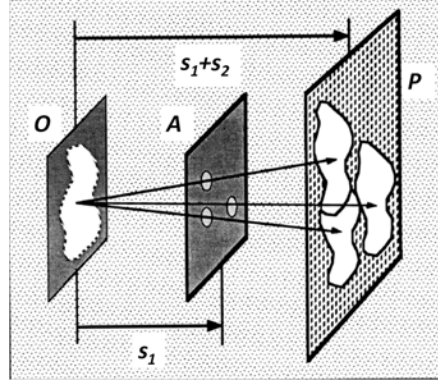
Figure 2. Planar approximation of the coded-aperture problem. Adapted from [65].

same scale. However, in most defense and medical applications, the source cannot be assumed to be located at infinity. Rather, a magnification effect will exist, and must be considered. The magnification factor, m, is given as:

$$m = \frac{s_1 + s_2}{s_1} \qquad (5)$$

where s_1 is the distance between the object and the aperture planes and s_2 is the distance between the aperture and detector planes, as shown in Figure 2. In near-field applications, it is conceivable that the magnification could be used to determine the distance of the source from the detector. Information about the source's location in all three dimensions could possibly be gathered by factoring in the effect of magnification.

2.2   Mask Configurations

A number of different coded-aperture collimator designs have been employed in the past, each with its own advantages. Fresnel zone plates, annuli, and Fourier apertures can be used as coded-apertures [9]. The programmable collimator falls under the broad pinhole-array category. The term "pinhole" is used here somewhat loosely as any small round or square aperture. Each element of the programmable collimator is

shaped as a 5x5 mm^2 hole, for instance. Square holes are easy to manufacture, and thus are fairly common. Hexagonal holes also have been organized into a honeycomb pattern and used successfully [17].

The first pinhole array design considered is called the random array and was suggested in Dicke's original paper [21]. Any number of pinholes can be opened, with varying results. Often 50% of the array elements are opened, as is the case in Figure 3. An initial guess for the matched filter, G, could be the matrix A itself. Since a source projects an identical shadow of the aperture pattern onto the detector, this is a reasonable first guess. However, recall that the term $A \star G$ should approach a δ-function as nearly as is possible. If A is used for G, a distinct triangular base is formed in the correlation (Figure 3). Anytime that the sidelobes of the correlation deviate from zero, artifacts are introduced into the object estimate, $\hat{O}$.
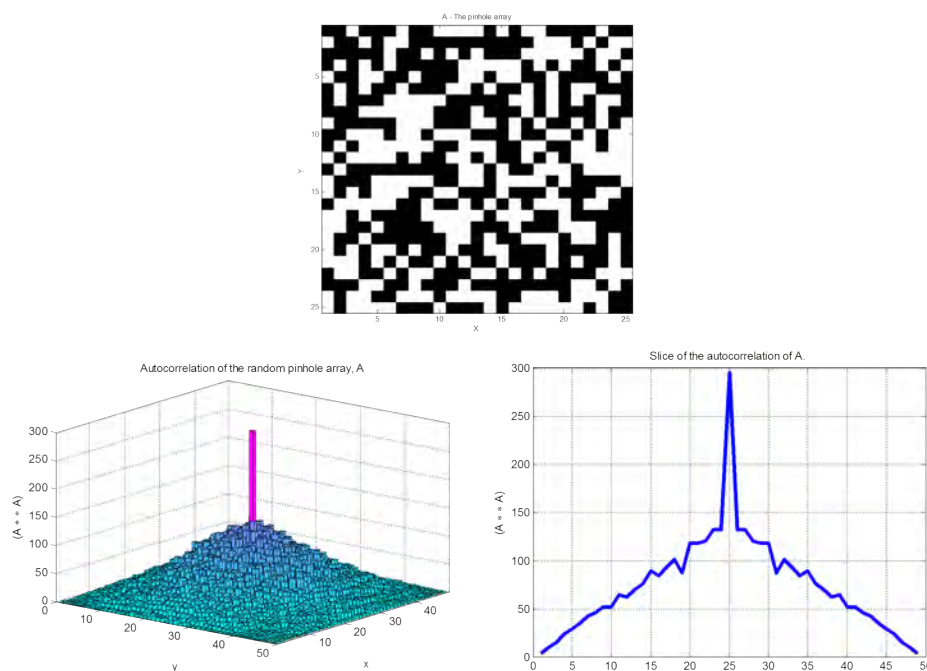
Figure 3. Top: A random pinhole array, A. Bottom-Left: The autocorrelation of the pinhole array, A. Bottom-Right: A slice in one dimension of the autocorrelation of A.

Of course, G is nothing but a mathematical abstraction, and can be altered in any way desired. With this idea in mind, C. Brown suggested that the anti-mask should be allowed to take on negative values [10]. Namely, the zeros in the mask are replaced with "-1's", or

$$
\begin{aligned}
G(i,j) & = \quad 1 \text{ if } A(i,j) = 1 \\
& = \quad -1 \text{ if } A(i,j) = 0
\end{aligned}
\tag{6}
$$

where i and j are row and column indices, respectively. In the mask, A, a value of "1" corresponds to an open element where γ-rays are allowed through, whereas a value of "0" corresponds to closed elements, where γ-rays are blocked.
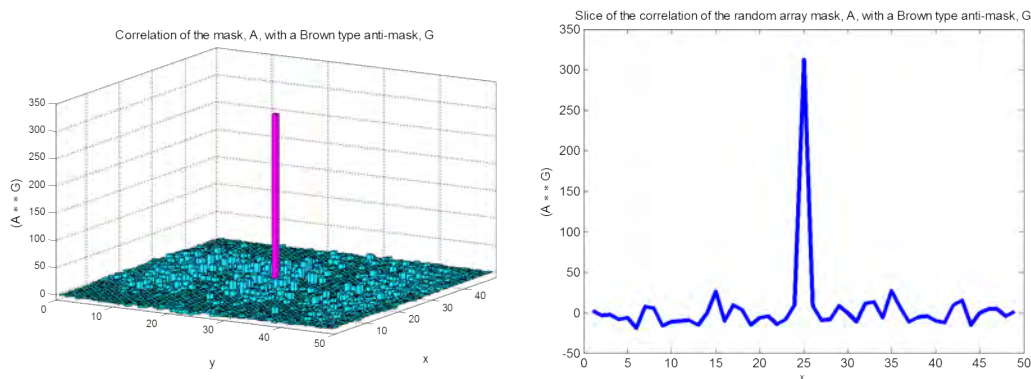
Figure 4. Left: The correlation of A from Figure 3, with its Brown anti-mask, G. G is constructed by replacing the zeros in A with "-1's". Right: A 2D slice of the 3D $A \star \star G$ plot.

The Brown anti-mask improves the $A \star G$ term. The triangular base is removed, causing the term to approximate a δ-function more closely. Note that the inclusion of negative values in the anti-mask causes negative values in the $A \star G$ array. This can result in non-physical artifacts in $\hat{O}$, though the advantage of the removed triangular base typically outweighs the disadvantage of these artifacts.

12

Another mask configuration is called the Uniformly Redundant Array (URA). A subset of this mask class is the Modified Uniformly Redundant Array (MURA). URA's were studied extensively by Fenimore and Cannon [26]. In an extension of Calabro and Wolf's work, they define the aperture plane as an infinite mosaic of repeating, pseudonoise arrays [12]. The basic array has dimensions of r and s where r and s are both prime numbers and $r = s + 2$. The basic array, $A(I, J)$ is defined as

$$
\begin{aligned}
A(I, J) &= 0 \text{ if } I = 0, \\
&= 1 \text{ if } J = 0 \text{ and } I \neq 0, \\
&= 1 \text{ if } C_r(I)C_s(J) = 1, \\
&= 0 \text{ otherwise}
\end{aligned}
\tag{7}
$$

where I and J are row and column indices of the basic array, respectively, and

$$
\begin{aligned}
C_\alpha(\beta) &= 1 \quad \text{if there exists an integer } x, 1 \leq x < \alpha \\
&\qquad \text{such that } I = \text{mod}_\alpha x^2 \\
&= -1 \quad \text{otherwise}
\end{aligned}
\tag{8}
$$

where α can be r or s and β can be I or J. Physical coded-apertures cannot be infinite, but instead are a finite cutout of the infinite mosaic. Figure 5 shows a coded-aperture, A, of size $2r$ x $2s$, where $r = 19$ and $s = 17$. G, the Brown matched filter, was found as in Equation 6.

A discrete correlation always doubles the size of the output matrix as compared to the input matrices. The center square of the correlation is the only part used in the image reconstruction process. The additional spikes in $(A \star G)$ arise from the repetition of the basic array within A. The URA has been shown to outperform the random array in most cases, when correlation methods are used [5, 26]. Unfortunately, the programmable collimator is not equipped with sufficient elements for a proper

URA/MURA pattern. Technically one could be formed, but whether the resulting matrix could be classified as a URA would be disputable. As such, random arrays will be focused upon with the programmable collimator. On top of all this, URA/MURAs are not necessarily more effective for ML-EM methods.
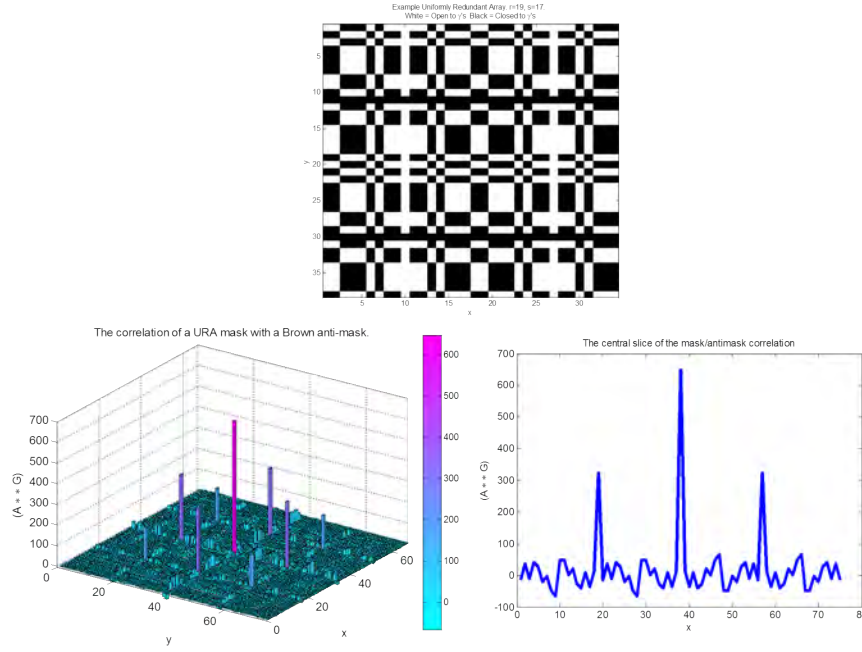
Figure 5. Top: An example URA, A, where r=19, s=17 and A is 2r x 2s. Bottom-Left: The correlation of the URA mask, A, with the Brown anti-mask, G. Bottom-Right: The central slice of the correlation between A and G. [38]

Note that the above figures do not have any noise included. The portions in the plots of $(A \star G)$ that appear to be noise are instead artifacts of the correlation process. If the A and G planes approach infinite extent in space, the artifacts would diminish to zero. These artifacts often are termed *inherent noise*. The choice of aperture pattern and matched filter pattern should be made so as to diminish the inherent noise as much as possible.

2.3 Reconfiguring the Mask

The primary advantage of the programmable collimator is its ability to be reconfigured. Multiple "views" are desired of the imaged object. A number of different, unique projections of an object will increase the fidelity of the final, reconstructed image. This can be achieved in a variety of different ways. In some cases, the coded-aperture mask and/or detector is rotated, giving multiple views of the object [17]. Often, in this case, hexagonal arrays are used, being more conducive to rotational transformations about the center axis of the mask. In the satellite application, this sort of rotation adds complexity to the satellite system. The entire satellite must rotate, perhaps causing problems with other systems. In ground-based applications, the requirement of rotation implies additional actuators to make the whole system rotate.

In other tests, the coded-aperture mask pattern was altered by sliding a pattern cut from tungsten in one dimension and only allowing a portion of the pattern to let radiation through [71, 16]. For example, a 10 x 20 pattern could be cut from the tungsten. Lead could be used to ensure that only a square of size 10 x 10 would be open. The pattern could be slid in the long direction, allowing for ten mask patterns. Such a design was suggested as a way to combat the incomplete attenuation of photons in the closed portions of a coded-aperture pattern, which becomes a greater factor with higher energy γ-rays. The programmable collimator is an improvement over this sort of design in that it can produce any possible pattern, therefore allowing for "views" that are more independent from each other.

Another means for gaining multiple views of the object is either to rotate the object or to rotate the coded-aperture/detector system around the object. The latter method is recognizable as a staple CT technique. This sort of rotation is especially well suited for three-dimensional imaging, or tomography. The disadvantages are
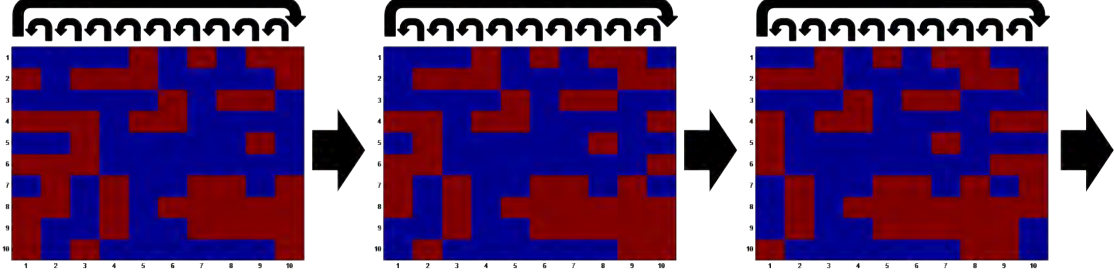
Figure 6. A time-coded pinhole array, in the style of Clinthorne *et al.* [16]. The columns are shifted once leftward in each subsequent array.

similar to those enumerated previously, namely the additional mechanical complexity of a rotating system. Furthermore, the rotation can cause problems for iterative reconstruction algorithms, like ML-EM. Such techniques require the pixel size in the object be fixed so that the relationship between the object and the projections is tractable [33].

With the programmable collimator, no rotation is necessary. Semi-independent views are gained by changing the mask configuration. Thus, the collimator and detector can stay in the same position relative to the object. Or the programmable collimator could be conjoined with current methods, making them better.

Though not investigated in this work, a future programmable collimator imaging system might be able to incorporate incoming data in order to choose the best patterns for the remainder of the data run. Aperture patterns would be chosen on the fly. After the first 1-2 arbitrary mask patterns were used, the system would have a good idea of where the source is located. It could then choose the proper patterns so as to narrow in on the source. The system could start with a high pinhole density, allowing maximum throughput with lower resolution. As the source becomes visible, the pinhole density would decrease, resulting in a sharper image in a shorter duration.

16

2.4 The Maximum Likelihood Expectation Maximization Algorithm

Matched filter and correlation techniques are the traditional means for analyzing data from a coded-aperture system. A more modern and effective method, called the Maximum Likelihood Expectation Maximization (ML-EM) technique, has been used for several decades in medical imaging [61]. In ML-EM, an accurate forward model must first be devised. Good predictions of the detector response are required, given mask position and configuration, source type, source location, etc. The more accurate the forward model is, the better the results given by the ML-EM method will be. The forward model could even be created experimentally, by carefully setting up a source-mask-detector system and measuring all of the relevant parameters. This approach is rarely practical. Instead, computer models typically are used as the forward model, sometimes incorporating real-world data.

The forward model is used to define the ML-EM variable A. The forward model deals with two sets of spatial locations, being the detector plane and the source plane. The detector is discretized into N pixels. The source plane is discretized into M pixels. In more advanced versions, the source region could be split into three-dimensional voxels. In this study, only 2D pixels are considered. The purpose of the forward model is to predict the number of counts that would be recorded by a given detector pixel if the source were located at a given source plane pixel. The model should incorporate as many physical processes as possible, such as inverse squared geometric attenuation, material attenuation and the location and configuration of the coded-aperture mask. More advanced models might include Compton scatter, heterogeneous efficiencies among detector strips (and within detector strips), and so forth. The goal of the forward model is to fill in an NxM matrix named $\mathbf{A}$, where A_{ij} is the predicted response of detector pixel i if the source were located at source plane pixel j (See Section 3.1). The values of the elements of $\mathbf{A}$ can be thought of loosely as

17

the expected number of counts. However, **A** must be normalized before being used. The most appropriate way to consider A_{ij} is as the probability that a photon emitted from a source at location j is detected by detector pixel i. **A** is precomputed and is used in the ML-EM algorithm.

Once **A** is computed, the ML-EM iterative sequence is performed. Besides **A**, the algorithm requires a few other vectors. $\vec{y}$ is a length N column vector that contains the real data from an experiment. That is, y_i is the number of counts recorded by detector pixel i. $\vec{\lambda}$ is the object/source estimate and is the output of the algorithm. $\vec{\lambda}$ is a length M column vector, where λ_j is the probability that the source was located at source plane pixel j. b is an additive noise term and represents the probability that a detected photon is attributable to background or Compton scattering. The single equation of the ML-EM algorithm is [53, 40, 62]:

$$\lambda_j^{\texttt{new}} = \frac{\lambda_j^{\texttt{old}}}{\sum_i A_{ij}} \sum_i A_{ij} \frac{y_i}{\sum_k A_{ik}\lambda_k + b} \tag{9}$$

In MATLAB® this is written as:

$$\vec{\lambda}_{\texttt{new}} = \vec{\lambda}_{\texttt{old}} \mathbin{.\!*} \left[\mathbf{A} * \left\{ \vec{y} \mathbin{./} \left(\mathbf{A} * \vec{\lambda} + b \right) \right\} \right] \mathbin{./} a \tag{10}$$

where a is a normalization factor for **A**, found by multiplying the inverse of **A** by a length N ones vector. To perform the ML-EM algorithm, every element of λ is first set to "1." In other words the source has an equal probability of being anywhere before the algorithm begins. The code then continues to loop Equation 9. After the equation is evaluated in each loop, $\vec{\lambda}_{\texttt{old}}$ is set to $\vec{\lambda}_{\texttt{new}}$. The ML-EM equation compares the real data to the predictions, morphing λ with each iteration to make the best agreement between the prediction and reality. There is no set way to determine the minimum number of iterations necessary. It must be determined empirically for any

given problem. It is possible to perform too many iterations (Section 5.2), in some cases. Weak regions can be lost when too many iterations are performed. The user must find the proper number of iterations in order to reach convergence without losing weak regions.

2.5 Multiplexed Compton Scatter Tomography

Multiplexed Compton Scatter Tomography (MCST) has been explored previously at the Air Force Institute of Technology (AFIT). Brian Evans and Matt Lange, in research advised by Professors Jeffrey Martin and Larry Burggraf, looked at defects in thin aluminum airfoils [25, 41]. Evans used six HPGe detectors and collimated the scattered photons down to a two-dimensional slice. MCST, in that case, would be useful in detecting cracks that develop around rivets on aircraft. Marc Sands used MCST to image a phantom representing a wrist bone [59]. Noninvasive bone density measurements would be useful for the medical characterization of osteoporosis in patients. Sand's MCST system was able to differentiate between normal, osteoporotic, and void bone densities.

MCST is a nondestructive inspection technique whereby an object's near-surface interior structure may be discerned. In MCST, high energy photons shine into an object. By detecting the photons that Compton scatter back toward the detector, information about the elements within the object is found. This technique differs from computed tomography (CT) where the object is placed between the source and the detector and the attenuation through the object is found. With MCST, the source and the detector are located on the same side of the object. The CT-type setup is not always possible.

MCST takes advantage of the fact that the energy of a Compton scattered photon is angle dependent. Furthermore, the cross section for scatter depends on the electron

density, and thus the atomic number, of the scattering element in question. Compton scattering is governed by the Klein-Nishina equation [37]

$$
\begin{aligned}
\frac{d\sigma}{d\Omega} &= Zr_0^2 \left(\frac{1}{1+\alpha(1-\beta)} \right)^2 \left(\frac{1+\beta^2}{2} \right) \left(1 + \frac{\alpha^2(1-\beta)^2}{(1+\beta^2)[1+\alpha(1-\beta)]} \right) \\
\beta &= \cos\theta
\end{aligned}
\tag{11}
$$

where σ is the cross section for scattering, in barns, r_0 is the classical electron radius, θ is the scattering angle, Ω is the solid angle into a given detector pixel, and $\alpha = E/m_0c^2$. The experimenter is most interested in finding the Z of the material, and thus must integrate over the solid angle, which is often θ dependent. In MCST, the experimenter gets a response in each detector pixel. From an ideal point sample, this response would be a δ-function at a certain energy, multiplied to a certain count height. The energy of the scattered photon is given by the Compton formula [37]:

$$
E' = \frac{E}{1 + \frac{E}{m_0c^2}(1 - \cos\theta)}
\tag{12}
$$

where E and E' are the energy of a photon before and after Compton scattering, respectively. By looking at the energy of the detected photon, and by knowing the initial energy from a monoenergetic source, the angle of scattering can be deduced. The number of counts received by each detector pixel would also be known, which is directly proportional to the cross section for scattering. Given all this knowledge, the electron density of the material point is found. From electron density, atomic number can follow.

Note that the Compton equation assumes that the photon scatters off of an initially stationary electron. In reality the electrons are moving about the atoms at significant speeds. Depending on how a given electron is moving relative to the detector, the scattered energy can be more or less than that given by the Compton

formula. This effect is called Doppler broadening, and serves to widen the detector response peaks. Doppler broadening in MCST problems has been characterized previously [25, 41].
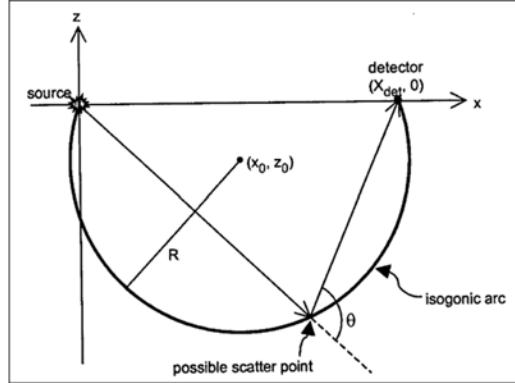
Figure 7. By knowing the source and detector positions, as well as the initial and scattered energy of a single photon, an isogonic arc of possible scatter locations is found [25].

From a measured, Compton scattered photon, an infinitesimal point in the sample is not deduced, but rather the scattered angle into the detector. For an individual, detected photon, only an isogonic arc of possible locations in the sample where the scattering angle is θ is known. Various techniques can be used to discern the point at which the scattered photon originated, rather than the isogonic arc. Collimation can limit the field of view into each detector pixel, chopping the isogonic arc into small pieces. By changing the collimation, by using more detectors, and by changing the source-object-detector geometry, the true point of scatter can be determined from all the different isogonic arcs. The isogonic arcs are similar to the straight line projections of attenuation in computed tomography. Evans and Lange observed that the electron density would bleed from high density regions to low density regions as the reconstruction routine was iterated. The line between high and low electron density regions in a given phantom would thus appear blurred in the final, reconstructed

image. Collimation causes the reconstruction routine to be more stable, reducing this bleeding effect.

Perhaps the greatest hindrance to MCST is the fact that γ-rays are attenuated in the object before and after being scattered. This effect alters the counted events in the detector as compared to a model that only includes Compton scattering. In nondestructive testing, the composition of an object being imaged is obviously not known, meaning that the attenuation through the object is unknown. Several methods have been investigated for overcoming the problem of attenuation. Lale *et al.* ignored attenuation altogether, assuming that higher energy γ-rays (5.6 MeV and 1.25 MeV, respectively) would be negligibly attenuated [39, 15]. Prettyman *et al.* incorporated information from a traditional, transmission imaging setup, combined synergistically with a Compton scatter tomography setup [56]. Such a technique would certainly be viable in medical imaging applications where attenuation information is already be known. However, a standalone system could be required, especially in industrial applications where access to only one side of an object is given. With such constraints iterative techniques must be used, such as those which were first rigorously developed by Hussein *et al.* and Arendtsz [36, 7]. Regularization methods are used to solve the problem, such as the ML-EM and Penalized Weighted Least Squares (PWLS) methods. Evans utilized the PWLS method in his work and developed a Fortran code for its execution [25].

A group from France is showing some interest in Compton scatter tomography for medical applications [51, 52, 23, 22]. They expand upon a method called the Compounded Conical Radon Transform, a form of filtered backprojection. This methodology may be useful in further AFIT work on MCST. Unfortunately, they assume that attenuation in the medium is negligible. Earlier, Arendtsz argued that attenuation in the scattering medium is the greatest stumbling block to MCST [7]. Nevertheless, the

Compounded Conical Radon Transform method is worth note. They examine some iterative methods, as well. They simulate both collimated and uncollimated MCST systems in their work. Their work is done with the Single Photon Emission Computed Tomography (SPECT) application in mind, making theirs a subtly different problem than the MCST problem investigated here.

B. Guerin and G. El Fakhri of the Massachusetts General Hospital and the Harvard Medical School, respectively, argue that energy data already present in PET scans can be used for Compton scatter compensation [28]. Specifically, the Cerium-doped Lutetium Yttrium Orthosilicate (LYSO) crystals used in PET have better energy resolution than the formerly used Bismuth Germinate (BGO) crystals. The 11.5% resolution of the LYSO crystals would not be adequate for good MCST spatial resolution (See Figure 19). This group uses the data to correct for Compton scatter corruption in the PET data. They do not use the data in a standalone manner, but rather to correct blur in the standard PET image.

An ideal Compton scatter imaging device would consist of an uncollimated source that shines photons upon the entire object and an uncollimated detector array which views the entire object at once. Such a problem would be highly multiplexed. The signals from photons that are scattered in all the voxels of the object would be convolved together. As the problem becomes more multiplexed, numerical instabilities cause the reconstruction method to fail. The multiplexed problem is ill-conditioned.

Commercial devices are in use that perform Compton scatter imaging. One such device, called COMSCAN, uses an X-ray generator and measures the backscattered photons [66]. This device is able to overcome the mathematical issues of the Compton scatter problem by highly collimating both the source and the detectors, as seen in Figure 8. The device physically moves, examining one voxel in the object at a time. In 2010, this particular device was successfully used to analyze historic artifacts,
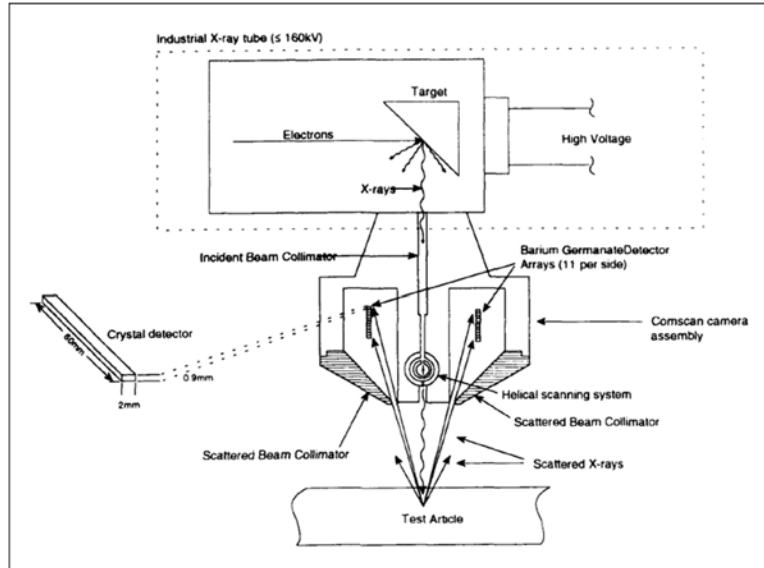
Figure 8. A diagram of the COMSCAN system, a commercially available device which uses Compton scatter X-rays [66].

including a fresco, and Egyptian mummy, and a medieval clasp [30]. It was found that Compton scatter imaging was useful for imaging objects of large size and/or high density. In either of those cases, too few X-rays would transmit through the object in order to use conventional X-ray imaging techniques.

Compton scatter imaging has been used for security applications, to scan personnel and equipment at airports, ports, etc. The full body, X-ray backscatter scanners used at airports (infamous for their ability to see through clothes) use low energy X-rays that can barely penetrate the body. This system is also highly collimated, like the COMSCAN system [8].

The highly collimated method is not ideal for the medical application, because the dose given to the patient could be unsatisfactorily high. Unlike with the airport full-body scanner, medical X-rays would have to be of a high enough energy to penetrate the body. A slow scan through the body with high energy X-rays would result in too high of a dose. Thus, multiplexing and lesser collimation would be useful. In

the industrial application the current systems are usable, but if multiplexing were incorporated then scan-time would decrease dramatically.

2.6   Other Applications

2.6.1   Unmanned robots or UAVs

Unmanned Aerial Vehicles (UAV) and unmanned robots are becoming increasingly popular in the DoD. The idea of placing a position-sensitive γ-ray detector on one of these vehicles is a promising one. Already, Sodium Iodide (NaI) scintillator crystals have been placed aboard small aircraft in order to detect uranium, thorium, and potassium over a wide area of land [43]. Position sensitivity is achieved by flying over a large area. If the detector aboard the aircraft was position-sensitive, then required flight times and distances would be reduced. A similar application would be to place a position-sensitive detector on a ground-based robot.

These types of vehicles are not likely to help in preventing a nuclear attack. Neither uranium nor plutonium is very active, meaning that there would be few γ-rays to detect, especially from long distances. Furthermore, a nuclear weapon would probably be encased in lead or tungsten shielding to prevent its detection by γ-rays. The best application for unmanned vehicles is the detection of radioactive material after a nuclear reactor accident or a nuclear weapon detonation [70]. Whether by a nuclear detonation or a nuclear reactor accident, highly radioactive substances could be dispelled over a large area of land. Unmanned vehicles can easily traverse radioactive areas, sending back readings. These readings would give valuable data to decision-makers regarding evacuations and movement of responders and military personnel. Also, collection of radioactive effluents is an important component of several treaty-monitoring organizations. A position-sensitive system would help to guide members of these organizations toward the locations where radioactive effluent content is highest.

Lastly, a position-sensitive detector would be useful inside of a running reactor facility in order to detect leaks.

2.6.2 Space Surveillance

Since the 1960s, the United States has launched numerous satellites with the ability to detect γ-rays emitted from terrestrial sources [73]. These satellites are particularly well-suited to detect the γ-rays from nuclear detonations. The satellites are used to ensure that other nations are adhering to their treaty obligations, especially with regard to nuclear weapon tests. Better position-sensitive γ-ray detectors could locate the source of the γ-rays with better resolution.

2.6.3 Space-based Gamma-Ray Astronomy

Worldwide, over eighty satellites have been launched with γ-ray detection capabilities. A good list of all the satellites that have been used for γ-ray astronomy can be found at the NASA website [46]. γ-ray detectors are used to investigate solar flares and supernova events [31]. Perhaps the most significant use, currently, is the detection of Gamma-Ray Bursts (GRB). GRBs are the most intense electromagnetic events in the universe. There is still not a full consensus as to the origin of GRBs, though it is generally thought that GRBs are caused by supernovae or neutron star creation events in distant galaxies [72]. GRBs last from between less than a second to several minutes. Typical durations are from 20-40 seconds.

Current satellites systems used in γ-ray imaging can be large, heavy, and expensive. The Compton Gamma-Ray Observatory (CGRO), for instance, weighed a whopping 17 tons. Perhaps a better approach to γ-ray astronomy would be to deploy a greater number of small, inexpensive satellites. Cubesat and Nanosat technology is becoming increasingly popular [18]. Position-sensitive γ-ray detectors could be placed

on a large number of small satellites. These satellites could be used to observe a large area of the sky. The satellites could also be used in a large array configuration, all of them pointed with the same field-of-view, in order to increase image resolution of stellar γ-ray sources.

Coded-apertures have successfully been used on satellites for γ-ray astronomy [60, 54, 49]. One possible way to increase the views given to the satellite, thus decreasing inherent noise, is to spin the satellite [32, 1]. Spinning the satellite introduces several complexities in satellite control, communications, and solar power acquisition.

2.6.4 Medical Nuclear Imaging

Many researchers have investigated coded-apertures for medical applications. Numerous nuclear medical spheres have been considered, including Single Photon Emission Tomography (SPECT), Positron Emission Tomography (PET) and Computed Tomography (CT) [5, 33, 47, 65, 42, 14]. Often the thyroid phantom is used as a gauge for the effectiveness of a given system [3]. Small animals and capillary tubes have also been imaged [4, 50]. Methods for decoding include correlation methods, ML-EM, and PWLS. Coded-apertures are most useful in cases where a γ-emitting radionuclide (typcially Tc-99m) is injected into the body or ingested by the patient. Prominent issues in medical imaging are the limited doses that can be administered to patients, limitations on how close a detector can be placed to source, and movement of the patient over time. Coded-apertures are less successful in the CT case, where the source and the detector are placed on opposite sides of the body, and varying spatial attenuation in the patient's body causes spatially varying strength of the X-rays. Different methods have been employed to account for vignetting effects.

2.6.5 Position Sensitivity from a Single Detector Crystal

There are a number of dynamic collimators that have been considered in the past. Some examples, in addition to coded-apertures, are the fresnel zone plate, the rotating slit collimator, the stochastic aperture, and the Fourier aperture [9]. These apertures can be modulated in time in order to gain different views of the source.

A rotating mask collimator has been successfully mated with a NaI detector, giving position sensitivity to the single crystal [74]. The time-dependent signal given by the detector is compared to the known, time-dependent modulation of the collimator. Since the problem is constrained in a known, repetitive way, information about the location and strength of the source can be deduced.

III. Computer Modeling

3.1 Coded Aperture Ray Tracing Forward Model for ML-EM

A model was created in MATLAB® to calculate the coded-aperture forward problem. The term *forward problem* is used to describe the situation in which the location, size, activity, and other relevant parameters of the source plane are known and the detector response is measured. The forward model process is the opposite of the image reconstruction process (or *inverse problem*) in which the detector response is known and the source plane must be characterized. The forward model helps in image reconstruction.

This model utilizes the coordinates shown in Figure 15. First, three relevant coordinates are specified, being the location of a point source, the location of the programmable collimator and the location of the detector (which is set as the origin). The mask pattern is input, from which the collimator is constructed virtually, in three dimensions. Two planes are defined, being the front and back of the collimator. On each plane, a 10 x 10 grid is carved out, representing the fronts and backs of the chambers of the collimator. The size of the detector crystal and the size of the source plane also can be set. The resolution of the source and the detector planes are set by the user. In other words, a factor is placed in the code which changes how finely or coarsely the two planes are discretized, which can be adjusted based on memory and/or time constraints.

The forward model's primary function is the calculation of the matrix **A** for use with the ML-EM algorithm, as described in section 2.4. Within the script the user defines the activity of a point source. All of the pixels in the source plane and the detector plane are labeled. The program then systematically moves through the source plane, placing the source at each spot in the source plane. At each source position, the
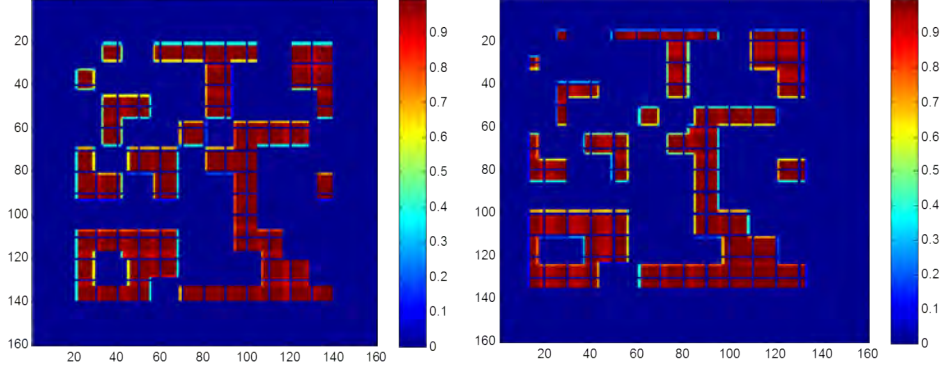
Figure 9. Two images of the detector plane from the model, given two different point source positions. Notice how the features are thinner in the right image. This is due to collimator depth, or vignetting, effects, and is accounted for in the model.

program loops through the detector pixels. For each source and detector pixel combination, the program computes the vector between the centers of the two. By simple geometry, the points of intersection of this vector and the front and rear collimator planes are found. From these coordinates in the collimator planes, the chambers traversed by the vector are found. If the vector passes through open chambers of the collimator only, then the number of counts recorded into **A** is given as:

$$A_{ij} = \frac{I}{d^2} \ N \ P_\alpha \tag{13}$$

$$P_\alpha = \exp(-\frac{\mu}{\rho}\rho t) \tag{14}$$

where I is the number of photons emitted by the point source, d is the distance between detector pixel i and source location j. When the program checks each vector, it records the number of grid walls that the vector passes through, labeled here as N. If a photon were to pass through multiple open collimator elements, it would experience some attenuation in the steel grid that separates the collimator elements. The fractional attenuation due to one of these interior grid walls is given as P_α, where $\frac{\mu}{\rho}$ is the mass attenuation coefficient (taken to be that of steel, given by the NIST

website), ρ is the density of the steel and t is the thickness of the steel [37, 34]. For simplicity, t was set to a constant, approximate value.

If the program finds that the vector between a given source location and detector pixel passes through a closed collimator element, it sets the corresponding element of **A** to zero. All photons that enter the closed chambers are assumed to be attenuated (See Section 4.1 for justification of this assumption). It was found experimentally that a significant number of photons are Compton scattered inside of the collimator. These events are ignored by the model because an energy discriminating detector was used. The detector can be set to record only those detected photons that were received with the known energy of the monoenergetic radionuclide source (plus or minus 2-3 keV). Since the detector filters out the Compton scattered photons, the model need not include them. Additionally, every tenth row and column of the detector matrix is set to zero, as well as the corner pixels, to mimic the real detector (see Section 4.2).
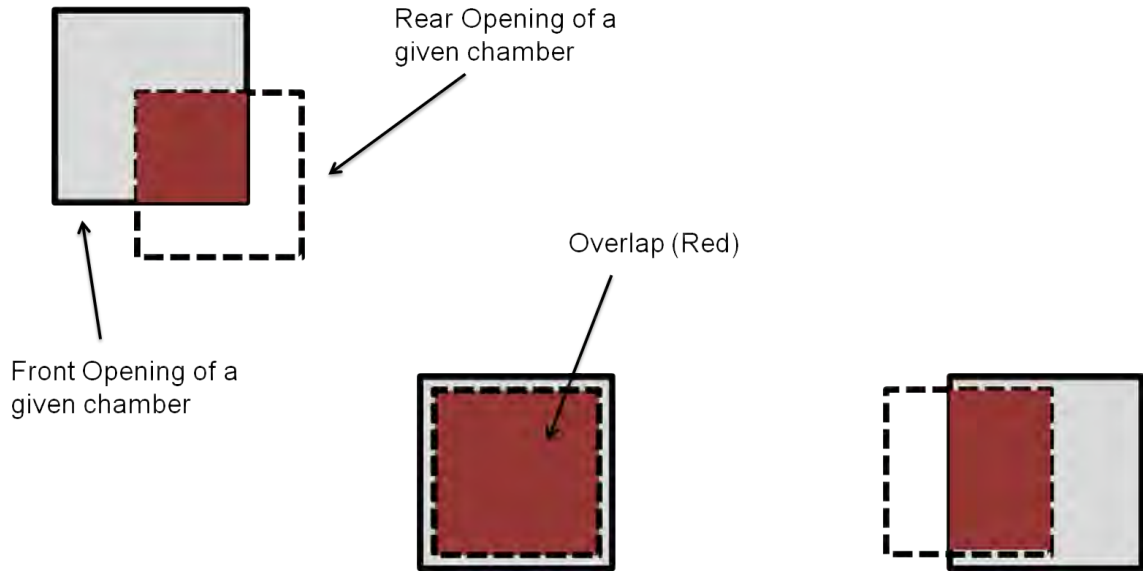
Figure 10. An illustration of the vignetting effect. Viewed from the source, through the collimator. A chamber directly in line with the source and a given detector pixel allows full throughput. Off-axis chambers block part of the possible paths, as a result of collimator depth.

One bit of functionality added later to the model was the ability to characterize, more accurately, the vignetting that occurs from sources in the near-field region due to the collimator's physical depth. Some work has been done to account for the effect of collimator depth on correlation methods, particularly by Mu and Liu in 2006 [50]. Using a different method, this model accounts for vignetting by first over-resolving the detector plane. The script allows for the user to define how fine the resolution should be. Each detector plane pixel is thus split into smaller squares. The probability of a photon reaching each smaller square is found in the same manner as before. All of the probabilities of the little squares are then averaged to find the overall probability for a given detector plane pixel.

Table 1. **Run-times and memory requirements for the calculation of the A matrix. Run-times are based on an above-average desktop computer (for 2011).**

M	N	Time	RAM Req. (MB)
100	25,600	10m	10
2,500	25,600	4h7m	250
3,600	25,600	6h	369
10,000	25,600	16h	1,024

The computation of the $\mathbf{A}$ matrix is nontrivial. As M increases, the RAM and time required to compute $\mathbf{A}$ also increases, as seen in Table 1. There is a limit to how finely the source and detector planes can be discretized based on the computer setup.

In a future version of the model, differences in strip efficiencies should be taken into account, as well as the change in efficiency across a strip. As with the MCST forward model, inclusion of detector depth information would increase model accuracy.

3.2 MCNP Forward Model

A forward model was also created using a Monte Carlo program called Monte Carlo N-Particle Transport Code (MCNP). MCNP was originally developed by Los Alamos National Laboratory to model neutron transport in nuclear reactors, but it can be useful for modeling γ-rays and their interactions with matter as well [69]. MCNP was chosen over other Monte Carlo programs simply because of the author's familiarity with the code and its immediate availability. A primer by Shultis and Faw of KSU was frequently referenced during the writing of this model [63].

The term *Monte Carlo* was first coined and used extensively by John von Neumann, Stanislaw Ulam, and Nicholas Metropolis for the Manhattan Project [24]. In Monte Carlo methods, the geometry of the system is carefully specified so that the material of all of the objects, or cells, in the system is specified. Starting at the source position, dice are rolled, figuratively, and a photon is emitted in a random direction. A large number of distributions are stored in the software for many different types of materials. The distributions are based on cross sections for interactions. For instance, the software has a stored distribution describing how often a Compton scatter event will occur in air for a photon of a given energy. The code will randomly pick different outcomes for each photon, weighted by the appropriate distributions. An outer sphere is usually defined, the interior of which is called the universe. Photons that exit the sphere are "killed." The code probabilistically determines the path of a single photon until that photon is either killed or deposits all of its energy in one of the cells within the universe. Once either of those criteria are met, the program records the path of the photon and starts a new photon. Millions of photons can be tracked in this fashion.

A MATLAB® script was developed to write the input file for MCNP. The input files were thousands of lines long and therefore could not reasonably be written
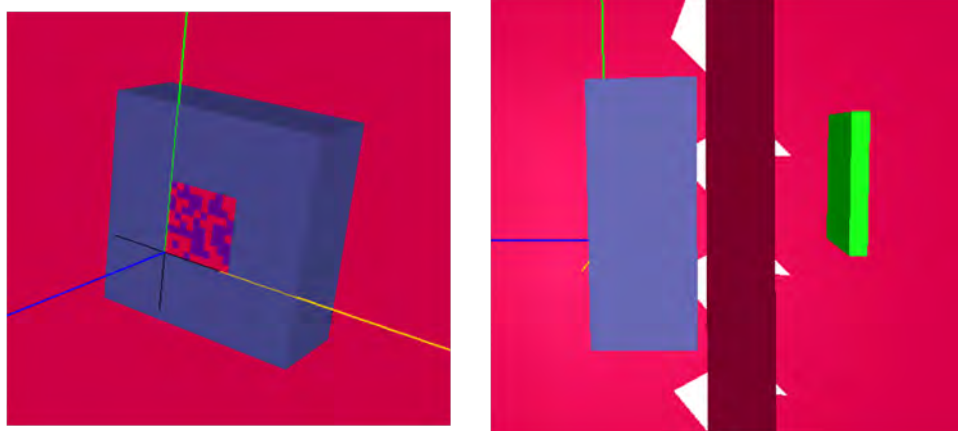
Figure 11. Left: The programmable collimator, as modeled in MCNP. Right: A side view of the programmable collimator and the detector crystal, as modeled in MCNP.

manually. To use the MATLAB® script, the user simply inputs the location of the source and the mask relative to the detector crystal in three dimensions, as well as the mask configuration. Based on the mask configuration, the script fills in the cells corresponding to the collimator chambers either with air and a PEEK plug at the rear, or with a PEEK plug at the front and AIM-70 in the rest of the chamber, depending on whether the chamber is "on" or "off." The script also defines 160 x 160 detector cells, corresponding to the detector subpixels. A 122 keV γ-ray point source was used. Initially the detector crystal was made from germanium. The idea was to record tallys. Each time a photon deposits its full energy in a detector cell, a tally corresponding to that cell increments up by one. However, MCNP only will track 1000 tallys, significantly less than the 25,600 cells of the detector crystal. After this realization, it was decided that the *ptrac* files would be used. The *ptrac* files list the track of all of the particles of interest. The detector crystal material was set to vacuum, and any photon that passed through the detector in the appropriate energy range is recorded in the *ptrac* file. Just like with the real detector, MCNP has an energy window, which was set to 122 keV +/- 5 keV. At that time the plan was that

the actual detector would use a 10 keV energy window, though this was later reduced to 6 keV to further filter out Compton scattered photons.

To further increase computational efficiency, the photons emitted from the source were constrained to a cone which subtended an area slightly bigger than the programmable collimator. In other words, the source was only allowed to emit photons in the solid angle of the cone. By not allowing photons to be emitted in the opposite direction of the programmable collimator, for instance, computation time was reduced dramatically.
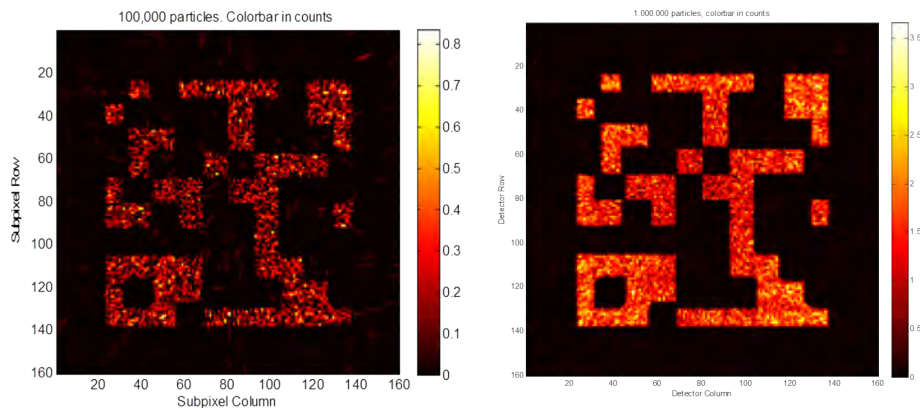
Figure 12. Predictions of the detector response from a point source, given by MCNP, using 100,000 particles (Left) and 1,000,000 particles (Right).

A *ptrac* parser was written to interpret the *ptrac* data. For a given particle track, the parser records which detector cells that the path traversed. Also, for a given path, the parser records the number of detector cells traversed, called EC (for event count). The parser script then adds $\frac{1}{EC}$ to each of the affected detector cells, assuming full energy deposition to be equally possible for each of the traversed cells. This is done for all particle tracks.

At one time, there was hope that MCNP could be used to provide the $\mathbf{A}$ matrix for ML-EM. However, without a sufficient number of particles in MCNP, there is too

Table 2. Run-times and ptrac file-sizes for MCNP simulations based on the number of particles emitted from the source. Run-times are based on an above-average desktop computer (for 2011).

Particles	File-Size (MB)	Run-Time	Avg. Counts per Det. Subpixel
10,000	0.8	13.6s	0.00377
50,000	2.7	43s	0.018
100,000	5	1m18s	0.0329
500,000	24	5m16s	0.1736
1,000,000	47	9m57s	0.349
5,000,000	235	47m16s	1.74
10,000,000	471	1h33m	-
100,000,000	4,698	15h22m	-

much variation from pixel to pixel in **A**. The data must be smooth if they are to work for ML-EM. To achieve the proper smoothness, at least 10,000,000 particles must be used, although 100,000,000 would be better. An average **A** matrix has about 1,000 source positions with up to 10,000 in some cases. Conservatively, using the data from Table 2, it would take 65 days to compute **A**. This simply is not reasonable, especially given the fact that a different **A** is needed for every source-collimator-detector geometry and mask configuration. Nevertheless, the MCNP simulation provided good insight into the number of expected Compton scatter events, the expected attenuation through the "off" chambers, and things along similar lines. Perhaps by using variance reduction, or other more sophisticated techniques, MCNP could be used to calculate the forward model for ML-EM.

3.3 The Optimal Mask Sequence

A code was developed to find the optimal mask sequence for the coded-aperture application of the programmable collimator. The code iteratively determines a sequence of matrices that are most independent from each other. The cross-correlation
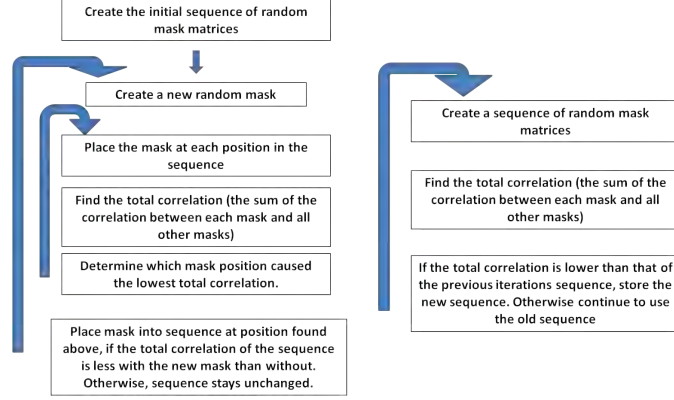
Figure 13. Methods to find the sequence of masks that are least correlated with each other.

is used as a measure of independence between mask matrices. More specifically, the magnitude of the central spike of the cross-correlation is used as the metric. If the central spike is zero, then the two mask matrices are completely independent. The two iterative methods are shown in Figure 13.

It was found that the right-hand method shown in Figure 13 converged more quickly than did the left-hand method. Also, by observing the operation of these codes, it was discovered that the least correlated sequence of matrices is that in which each mask element is open or closed for equal durations. For instance, in a sequence of six mask configurations, each element should be open in three of the masks and closed in three of the masks. After this discovery was made, a code was written to construct a sequence of random masks that adhere to this criterion.

An additional algorithm was written which orders the masks in the sequence for which the programmable collimator user will have the least number of element changes to make during an experiment. This algorithm can lower the number of changes by 40-50 for a six-mask sequence of 10x10 matrices. Later, code may be developed in which the number of changes is determined by the user, and the code will find the sequence of least-correlated masks with the specified number of changes. Additionally, this code could be modified to choose the best masks on the fly. Incoming information

would be incorporated to help choose the next mask to use. These optimal mask sequences would vary based on the application.
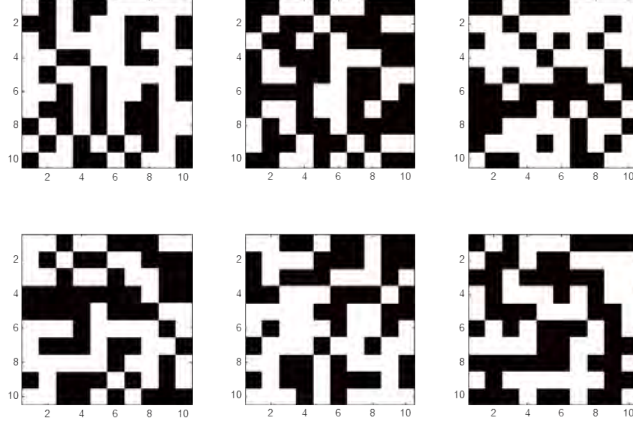
Figure 14. An example, optimized sequence of random mask matrices. Notice that each mask element in this six-mask sequence is open in three masks and closed in three masks.

3.4 MCST Forward Model

A three dimensional Cartesian coordinate system was devised. The millimeter was chosen as the unit in this space. The detector crystal is assumed to be a square, and the origin was placed at the furthest, lowest point of the detector to keep all coordinates positive. Only three points in space need to be defined for a given photon event: the point source, a point in the material, and a point in the detector. Vectors following the rays of light are found between the source and the material and between the material and the detector, defined as

$$\texttt{srcmatvect} = \langle x_{mat} - x_{src}, y_{mat} - y_{src}, z_{mat} - z_{src} \rangle \tag{15}$$

$$\texttt{matpixvect} = \langle x_{pix} - x_{mat}, y_{pix} - y_{mat}, z_{pix} - z_{mat} \rangle \tag{16}$$

The Compton scattering angle, θ, is found through the dot product, such that

$$\theta = \pi - \cos^{-1}\left(\frac{\texttt{srcmatvect} \bullet \texttt{matpixvect}}{|\texttt{srcmatvect}|\,|\texttt{matpixvect}|}\right) \qquad (17)$$

Of course, the detector pixel is not a point, but rather is three dimensional. Each pixel is approximated as a square that extends in y and z. The angles from the point material to the top and bottom of the detector pixel, called β_{max} and β_{min}, are found using the same methodology as used above. In the same way, the angles to the left and right sides of the detector pixel, α_{max} and α_{min}, are found. These angle ranges are used to find the solid angle subtended by the detector pixel as part of the Klein-Nishina integration.

A point material was placed in the space based on the coordinates in Figure 15. A detector was constructed virtually as an 80x80 mm^2 square, with 256, 5x5 mm^2 pixels. The scattered energy, E', was calculated using the Compton equation for each detector pixel (Equation 12). Given a Z of 29 for copper, the expected cross section, in barns, for each detector pixel was calculated.
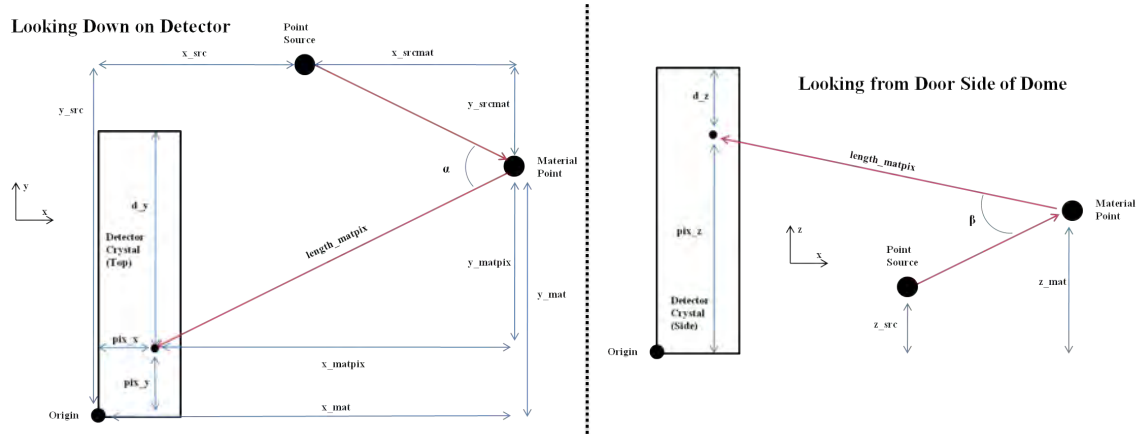
Figure 15. The coordinate system and relevant dimensions used for modeling with the PHDs Co. DSSD.

Eventually, this model can be used in conjunction with an ML-EM or PWLS method. It may be useful to include detector depth information in this model. The PHDs strip detector system is able to make relatively accurate estimates of the depth at which an event occurred [75]. The inclusion of depth information would result in a more accurate model, geometrically. And, of course, the more accurate the model is, the better the iterative methods like ML-EM and PWLS will perform.
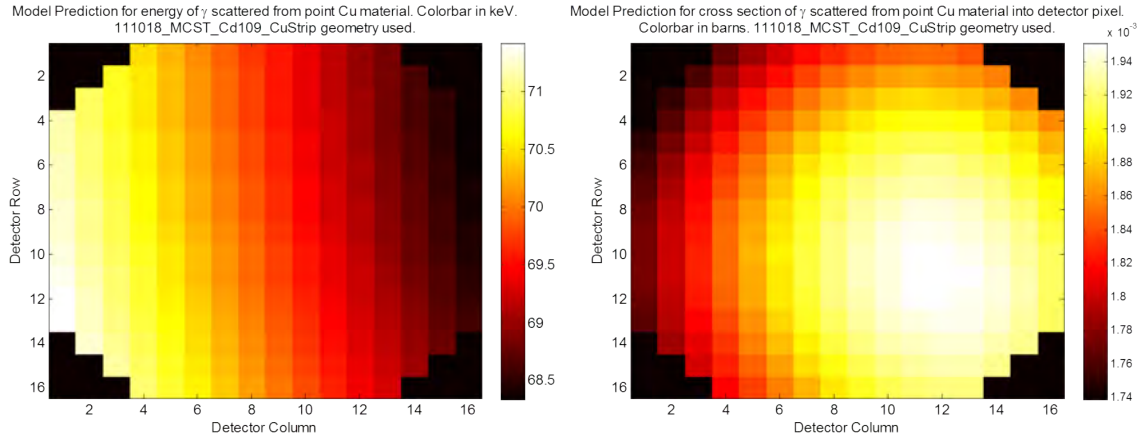
Figure 16. Left: The predicted photon energy into each pixel from the copper "point" phantom. Right: The cross section for scatter, from the copper "point" phantom into each detector pixel.

3.5   MCST Resolution and Setup Analysis

At first, when thought was given to an MCST setup, it was unclear what the optimal setup would be. On the one hand, the Klein-Nishina distribution is angle dependent. The scattering cross-section, in the backscatter region, is greatest at 180 degrees. So to get the greatest number of scatters over a given time, the source and the detector would have to be close to each other with the sample between them in y and out a ways in x. On the other hand, as the sample moves closer to the detector the angles of the source-detector pixel vectors are differentiated more. With
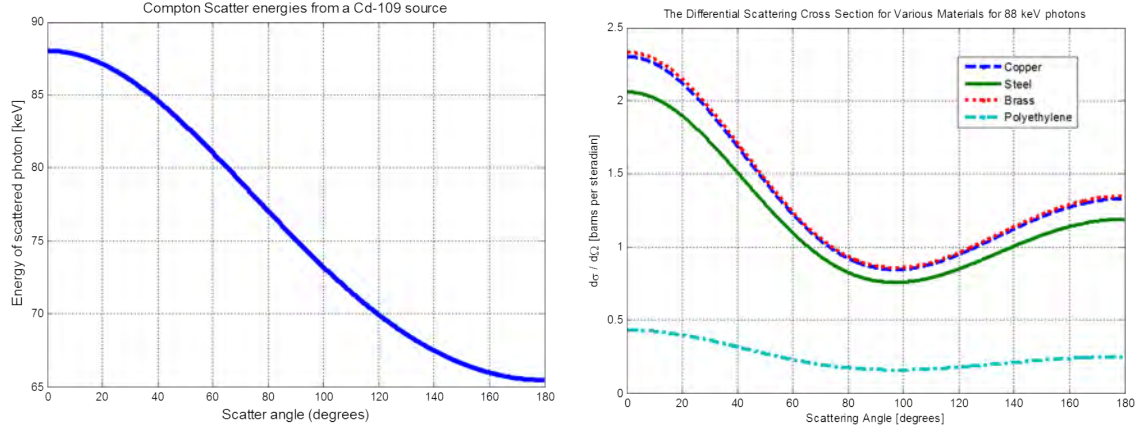
Figure 17. Left: The energy of an 88 keV photon after a Compton scatter, from the Compton formula. Right: The differential cross section for scatter in various materials, from the Klein-Nishina formula [37].

greater differences in the angles into each detector pixel, there are greater differences in the energies found in each detector pixel. A goal of the detector positioning is that the detector subtends the greatest solid angle of scattered photon paths from the material.
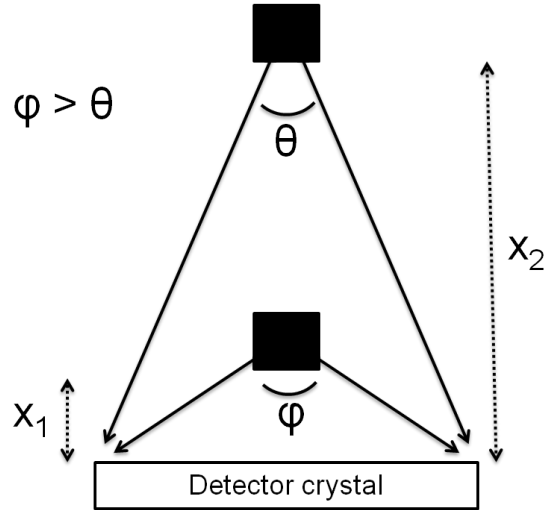
Figure 18. At the closer material-detector distance, x_1, the detector subtends a much larger solid angle, ϕ as compared to the solid angle θ subtended by the detector when the material-detector distance is increased only modestly (x_2).

It was discovered empirically that the angle discrimination advantage gained by moving the material closer to the detector outweighs the decreased cross section for scatter. Indeed, to allow for the closest material-detector distance, the source-material-detector angle becomes about 90 degrees, being the angle with the lowest scattering cross section. In a real application, the sample-detector distance may be fixed to a longer than desirable length. To get the best results this distance was minimized in experiments. The effect of this distance on potential resolution is given in Figure 19.
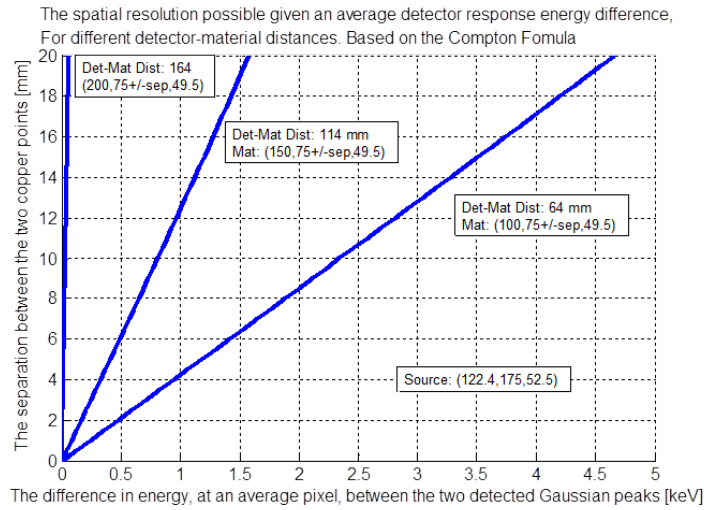
Figure 19. Using the model, two infinitesimally small pieces of copper were separated by various distances (y-axis). The difference in Compton scattered photon energy from each piece was found (x-axis). This graph gives the MCST spatial resolution possible in the sample given the minimum difference in energy between detected photons that is distinguishable. Three sample-detector distances are shown.

To make things more clear, a two-dimensional phantom was conceived, as shown in Figure 20. A model was written to predict the Gaussian response that each piece of material would cause in the detector. These responses must be distinguishable if the MCST method is to be effective. As seen in Figure 20, the distance between the material and the detector significantly affects this distinguishability. To reiterate,

the minimization of the detector-sample distance should be the primary focus when considering the dimensions of the MCST setup. In importance, the minimization of this distance far outweighs the maximization of the cross section for scatter.
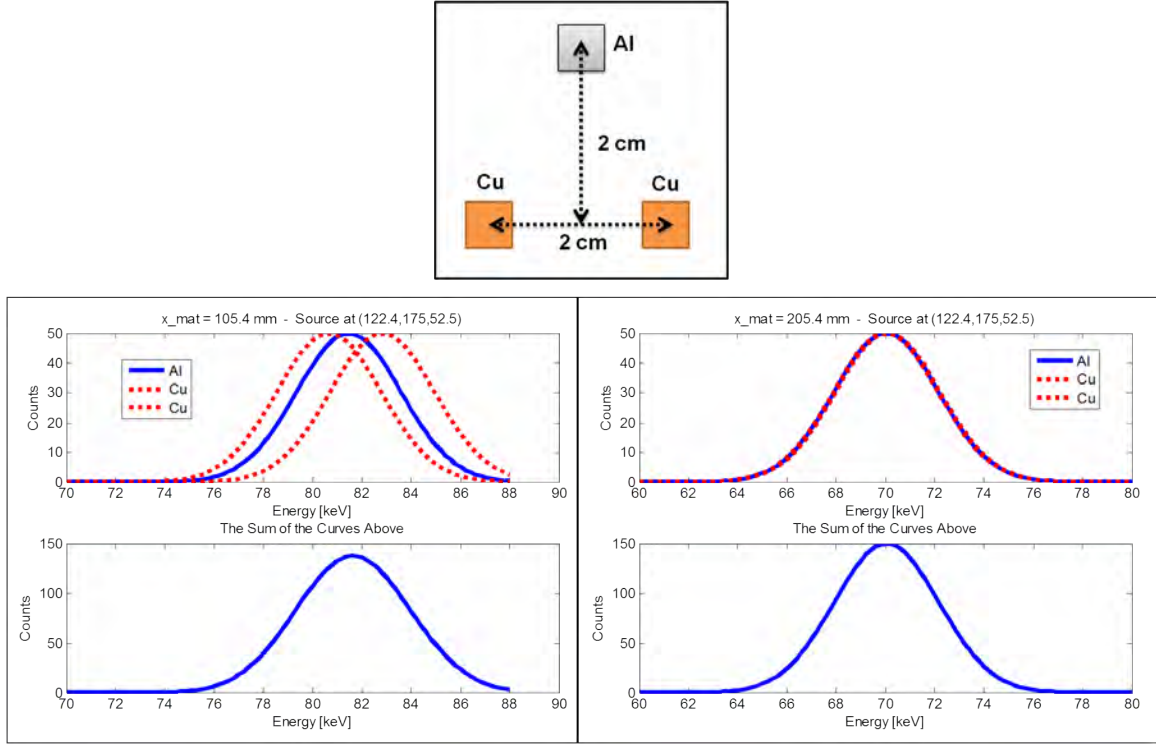
Figure 20. Top: The AlCuCu phantom used for modeling. Left: The predicted detector response, if the phantom were located at 105.4 mm. Right: The predicted detector response if the phantom were located at 205 mm. Notice how indistinguishable the Gaussians from the three materials become when the detector/material distance is doubled.

IV. Design and Experimental Setup

4.1 Progammable Collimator Design

In the first design iteration, it was thought that plastic rods would be submerged in a liquid metal, all within a sealed container. The rods would have small magnets on each end and would be actuated by external permanent magnets or electromagnets. However, the attenuation in the plastic rods was calculated as being too great and significant difficulties were foreseen in actuating the rods. Eventually the current design was chosen.

Figure 21. Molten AIM-70

The programmable collimator, in its present form, was built by the AFIT model shop in the Summer and Fall of 2011. A steel block was fabricated, using Electrical Discharge Machining (EDM), to include 100 elements, or chambers, in a 10x10 array. The square, cross-section of each chamber is 5x5 mm^2, like the PHDs DSSD detector pixels. Each chamber can be turned "on" or "off" to γ-rays. The design was optimized for the 511 keV γ-rays from electron/positron annihilation. Originally the device was intended for AFIT's ongoing positron work. Lower and higher energy photons certainly can be imaged through this collimator.
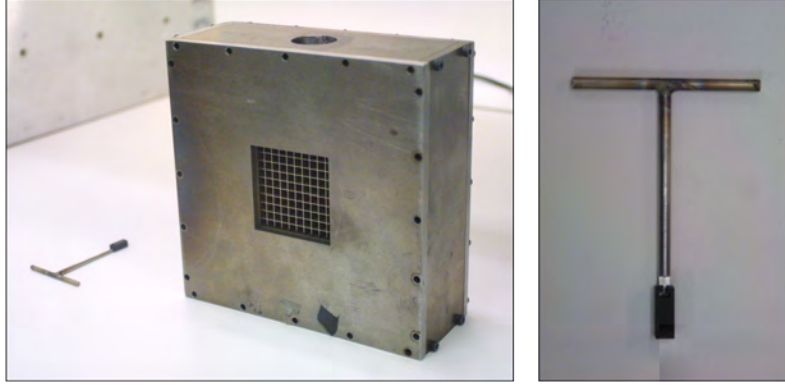
Figure 22. Left: The front face of the programmable collimator. Right: The tool used to move the PEEK rods back and forth in the collimator chambers, locked to a single PEEK plug.

The primary component of the collimator apparatus is the grid block, as shown in the left of Figure 23. The block's outer dimensions are 5x5x5 cm^3. The block is suspended in the center of the outer housing. While in operation the housing is filled with a liquid metal called AIM-70, also known as CerroBEND, Wood's Metal or MCP 158. AIM-70 is a eutectic alloy composed of 50% bismuth, 26.7% lead, 13.3% tin and 10% cadmium, by weight, with a melting point of only 70° C (158° F) [48]. Due to its high $Z_{\texttt{Effective}}$, AIM-70 is a good attenuator of γ-rays. Each chamber also contains a plug made of PolyEther Ether Ketone (PEEK), which prevents the liquid AIM-70 from spilling out of the front of the grid block. PEEK is a highly machinable plastic that is able to withstand high temperatures. The particular flavor of PEEK chosen is filled with carbon to 30%. By filling the PEEK with carbon, the compressive strength increases, the expansion rate decreases and the themal conductivity increases, as compared to unfilled PEEK [55]. Having a low $Z_{\texttt{Effective}}$, PEEK is a poor γ attenuator.

Centered on the rear plate of the apparatus is a square window, also made of PEEK. This window is 5 mm thick. When the apparatus is assembled, the rear face of the chamber block is only 3 mm from the rear PEEK window. This spacing allows

45
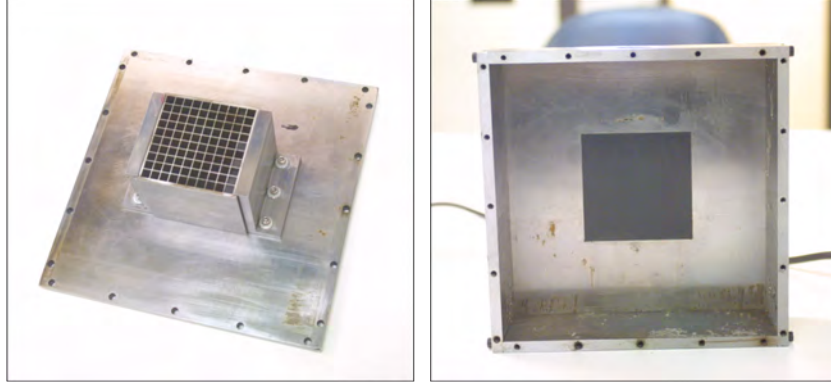
Figure 23. Left: The rear face of the chamber block, suspended in the center of the housing plate, as seen from the interior. Right: The PEEK window in the back of the collimator assembly.

the AIM-70 to flow into the chambers from the outer housing box. A "T" pattern was cut out of each PEEK plug (Figure 22). A matching tool was fabricated with a similar "T" shape on the end. The tool is inserted into the chamber with the proper orientation to allow entry into the cutout of the PEEK plug. Once inside the plug, the tool is turned ninety degrees, locking it in place. The user may then push and pull the PEEK plug within the chamber.

To operate the collimator, each of the 100 chambers is configured in one of two ways. The chamber is turned "on," meaning that γ-rays are allowed through, or "off," meaning that γ-rays are attenuated. To turn the chamber "off," the PEEK plug is pulled all the way to the front of the grid block. The AIM-70, which fills the outer housing, flows around the back of the grid block into the chamber. The AIM-70 in the chamber attenuates any γ-rays that try to pass through. To turn a given chamber "on," the PEEK plug is pushed as far back as possible so that it mates with the rear PEEK window. While the PEEK plug is pushed backward, the AIM-70 is displaced from the chamber and into the outer housing assembly. Once the PEEK plug is mated to the rear PEEK window, a γ-ray passing through that particular
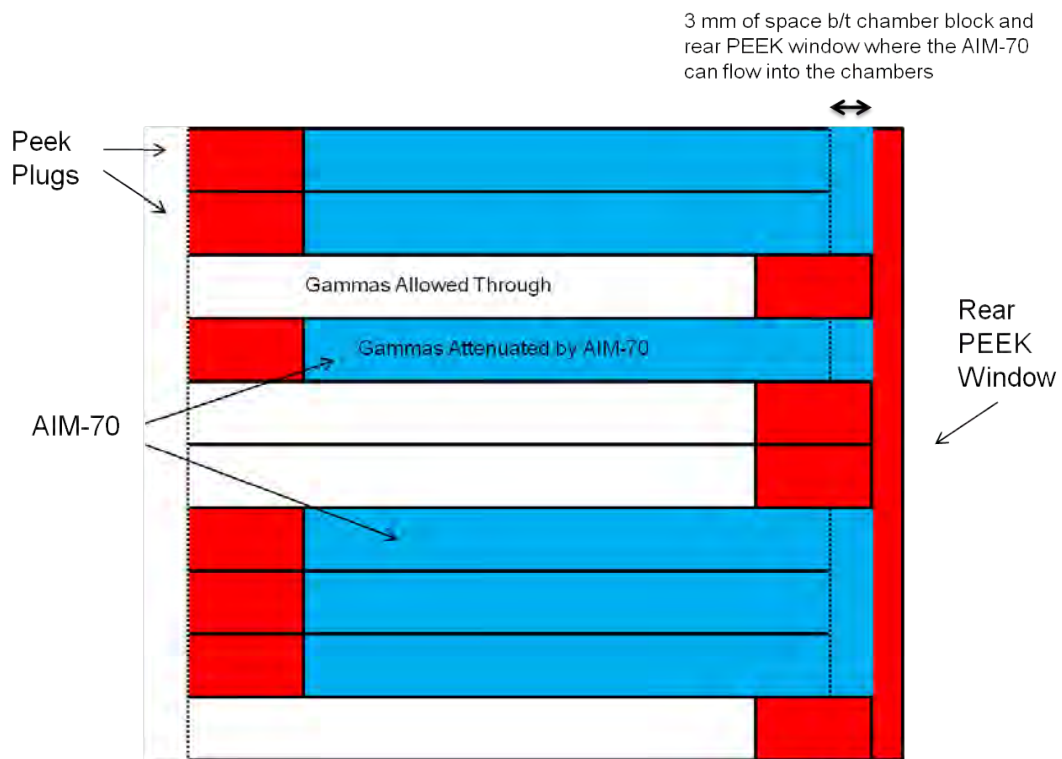
Figure 24. **A slice through the programmable collimator. If the PEEK plug is pulled out (top chamber), the chamber fills with AIM-70, and γ-rays are blocked. If the PEEK plug is pushed in (bottom chamber), the AIM-70 is pushed out of the chamber and γ-rays must only pass through a small bit of PEEK.**

chamber will encounter only air and 17 mm of PEEK, and thus will be only lightly attenuated.

More quantitatively, it is known that

$$\frac{I}{I_0} = e^{-\left(\frac{\mu}{\rho}\right)\rho t} \tag{18}$$

where I is the number of transmitted photons, I_0 is the original number of photons, $\left(\frac{\mu}{\rho}\right)$ is the mass attenuation coefficient and ρt is the mass thickness of the material in question [37]. Hubbell and Seltzer's NIST data were used, ρ_{AIM-70} was taken as 9.38 $\frac{g}{cm^3}$ and ρ_{PEEK} was assumed to be $\rho_{Polyethylene}$, which is 1.19 $\frac{g}{cm^3}$ [34]. As one example, at 511 keV, 83% of the photons will pass through a chamber in the "on" configuration, whereas only 0.57% of the photons will pass through a chamber in the "off" configuration. For 100 keV photons, 72% of the γ-rays would make it through an "on" chamber, whereas 10^{-70}% of the γ-rays would make it through an "off" chamber.

Energy (keV)	Length [cm]	AIM70 (mu/rho) [cm^2/g]	AIM-70 I/I_0	PEEK(mu/rho) [cm^2/g]	PEEK I/I_0
100	1.7	4.73E+00	1.85546E-33	0.1641	0.71750576
100	3.6	4.73E+00	4.85438E-70	0.1641	0.4950956
511	1.7	0.1476	0.095023638	0.0941	0.82665793
511	3.6	0.1476	0.006845548	0.0941	0.66822897
1000	1.7	0.0686	0.334909277	0.0687	0.87024535
1000	3.6	0.0686	0.098619645	0.0687	0.7450449

Figure 25. Selected attenuation data for AIM-70 and PEEK (approximated as polyethylene) for two different lengths at three different energies.

To keep the AIM-70 in liquid form, the entire apparatus must be kept above 70° C. This was accomplished using a hot plate. In the future, heating tape may

be used to maintain operating temperatures. Initially there was concern that the PEEK plugs would fit differently within the steel chambers upon heating, in that the thermal expansion coefficient for each material is different. In other words PEEK and steel expand at different rates when heated. In practice, however, this differential expansion seems to be negligible. The plugs move similarly at all temperatures tested.

An initial test with AIM-70 resulted in some leakage from the housing. The outer housing was disassembled and the edges that make contact with each other were ground and polished, resulting in no further leakage. In another test, the apparatus was filled with water under the assumption that water would leak more than would the thicker, liquid AIM-70. The apparatus was heated to operating temperatures and the PEEK plugs were pushed and pulled within the chambers. During this test, no water leaked from any of the junctures. Furthermore this test again proved that the difference in expansion between the PEEK and steel, with temperature increase, is inconsequential.

As the collimator was tested, concern developed that the experimenter might pull a given PEEK plug all the way out of the grid block when trying to change a given chamber to the "off" configuration. If this were to occur, molten AIM-70 would eject from the device, spilling out into the experimental area. To assuage this risk, the collimator configuration was changed in a fume hood. The collimator was placed within a large, metal tub. The AIM-70 happened to cool and solidify by the time it was taken to the detector setup. The cooling AIM-70 is something that warrants consideration. AIM-70 expands 0.006 inches per inch upon cooling [13]. This expansion causes stress on the chamber walls within the grid block. A few of the chamber walls have shown cracking, possibly due to this effect.

Ultimately, a different alloy is desired. Another eutectic alloy called AIM-47 (or LOW 117) may be considered. It has roughly the same $Z_{\texttt{Effective}}$ as AIM-70 but has

a lower melting temperature (47° C or 117° F) and less expansion upon solidification (+0.0002 inches per inch over the first 6 minutes, followed by shrinkage to -0.0002 inches per inch). This is discussed further in Section 6.4.

The FOV of the collimator was constrained because of the collimator's depth. The height or width of the square plane visible to the collimator, $H_{\texttt{AnyChamb}}$, is given in cm by

$$H_{\texttt{AnyChamb}} = 5 + \frac{2D}{10} \tag{19}$$

where D is the distance from the front of the collimator (or the source side of the collimator) to the source plane, in cm. The equation gives the height of the maximum visible plane, meaning that source positions in which the source is visible through as little as a single chamber are included. If the source is to be seen through all of the chambers, then the visible square is somewhat smaller, where the width or height, $H_{\texttt{AllChamb}}$, in cm, is given by

$$H_{\texttt{AllChamb}} = H_{\texttt{AnyChamb}} - 9 \; ; \; D > 20 \tag{20}$$

Notice that the source must be at least 20 cm from the front of the collimator if it is to be viewable through all of the chambers.

4.2   The PHDs HPGe Strip Detector

A PHDs Co. Double-Sided Strip Detector (DSSD) was used in the experimental portions of this study. The detector consists of a single, 9 cm diameter High-Purity Germanium (HPGe) crystal, with an active depth of 11 mm. The crystal is split into 16 strips on the front and rear faces of the detector, where the front and rear strips are orthogonal to each other. Because the crystal is round, only the middle ten strips on each side extend to a length of 8 cm. Moving outward from the center ten strips,

each strip is progressively 5 mm shorter, so as to conform to the shape of the crystal. The strips are 5 mm wide, effectively resulting in 220, 5x5 mm^2 energy-sensitive pixels (Figure 26). The rear strips, which run vertically, are termed the AC side, whereas the front strips, which run horizontally, are termed the DC side. The AC strips are labeled from 0-15, where 0 is the left-most strip and 15 is the right-most strip. The DC strips are labeled from 16-31, where 16 is the top strip and 31 is the bottom strip [75]. The segmented detector contacts were fabricated using amorphous-germanium detector technology [29, 44, 57, 35]. A Stirling-cycle mechanical cooler maintains the detector operating temperature near 68 K in a vacuum crystat assembly having a mass of about 12 kg [78]. The mechanical cooling and low weight mean that the programmable collimator and detector combination could be made portable for future applications.
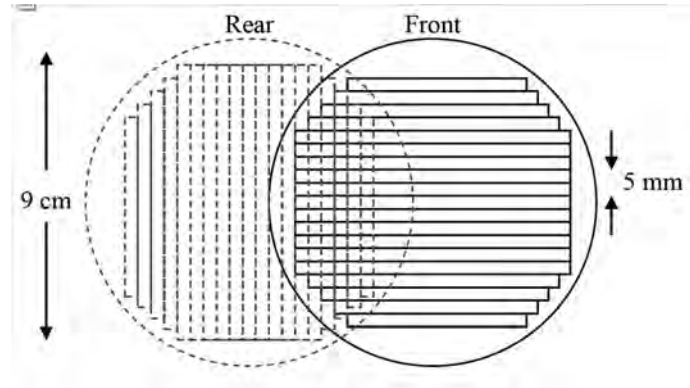
Figure 26. The configuration of the PHDs detector crystal [75].

The strips are connected to an electronics system called the Spect32. The Spect32 contains four Field Programmable Gate Arrays (FPGA), each optimized for imaging. Subpixel resolution can be attained through subpixel interpolation. When the electrons and holes move through a given strip after a photon event, transient charge is induced in the adjacent strips. The amount of transient charge induced in one

adjacent strip relative to the other adjacent strip is related to the location across the event strip in which the photon event occurred. If the photon event occurred closer to one side of the event strip, more transient charge will be induced in the closer adjacent strip [11, 75, 67]. The transient charge in the adjacent strips is measured by the detector system. By interpolation, subpixel resolution down to 0.5 mm is achieved. Thus, the overall resolution of the detector is increased by a factor of ten. Several subpixel interpolation schemes are built in to the detector system software. Every tenth row and column subpixel always reads zero counts, corresponding to the location of the physical separator between strips.

The detector has a FWHM energy resolution of 1 keV at 88 keV. Before use the detector must be calibrated in energy using a known source. Ideally, the same source that is to be imaged should be used for calibration.

4.3   MCST Uncollimated Forward Problem Experimental Setup

A view from the top of the basic setup for MCST is shown in Figure 27. A 101.8 μCi (on 07NOV11), Cd-109 button source was used (T-098). The source was secured to a wooden block, and the block was secured to a precision lab jack. A set of three girders, arranged as three sides of a square, was placed in front of the detector. The square formed by the girders was much taller and wider than the detector, so that Compton scattered photons from the girders would be attenuated geometrically and so that Compton scattered photons from the girders would be of a much different energy than those from sample. Two pieces of nylon fishing line then were hung from the top girder. Weights were tied to the bottom of each fishing line, to keep the lines taut. The samples were then taped to the fishing lines, effectively levitating the samples in front of the detector.

Originally, the samples were taped to a block of polyethylene and were placed on

the same lab jack as the source. This approach suffered from the vibration of the detector cooler. The vibration caused the block to skate around on top of the laboratory jack. The feet of the girder assembly were far enough away from the detector not to be affected by the vibration, and the feet of the girder assembly are padded. Also, by hanging the samples, the Compton scatter events in the polyethylene, which would add noise to the results, are eliminated. The wooden block and the steel shielding block also suffered translation over long periods of time due to the vibration of the cooler. These were secured to the jack with screws. The detector system has built-in mechanisms to dampen the effects of the cooler vibration on the detector crystal. Thus, with the hanging sample configuration, the sample and the detector crystal can be considered stationary relative to each other.
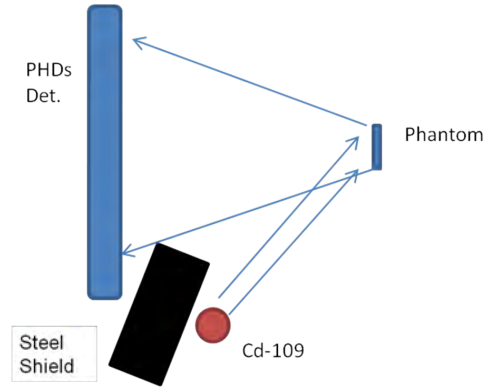
Figure 27. The basic setup used to begin to characterize the MCST forward problem, without collimation.

If Cd-109 is being used for the source, then lead cannot be used for shielding. Cd-109 emits an 88 keV γ-ray. There is a good probability that a γ-ray with 88 keV of energy will knock out a K-shell electron in the lead. When the vacancy then is filled with another electron, an X-ray between 72 keV and 88 keV is emitted [20]. The measured backscattered photons from the sample are between about 65 keV

and 80 keV. Essentially the lead shielding becomes an additional, unwanted source, emitting photons in the energy range of interest. A lower Z material with lower K-shell transition energies was chosen for shielding. Steel was used in this case, based on availability. A 5 cm thick block was used, sufficiently stopping direct photon travel from the source to the detector.
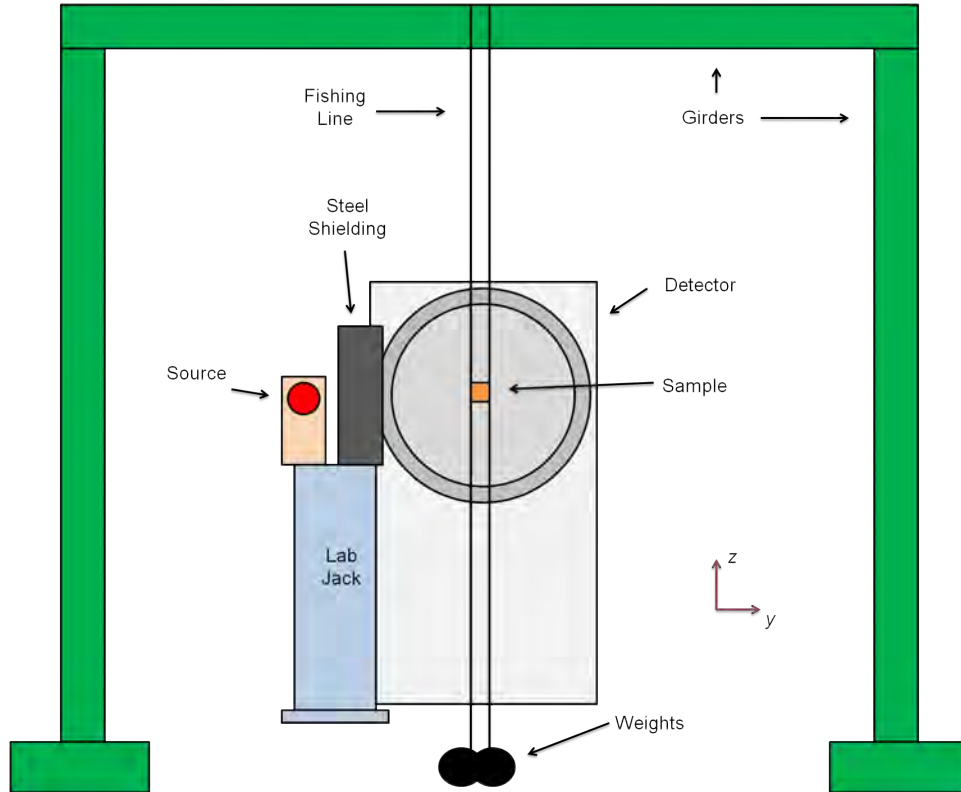
Figure 28. The MCST setup, viewed from the front, looking back at the detector.

Alternatively, a higher energy source could be used, such that the photons scattered in the sample would be easily distinguishable from the lead X-rays. Cd-109 was chosen because it was the most active source available at the time and because it was in the smallest package, making the point source approximation more legitimate. Brian Evans *et al* had originally found the 88 keV photons from Cd-109 to be opti-

mal for Compton backscatter studies in metals for several reasons [25]. First, Cd-109 does not have significant γ-ray emissions of energies higher than 88 keV, which would downscatter into the energy range of interest, introducing noise. Second, the energy must be high enough so that Compton scatter is the dominant mode of interaction in the material. Third, the energy must be low enough such that the mean free path in the material is not too high. The higher the mean free path, the less chance of interaction there will be in the sample.

In millimeters, based on the coordinate system shown in Figure 15, the source was placed at (122.4 +/- 1, 175 +/- 1, 52.5 +/- 2.5). The sample was placed at 205.4 mm +/- 1 mm in the x direction. Typically in the y and z directions, the source was located at 80 and 50 mm, respectively, though these value varied by centimeters from test to test.

Numerous samples were fabricated by the AFIT model shop. Each sample was about 5 mm x 5 mm x 0.7 mm. Samples were made of copper, aluminum, brass and steel. A CuCu "phantom" was constructed, in which two of the copper samples were arranged 5 cm from each other, center to center, and glued to stiff paper. Another phantom was made in which one sample of aluminum and two samples of copper were arranged in an isosceles triangle pattern (Figure 20). The copper strips were spaced 2 cm apart and the aluminum sample was placed 2 cm above the copper strips, centered.

4.4   Coded Aperture Experimental Setup

For the coded-aperture experiments, the coordinate system shown in Figure 15 was used again. The programmable collimator was placed on a laboratory jack as close to the detector in the x direction as was possible. By minimizing the detector-collimator distance, the magnification parameter was also minimized. In the x direction, mea-
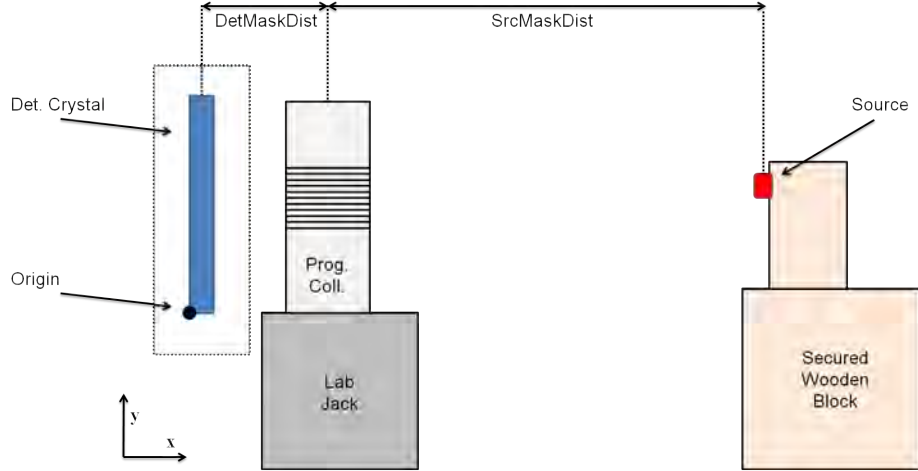
Figure 29. The basic setup for the coded-aperture experiments. Distances used are given in Table 3. Notice that collimator depth is significant with the distances used.

surements were made from the middle of the detector crystal and the middle of the programmable collimator.

Early on it was discovered that the PEEK plugs did not move easily in the chambers, even when liberal amounts of way oil were used as lubrication. The plugs could be pushed in to the "on" position easily enough, but problems occurred when pulling the plugs out to the "off" position. Sometimes excessive force would be needed to pull the plugs out. Each plug had been machined a bit larger than the chambers, and was broached so as to form the tightest possible seal. A few of the plugs fit too tightly. Sometimes in dry tests, when pulling a given plug out, the plug would be pulled out of the chamber entirely. The experimenter would have to apply great strength to overcome the static friction. Once the plug started moving he would not be able to stop himself in time, and the plug would come completely out. If this were to happen during an experiment, molten AIM-70 would gush from the open chamber onto the experimenter and the setup.

The experimental setup was adjusted to temporarily circumvent the above shortcomings of the device until a permanent solution is found. To change the mask

Table 3. Source Positions for the Coded-Aperture Experiment

	Mask-Det Dist [cm]	Src-Det Dist [cm]	Magnification
Position 0	5.6	30.3	1.33
Position 1	5.6	60.6	1.13
Position 2	5.6	177.6	1.04
Position F	8	60.6	1.16

configuration, the programmable collimator was taken to a fume hood. The device was drained of AIM-70 before the configuration was changed. After the configuration change, the collimator was refilled with AIM-70. The collimator was then placed back in to the experimental setup. This method obviously is not ideal and takes much longer than the intended method. However, one advantage of this method is that the collimator can cool before being used in the experiment. There had been concern about a hot programmable collimator being too close to the detector. The detector crystal must be kept at about 50 K. By letting the AIM-70 cool and solidify, one need not worry about heating up the detector. Also, the additional complexities of having a hot plate in the experimental area, along with the need to monitor the molten AIM-70, are eliminated.
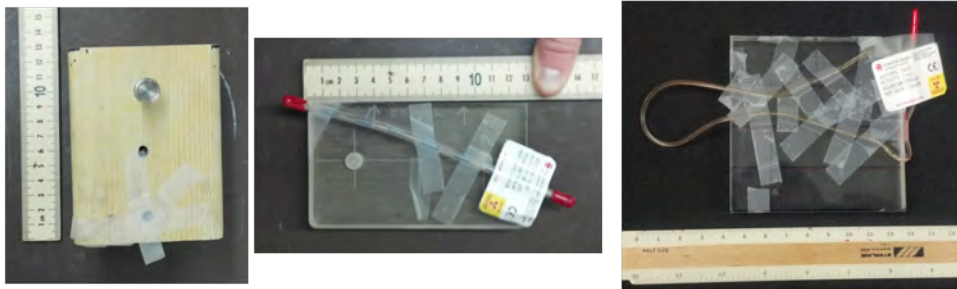
Figure 30. Three selected sources used in the experiments. Left: A 115 μCi, Co-57 button source. Center: An intermittent 38.13 μCi, Co-57 Rod. Right: A 47.66 μCi, Co-57, Flexible Rope

Three source positions were used in order to try different magnifications. Various sources were imaged. The Co-57 sources were used most in the coded-aperture testing. The button source was useful for approximating a point source. The Co-57 rod is about 15 cm long, and is "dotted," or intermittent. There are 1 cm long lead pieces spaced 1 cm apart down the length of the rod. The Co-57 rope was arranged in a distinctive shape. For each mask configuration, the sources were placed at the different positions and data were taken for various amounts of time.

Because the detector is energy-sensitive, an energy window could be set. For instance, with a Co-57 source, the energy window is set such that the only photon events recorded in the image are those with energies of 122.1 keV +/- 3 keV or 136.5 keV +/- 3 keV. By limiting the energy of the photons allowed, photons that have Compton scattered can be excluded. Indeed, only photons that pass straight through a chamber in the "on" configuration are desired. The energy sensitivity of the detector helps to exclude those photons that scatter in closed chambers. The energy sensitivity also serves to limit the background γ-rays that are measured, thus decreasing the noise in the raw data. Even so, the detector was surrounded on the back and sides with walls of lead bricks, to shield the detector from scattered photons originating from other experiments taking place in the laboratory.

Table 4. A selection of the sources used.

Designator	Isotope	Form	Activity [μCi]	Ref. Date	γ Energy [keV]
T-122	Co-57	Button	115	15NOV11	122.06, 136.47
Rod	Co-57	Rod	38.13	04JAN12	122.06, 136.47
Rope	Co-57	Rope	47.66	04JAN12	122.06, 136.47
T-124	Co-60	Planchet	5.85	04JAN12	1173, 1333
T-098	Cd-109	Button	101.8	07NOV11	88.03

V. Results and Discussion

5.1 Coded-Aperture Image Reconstruction Using Decorrelation Methods

A good first place for data analysis is with the correlation methods. Historically these methods were used first and are still used today in some applications. They are much less computationally intensive and much easier to implement. As for the choice of the matched filter, there are a few different options. One is to use the mask pattern as the matched filter G. Another choice is the Brown matched filter, where the zeros are replaced with "-1's."
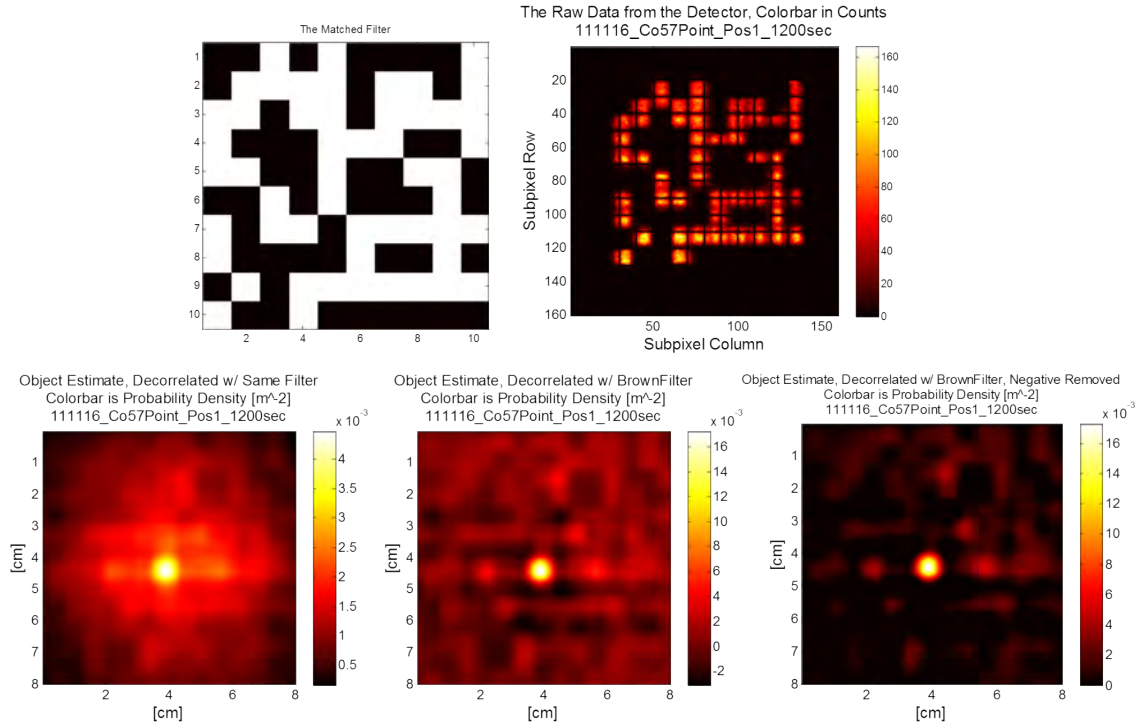
Figure 31. Images from a test using the Co-57 button source at position 1, over 1200 s. Top-Left: The mask pattern. Top-Right: The raw data. Bottom-Left: The object estimate, using the mask pattern as G. Bottom-Center: The object estimate using a Brown matched filter. Bottom-Right: The object estimate using a Brown matched filter, setting negatives to zero.

A MATLAB® script was written to decorrelate the raw data. The mask pattern is input as a matrix, as well as the directory of the raw data text file. The routine imports the data, storing it as a two-dimensional matrix. Next, the routine over-resolves both the raw data matrix and the mask matrix by the same factor so that they maintain equal scaling. The pattern size is increased by a factor of m, where m is the magnification expected. Because the matrices are over-resolved, the mask shadow can be rounded to a much finer range of sizes. By including the effects of magnification, the scale of the decorrelated image, or object estimate, is correct.

After the over-resolved raw data and G matrices are defined, the script invokes the built-in, cross-correlation function, such that

$$\hat{O} = P \star G \tag{21}$$

where P is the raw data and $\hat{O}$ is the object estimate. The numerical cross correlation function outputs a matrix that is bigger than the two matrices that are input, as expected. If P is of size $[M_P, N_P]$ and G is of size $[M_G, N_G]$, then $\hat{O}$ will be of size $[M_P + M_G - 1, N_P + N_G - 1]$. Abstractly, the cross correlation process can be thought of as discretely sliding G over P and recording how well the two "agree" at each location. In this case only the center part of $\hat{O}$ was used. More specifically, the center $[M_P, N_P]$ square of $\hat{O}$ was extracted, and the rest was ignored. The outside portions do have meaning, representing instances where the mask shadow is not fully on the detector crystal. However, it was found that the outside portions were not reliable, and so they were discarded. Furthermore, the sources were placed in a narrow enough solid angle so that the shadow would not project off of the side of the detector crystal.

The script also normalizes $\hat{O}$. That is,

$$\hat{O}' = \frac{\hat{O}}{\left\|\hat{O}\right\|} \tag{22}$$

By normalizing the object estimate, the units of $\hat{O}'$ become cm^{-2}. The values of $\hat{O}'$ are then values of probability density. If $\hat{O}'$ were integrated over its limits the result would be unity. The source is assumed to be located entirely somewhere within the spatial limits of the $\hat{O}'$ matrix and $\hat{O}'$ provides the probability of finding it at a given location within those limits.

Regarding inherent noise and filtering artifacts, perhaps the most instructive of the tests performed were those that used the Co-57 button source. In the bottom-left portion of Figure 31, one can see the results of using A as G. A large amount of inherent noise, or artifacts that arise from the decorrelation process, are seen. This inherent noise is manifested throughout the reconstructed image. Though the button source is still clear in this case, it may not be when short detection times are used or when a weak source is imaged. The Brown matched filter is able to smooth out the inherent noise, to a somewhat constant baseline, as seen in the bottom-center image. Nonuniformities are certainly present, but the source is more easily distinguishable.

A peculiarity that arises when using the Brown type matched filter is that $\hat{O}'$ can take on negative values. Obviously a negative probability is not meaningful physically. One way to account for these negative values is to throw them away entirely. Assuming the negative values of probability to be non-physical, the locations corresponding to those negative values are given zero probability of containing the source. This explanation may not sit well with some. Another way to think about this method is that the baseline is being raised. If the Brown matched filter causes a relatively constant level of inherent noise across $\hat{O}$, this constant noise simply can

be removed. Some signal may be lost but the SNR should increase. Viewing the bottom-right image in Figure 31, the advantage of this correction is clear. In practice one could move the threshold or baseline even higher, discarding even more of the noise.

It is known that coded-apertures are not as effective for extended source imaging. This is why astronomy became the first real use for the coded-aperture. Stars are essentially point sources. Nevertheless, the rod and the rope sources were used to characterize the programmable collimator's ability to image extended sources. One can see a bit of the rod in Figure 32. However, the noise is much more pronounced in this case. In Figure 33 the rope is mostly indistinguishable.

There are a few factors that worsen the object estimate in this particular case. First, the detector crystal is round, as can be seen in the left image of Figure 32. Not only is data lost because of this fact, but data is lost non-uniformly in space. The decorrelation methods do not have a good way to account for this fact, although ML-EM does.

Secondly, the total projection through the collimator can become bigger than the detector crystal if there is any significant magnification. Again, this causes a spatially dependent loss of data that the decorrelation methods are ill-suited to handle. One possible solution is to have either a bigger detector or a smaller collimator so that the projection stays on the crystal, away from the corners. A bigger detector crystal is not foreseeable with current equipment and funds. A smaller collimator could be fabricated given two to five months. Another solution is to move the source farther away from the collimator, decreasing the magnification. This has the disadvantage of lower count rates. Also, given the resulting smaller solid angle subtended by the source, from the detector, the resolution of the object image would be worse if the source were farther away.
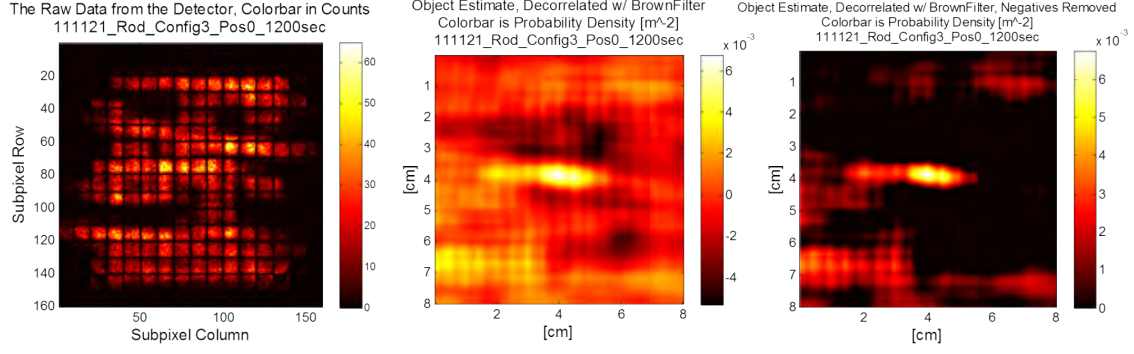
Figure 32. Data from the rod at position zero. Left: The raw data. Center: The object estimate, using a Brown matched filter. Right: The object estimate, Brown matched filter, negative values set to zero.

Thirdly, vignetting was significant with the dimensions used in this study. As mentioned in Section 3.1, there is an analytic formula which can correct the vignetting effects [50]. Such a correctional factor could be applied in the future. Essentially, the raw data pixels would be weighted based on their location, where the center pixels would have a higher weight than the edge pixels.
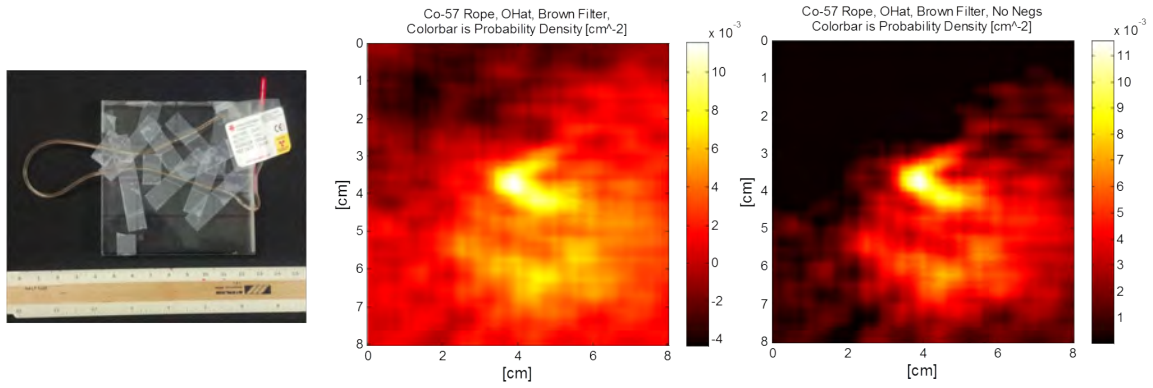
Figure 33. Left: The Co-57 rope source. Center: The object estimate using a Brown matched filter. Right: The object estimate, Brown matched filter, negative values set to zero.

5.2 Coded-Aperture Image Reconstruction Using ML-EM

The same data analyzed with correlation techniques in Section 5.1 were also analyzed using the ML-EM method. The matrix **A** was found as described in Section 3.1. A script was written to import the data from the detector and to run the algorithm. The ML-EM equation for imaging, reproduced here from Section 2.4, is [53, 40, 62]:

$$\lambda_j^{\texttt{new}} = \frac{\lambda_j^{\texttt{old}}}{\sum_i A_{ij}} \sum_i A_{ij} \frac{y_i}{\sum_k A_{ik}\lambda_k + b} \tag{23}$$

The method performed well with point sources. The number of iterations required for a satisfactory object image varies. When imaging a point source, the source became distinct with just a few iterations. Figure 34 shows the object estimate of a Co-57 point source. After just 4 iterations, the source is distinct, though with a halo. After 200 iterations, the source is reduced to a circle with a diameter of about 1 cm. The button source has a physical diameter of 1.5 cm. After 1400 iterations, the pixels of the image become more differentiated. The right image of Figure 34 is an example of ML-EM convergence. After 14,000 iterations, for instance, the image would look similar to that of 1,400 iterations.
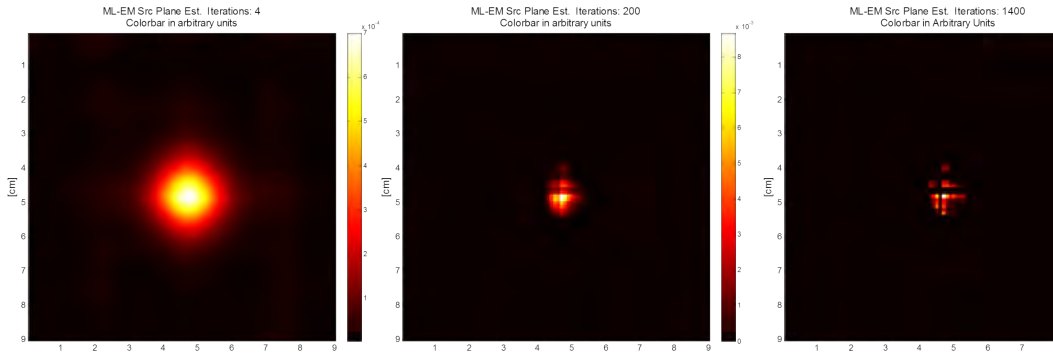
Figure 34. The Co-57 button source was imaged for 30 seconds. Shown is the object estimate after 4 iterations (Left), 200 iterations (Center) and 1400 iterations (Right).

The average amount that each image pixel changed from iteration to iteration is shown in Figure 35. Notice the drastic changes below about 100 iterations. Indeed, convergence can be assumed above a few hundred iterations, where the plots become asymptotic. One should note that full convergence in ML-EM often results in some non-physical artifacts. These non-physical artifacts arise due to limitations in the forward model predications as well as from limited sampling in the raw data. In the right-hand image of Figure 34, for instance, the blotchy pixelation shown is probably not physical. In a commercial system the number of iterations would be limited, in order to prevent these artifacts from developing. By limiting the number of iterations, the reconstructed image may not reach the same spatial resolution, though the number of non-physical artifacts is less. Both fully converged and partially converged images are presented in this document.
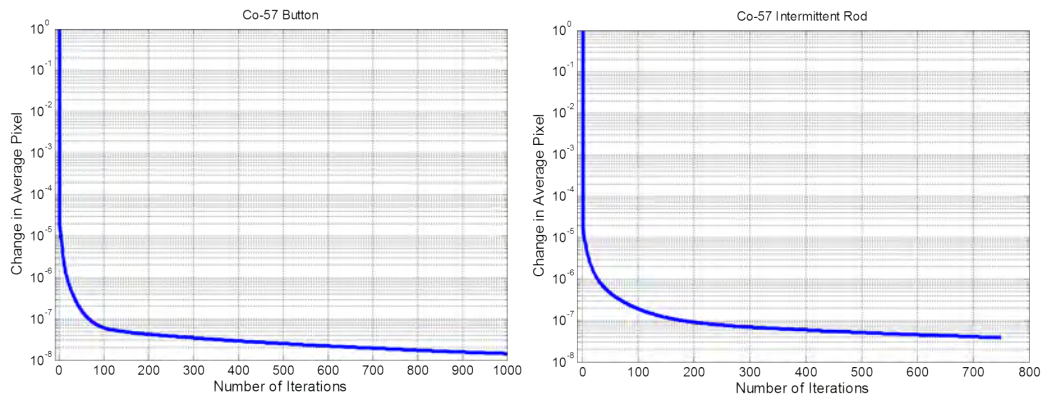
Figure 35. The average change in reconstructed image pixels from one iteration to the next. Left: Data for the Co-57 button source. Right: Data for the Co-57 intermittent rod.

The field-of-view was constrained because of the collimator's depth. It was discovered that the ML-EM method would fail if the discretized source plane did not fit within the field-of-view. Specifically, the reconstructed image would be populated

entirely with NaNs. This outcome is related to the collimator's depth. As described in Section 3.1, the forward model finds a vector between each source pixel and all of the detector pixels. If a photon traveling along a vector from source pixel j to detector pixel i is blocked by the collimator, then A_{ij} is zero. Now suppose, as an example, that source pixel $j = 2$ is completely outside of the collimator's field-of-view. In this case, photons traveling from source pixel 2 to any detector pixel are blocked. Therefore the term $\sum_i A_{i2}$ goes to zero. This term is located in the denominator of Equation 23. In computers, division by zero results in an assignment of the value NaN. Continuing with the example, $\lambda_2^{\mathtt{new}}$ thus would go to NaN. The NaN propagates to other j positions in λ because of the $\sum_k A_{ik}\lambda_k$ term. NaN times a number equals NaN. Within a couple of iterations, λ is filled completely with NaNs. Source configurations must be chosen in which the source is completely within the field-of-view.

The parameter b represents the average number of counts, per pixel, that are not attributable to unscattered rays from the source. That is, b represents the average number of counts that are not of the desired signal. If this parameter is set too high, true data can be lost. Less active regions of the source plane are set to zero artificially. On the other hand, if b is set too low, noise and background counts corrupt the object estimate. The number of iterations and b were set qualitatively, based on how the object estimate looked after the script was finished. Typically the number of iterations needed for convergence ranged between 300 and 800. b was usually set to be 10% of the counts in the raw data pixel with the most counts. A more quantitative means for determining these two values would be useful in a commercialized system.

The data taken using the extended sources were analyzed using ML-EM. The method performed well, especially as compared with the correlation methods. As seen in Figure 36, the full structure of both the rod and the rope is visible. The

images do not hone in exactly to the width of the rod or the rope. The radioactive material in both the rod and the rope has a width of 2 mm. In the reconstructed images shown in Figure 36, the rod has a width ranging from 3-6 mm and the rope has a width ranging from 4-5 mm. This limited resolution does not stem from any problem with the ML-EM method but rather is due to an interplay between the magnification, the cross-sectional area of a given collimator chamber, and the area of a given detector pixel. The magnification of the system could be altered by changing the source-mask and mask-detector distances. If the magnification is increased, the resolution of the reconstructed image increases but then less of the source plane lies within the system's field-of-view, and vice-versa. The magnification and the resolution are directly related. The magnification was chosen in this case so as to fit a significant portion of the extended sources within the field-of-view.
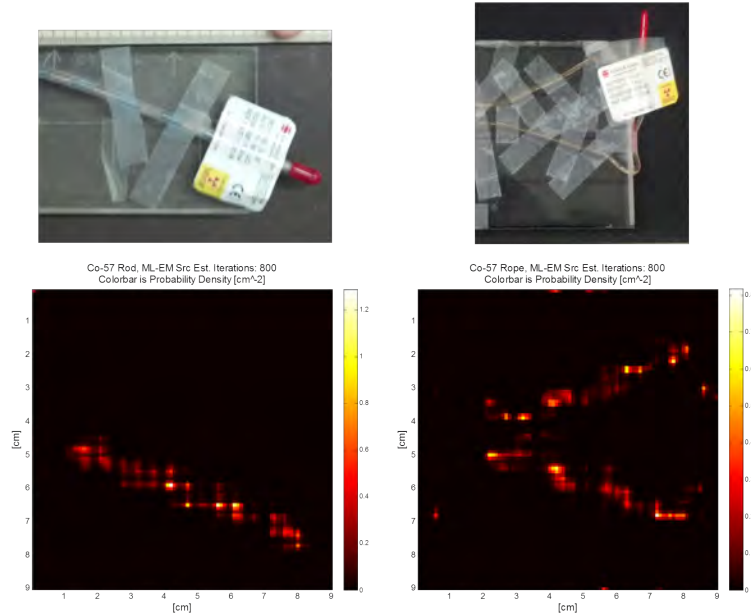
Figure 36. Top-Left: The Co-57 intermittent rod. Bottom-Left: ML-EM reconstruction of the rod after 800 iterations. Data taken for 1 hr. Top-Right: The Co-57 rope. Bottom-Right: ML-EM reconstruction of the rope after 800 iterations. Data taken for 1 hr.

The primary advantage of the ML-EM method over correlation methods is its ability to incorporate certain effects and physical characteristics of the detector that cannot be accounted for using correlation methods. For instance, the **A** matrix takes into account the fact that every tenth subpixel in the detector is dead, and that the detector is round, not square. And, as mentioned before, the forward problem results naturally compensate for vignetting effects. With the continual improvement of computer memory and speed, ML-EM will only become better as compared to the correlation methods. For this problem, algorithm computation times were trivial except when the number of source plane pixels, M, in the matrix **B** were greater than about 20,000, in which case computation times were on the order of ten minutes. A personal computer was used.

5.3   Quantitative Image Analysis and SNR

Comparing two images, the human eye is usually good at determining when an image is better than another. In an image of a radioactive source, the source should be bright (high values) and sharply defined whereas the rest of the image should be black (values of zero) and free of any artifacts. The eye can pick these sorts of things out, but a more quantitative analysis is almost always preferable in science and engineering. Two methods for finding the Signal-to-Noise Ratio (SNR) in reconstructed images were investigated.

Both methods used the definition of SNR from Cunningham *et al* as a starting point [19]. The size and location of the source being imaged is known. The source, being the signal, is removed from the reconstructed image. Only noise remains in the image. The signal and the noise then can be compared.

A script was written to determine the SNR in images of button sources. The user is able to define the center and the radius of a circle which represents the button
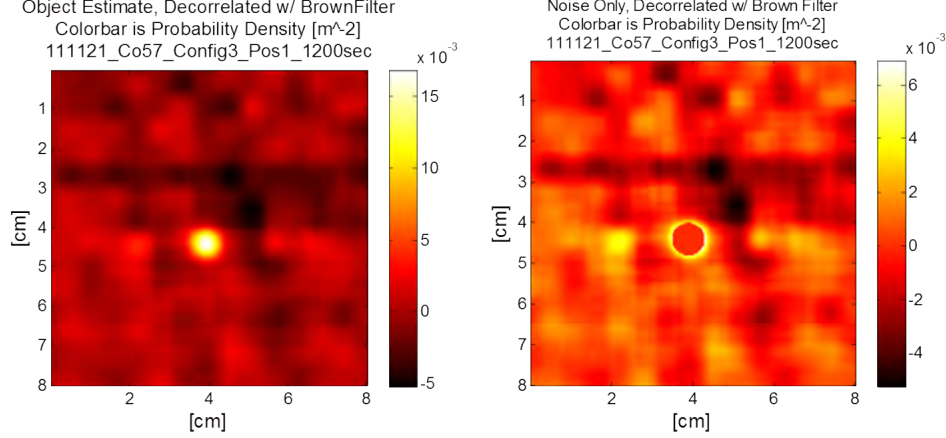
Figure 37. From the object estimate (left), a circle of signal is found, by hand, leaving the rest to be noise (right).

source. The values of the pixels in the image that are covered by the circle are placed in a length M_B vector called B, where M_B is the number of pixels that are covered by the user-defined circle. The values of the pixels not covered by the circle are placed into a vector called C of length M_C, where M_C is the number of pixels that are not covered by the circle. Notice that $M_B + M_C$ equals the number of pixels in the image.

In the first version of SNR used, the mean of the values in the signal list, $\overline{B}$, and the mean of the values in the noise list, $\overline{C}$, are found. The SNR is simply:

$$\mathrm{SNR} = \frac{\overline{B}}{\overline{C}} \tag{24}$$

This formulation works well, except in the correlation method that uses the Brown matched filter. When the Brown matched filter is used, the object estimate contains negative values. The negative noise is just as detrimental to the image quality as is the positive noise. However, if a simple mean is taken of the noise list, then many of the negative noise values would cancel out the positive values. $\overline{C}$ would be close to zero, yielding an artificially high SNR. Another version of the SNR compensates for these negative values by using the Root Mean Square (RMS) of the signal list and of

the noise list. The RMS signal, S, is defined as

$$S = \sqrt{\frac{\sum_{m=1}^{M_B} (B_m)^2}{M_B}} \tag{25}$$

and the RMS noise, ζ is

$$\zeta = \sqrt{\frac{\sum_{m=1}^{M_C} (C_m)^2}{M_C}} \tag{26}$$

The SNR_{RMS} is defined as

$$\text{SNR}_{\text{RMS}} = \frac{S}{\zeta} \tag{27}$$

The signal and noise distributions were examined for general insight and to determine if an appropriate simplification could be made. An example is shown in Figure 38. The noise that is found in images reconstructed with correlation methods generally adheres to the Poisson distribution, even through the decoding process. Radioactive counting experiments in which the counting time is short compared to the half lives of the nuclides used will follow Poisson statistics. In this case, the standard deviation is equal to the square root of the mean of the distribution [37, 64].
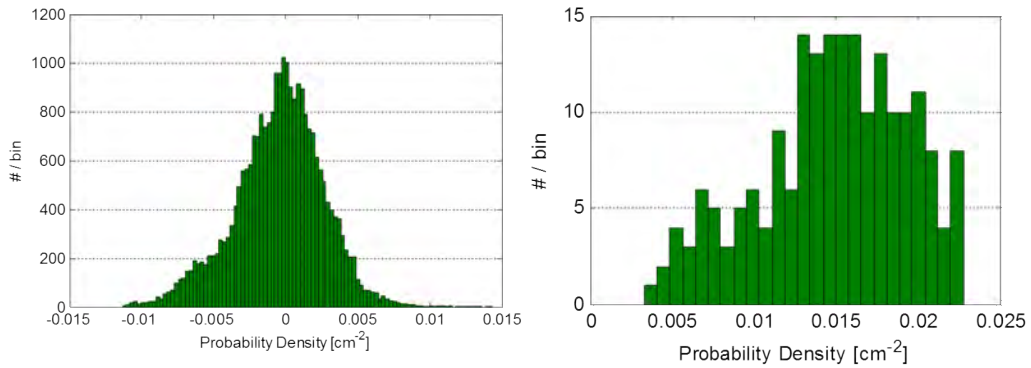
Figure 38. Left: A histogram of C taken from an image of the Cd-109 source with background. Right: A histogram of B from an image of the Cd-109 source with background.

70

The signal list, B, from the correlation method images, as well as both B and C from the ML-EM images, do not adhere to any known distribution. For thoroughness, the standard deviation for B and C was calculated outright for all images. For the first SNR formulation,

$$\sigma_B = \sqrt{\frac{\sum_{m=1}^{M_B} \left(B_m - \overline{B}\right)^2}{M_B}} \tag{28}$$

$$\sigma_C = \sqrt{\frac{\sum_{m=1}^{M_C} \left(C_m - \overline{C}\right)^2}{M_C}} \tag{29}$$

Under the SNR_{RMS} formulation,

$$\sigma_S = \sqrt{\frac{\sum_{m=1}^{M_B} \left(B_m^2 - S^2\right)^2}{M_B}} \tag{30}$$

$$\sigma_\zeta = \sqrt{\frac{\sum_{m=1}^{M_C} \left(C_m^2 - \zeta^2\right)^2}{M_C}} \tag{31}$$

In the calculation of SNR, the variances add [68]. Eventually the images could be conditioned, removing noise without significant loss of the true signal. The goal of this research is not to produce the best possible images but to show the relative improvement between images when multiple mask patterns are used.

5.4   Image Improvement from a Multiple Mask Sequence

As a coded-aperture, the overarching goal of the programmable collimator is better image quality. This is accomplished by using different mask patterns, which provide semi-independent views of the source. The different views provide new data that helps to cancel out noise and irregularities resulting from the previous views' data. The programmable collimator can improve imaging systems in two different fashions. It can either make better images in the same measurement time as compared to a

traditional coded-aperture, or it can arrive at the same quality image that a traditional coded-aperture would produce but in less time. The former situation was explored in this test campaign. The Co-57 button source, the Cd-109 button source (with background injection), the itermittent rod, and the rope were all imaged at Position F (See Tables 4 and 3). The rope was only imaged with up to five masks, rather than ten.
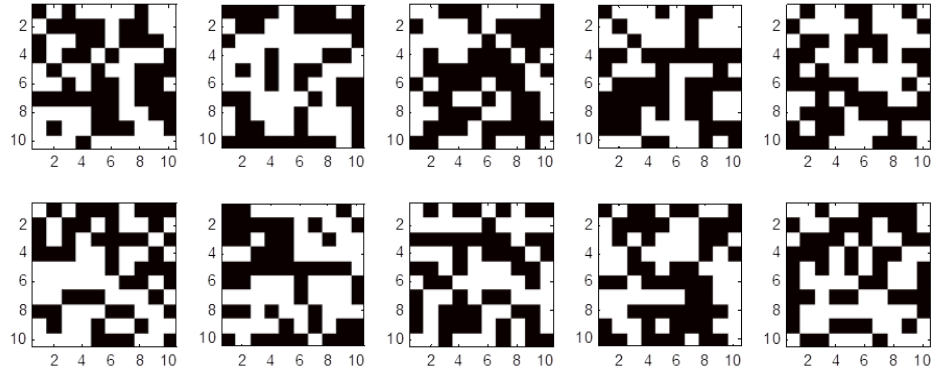
Figure 39. The 10-mask sequence of random masks used for testing. The sequence was found by the program described in Section 3.3.

The Cd-109, rod, and rope sources were all imaged for a total of 1 hour. The Co-57 source was imaged for a total of 5 minutes. As more masks were used, the total time was divided between each mask. For example, when the intermittent rod was viewed through two masks, data were taken with each mask for 30 minutes. When three masks were used, data were taken through each mask for 20 minutes, and so forth. In this way the total measurement time remained the same so that fair comparisons could be made between sequences with different quantities of masks.

To reduce the number of mask changes to be made to the collimator, all of the sources were viewed through each mask before changing the mask pattern. All required data collection times were found for each mask before changing the pattern.

Unfortunately, the proprietary HPGe detector software did not allow automation, meaning that each data-run was initiated manually. If automation had been an option, more more mask patterns would have been used. Nevertheless, good results were found with ten mask patterns.

A standard coded-aperture setup was used for the test campaign (Figure 29). The position of the collimator and the sources were marked on their respective stands using a sharp pen. The collimator was taken to a different laboratory with a fume hood for reconfiguration. When returned, it was positioned according to the marks on the stand. The sources were repositioned similarly between tests. This method led to some net movement or magnification/demagnification of the source in the reconstructed images, as explained in Subsection 5.4.1. Images were reconstructed using the Brown matched filter decorrelation technique and using ML-EM. When multiple masks were used, a reconstruction technique was performed on the data from each mask pattern. The reconstructed images were weighted equally and summed together. The summed image was then normalized to allow for legitimate comparisons between different sequences. Image improvement was demonstrated with all sources, as described in the following subsections.

Table 5. The data-runs performed for the Cd-109 source. Each "1" represents a single data-run.

Mask	3600 s	1800 s	1200 s	900 s	720 s	600 s	514 s	450 s	400 s	360 s
1	1	1	1	1	1	1	1	1	1	1
2		1	1	1	1	1	1	1	1	1
3			1	1	1	1	1	1	1	1
4				1	1	1	1	1	1	1
5					1	1	1	1	1	1
6						1	1	1	1	1
7							1	1	1	1
8								1	1	1
9									1	1
10										1

5.4.1   Image Shift Correction

It was discovered that the collimator had translated between mask patterns. When the mask was reconfigured in a different laboratory, it was not returned to the exact same position in the imaging laboratory. This caused a shift in the reconstructed images.

Table 6. The coordinates of the center/maximum pixel of the reconstructed button source for each of the ten masks, in mm. Co-57 dataset 1.

Mask Num.	1	2	3	4	5	6	7	8	9	10
Row	48	50	50	51	50	49	50	50	52	51
Column	44	48	51	50	46	52	46	51	51	51

For every mask pattern, data were taken using the Co-57 button source. The ML-EM images of the Co-57 source were so clean that the shift could be discerned. In all reconstructed images, the pixel with the highest probability density value also was the pixel at the center of the reconstructed button source. The coordinates of these maximum/center pixels were recorded. The results from one trial are given in Table 6. Notice that the center pixel varies by as much as 8 mm from mask to mask. Most of the image movement is horizontal, meaning that the biggest changes in collimator placement were lateral.

Results from multiple trials were averaged, giving the expected shift from mask to mask. The values for the first mask were used as the true position. Images formed using subsequent mask patterns were shifted based on the difference between that mask's reference coordinates and the first mask's reference coordinates. In this way the effects of collimator movement were reduced. Changes in magnification due to

collimator movement were not accounted for. However, translation of the collimator by a few millimeters would change the magnification only negligibly.

For future experiments, an assembly should be built to ensure that the collimator does not change position. Of course, this system is only a proof of concept. A real system would be automatically reconfigurable using computer control, eliminating the need to ever move the collimator.

5.4.2   Co-57

The most straightforward test was that which was performed on the Co-57 button source. This active and small source served as a good approximation of a point source. Two datasets were recorded. About 47,000 events inside the energy window were recorded over a given, total datarun. The correlation reconstruction techniques work well when a point source is imaged. In the top-left image of Figure 40, the source is clearly visible when just one mask is used, though significant inherent noise dominates the image. When five-mask and ten-mask patterns were used, the inherent noise in the decorrelated image was reduced significantly. The source and its halo stay the same size regardless of the number of masks that were used.

The ML-EM technique produced a mostly noiseless image with a single mask pattern. The detail in the source itself increases when more mask patterns are used. In the fully converged one-mask image, the source has a noticeable, nonphysical, horizontal discontinuity and an artifact slightly above it. Both features are not present in the fully converged five-mask image. The ten-mask image shows a tightened source and a decrease in halo size versus the five-mask image.

The SNR was found for each mask sequence and reconstruction method as explained in Section 5.3. Results for the correlation method are shown in Figure 41.

Figure 40. Images of the Co-57 button source using Brown correlation, ML-EM with 100 iterations, and ML-EM with 500 iterations. 1, 5, and 10 mask sequences are shown.

SNR_{RMS} clearly increases when more mask patterns are used. The SNR_{RMS} was 4.30 +/- 0.0003 times higher when ten masks were used versus when one mask was used.

Figure 41. Plot of the SNR_{RMS} versus the number of masks used. Correlation method. Co-57 button source. 1 hour total measurement time. Error bars are shown.

One interesting feature in Figure 41 is the discontinuous distribution of the data points. The SNR_{RMS} jumps up substantially between 2-3 mask sequences and between 5-6 mask sequences. This effect is explained in Section 5.5.

In the ML-EM images, the SNR and SNR_{RMS} increased by as high as nearly 10,000. It's unclear why the SNR peaks for the 7 and 8 mask sequences. The radius of the signal circle was increased, and the plots looked similar, meaning that the trends are not caused by the chosen position of the signal circle. SNR analyses on the ML-EM reconstructed images for this source are of some utility but should not be dwelt upon. The results were included for completeness. Already with a single mask, the noise in the reconstructed image is very low. Essentially the black areas of the bottom right image in Figure 40 are zero. The actual values in those pixels are something very low (about 5×10^{-43}). When those values decrease, on average, by a factor of ten, the SNR increases by a factor of ten, but the noise in those areas is still

essentially negligible. Nevertheless, the upward trend in the data presented in Figure 42 is undeniable.
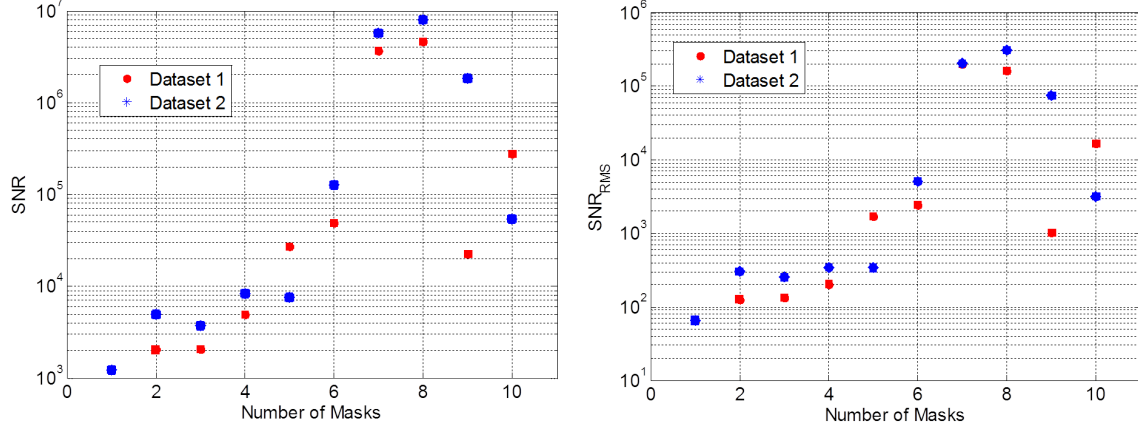
Figure 42. Left: Plot of the SNR versus the number of masks used in the sequence, ML-EM method, Co-57 button source, 1 hr total measurement time. Right: Plot of SNR$_{\mathbf{RMS}}$ versus number of masks used. Error bars are shown in both.

5.4.3 Cd-109 Button Source with Background Injection

As was mentioned in Subsection 5.4.2, the ML-EM reconstructed image of the Co-57 button source was already good with a single mask pattern. In order to better gauge the image improvement, a higher background and more external sources of noise were desired. In order to accomplish this, the Cd-109 source was placed 2 cm above the Co-57 button source (Table 4). The Cd-109 source has an activity of about 10% of the Co-57 button source, for the γ-rays of interest.

The unscattered γ-rays from the Cd-109 source are observed directly. Some γ-rays from the Co-57 source scatter down in energy to the energy window and are detected, also. These extra photons corrupt the image of the Cd-109 source. Figure 43 shows how the choice of energy window affects the reconstructed image. With a large energy window, more of the scattered photons from the Co-57 source are observed, and vice
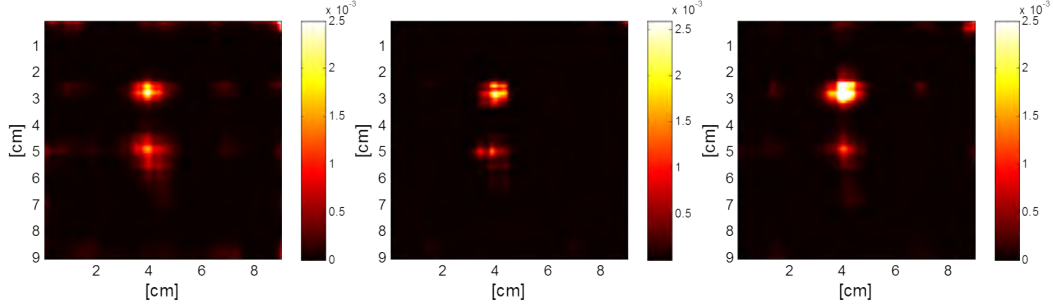
Figure 43. The effect of different energy windows. The colorscale is fixed. Left: 84-92 keV window. Center: 86-90 keV window. Right: 87-89 keV window.

versa. With a smaller energy window, more of the background is blocked out, but the count rate decreases. Based on the application, a choice must be made between a more stringent energy filter or higher count rates. For these tests an energy window of 86 keV - 90 keV was used. About 70,000 events were recorded for each total datarun.

Note that the Co-57 source, seen below the Cd-109 source in the images (Figure 44), is somewhat visible. Even though the scattered photons are observed, a blurred version of the Co-57 source is still seen. Based on the lead shielding around the detector, and the AIM-70 within the housing of the collimator, these photons presumably came through the open chambers of the collimator. Compton scattering of a photon from 122 keV to 88 keV results in a directional change of about 130 degrees, ruling out single-scattered photons. Instead, the observed photons from the Co-57 source likely are those that scatter multiple times inside of the collimator. By bouncing back and forth between the AIM-70 of the closed chambers, these photons maintain a similar trajectory to that at which they were emitted, but with lower energies. In this way the ML-EM algorithm is able to recreate an image of the Co-57 source, even though the energy window is set much lower than 122 keV.

In the future, this effect could be characterized, leading to a more effective system. Ideally, the full energy spectrum of detected photons would be used to reconstruct an image of the source. Again, with a larger energy window, count rates increase.
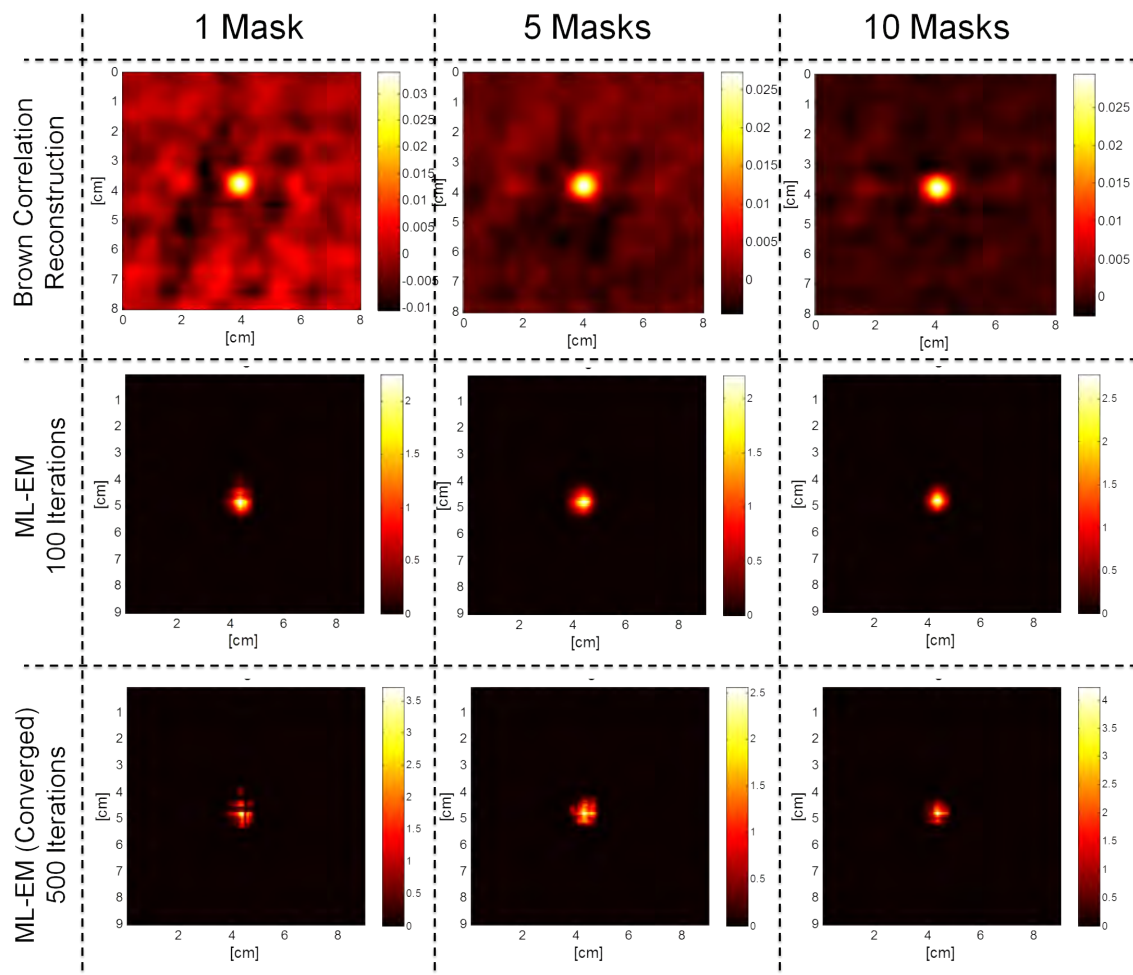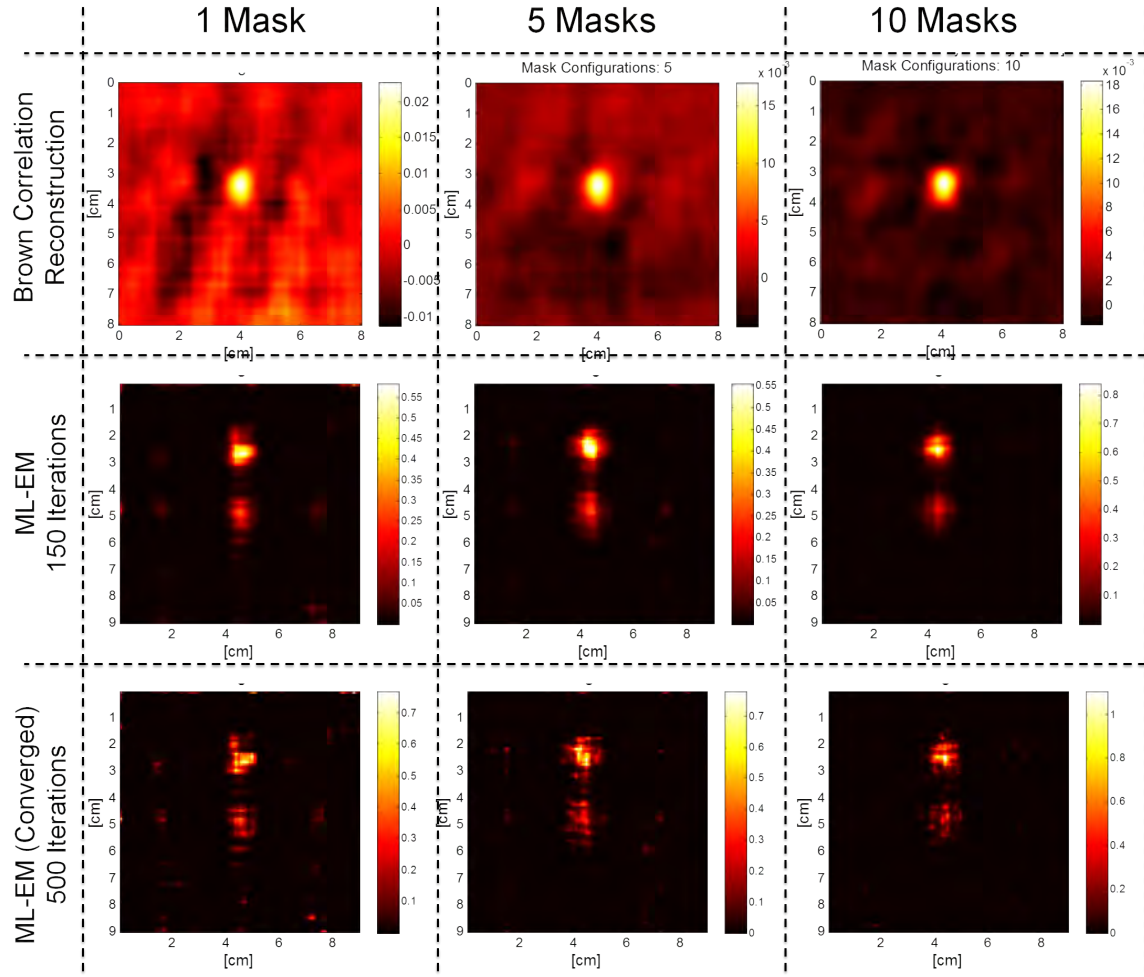
Figure 44. Images of the Cd-109 button source with background using Brown correlation, ML-EM with 150 iterations, and ML-EM with 500 iterations. 1, 5, and 10 mask sequences are shown.

Returning to the main purpose of the test, the use of multiple mask patterns successfully reduced noise in the reconstructed images. The inherent noise in the correlation images is greatly reduced with the use of multiple masks. With the ML-EM method, the Cd-109 source is apparent above the blur from the Co-57 source. When 1 mask was used, significant noise is visible in regions of the image where no source was present. This noise is reduced when more masks are used. The Co-57 blur remains, regardless of the number of masks used. With more masks the size of the Cd-109 portion of the image is honed down.

Using the SNR analysis methods presented in Section 5.3, the SNR and SNR_{RMS} were found. The results for the correlation method are shown in Figure 45. The SNR_{RMS} increased by a a factor of 3.04 when ten masks were used. Notice that the discontinuities between 2 and 3 mask sequences and 5 and 6 masks sequences are present again, as they were in the SNR plots for the Co-57 images. A potential explanation for these discontinuities is given in Section 5.5.
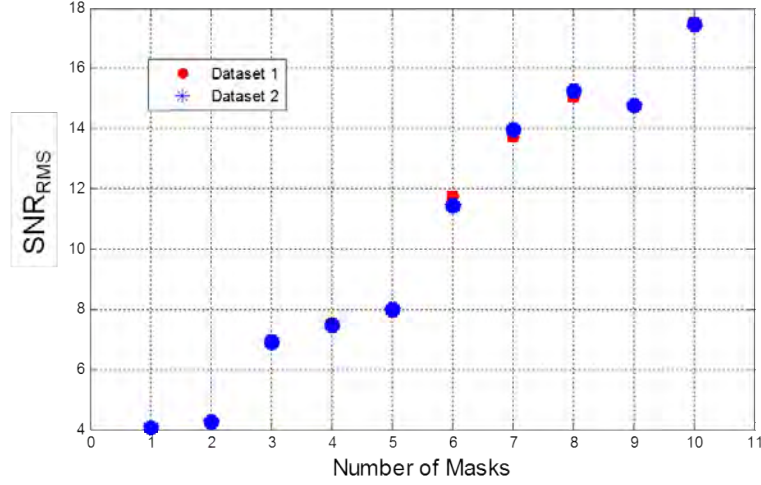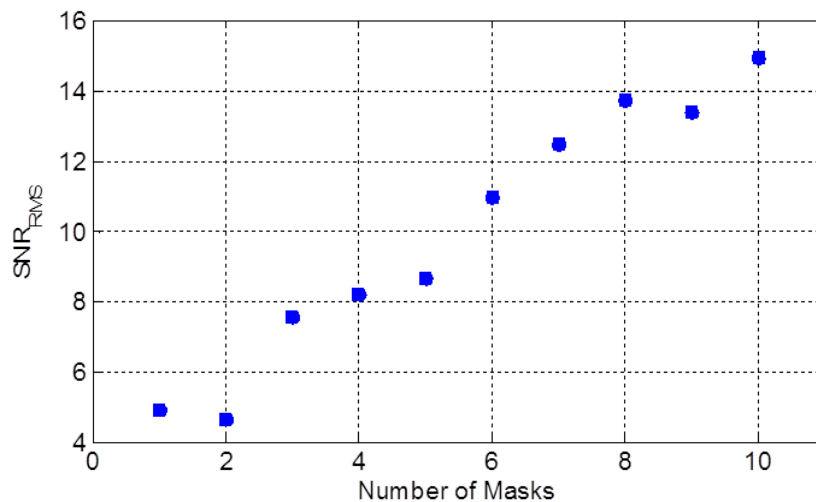

Figure 45. Plot of the SNR versus the number of masks used. Correlation method. Cd-109 button source with background. 1 hour total measurement time. Error bars are shown.

The ML-EM SNR plots both show significant increases in SNR. SNR increased by a factor of 1.8 when ten masks were used. The discontinuity between the 5 and 6 mask SNR results is possibly due to the explanation given in Section 5.5. However, the reason for the SNR jump between 1 and 2 masks is unclear.
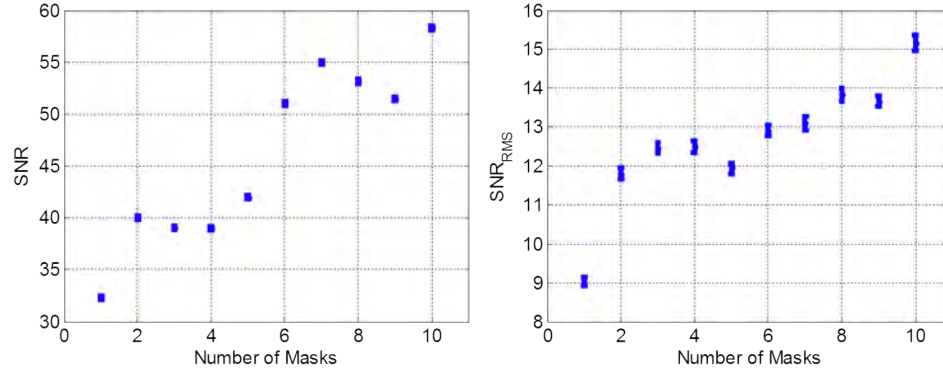
Figure 46. Left: SNR versus number of masks used, Cd-109 with background, 1 hr detection time. Right: SNR_{RMS} versus number of masks used, Cd-109 with background, 1 hr detection time.

This source configuration is somewhat strange, in that much of what was considered noise originated from the Co-57 source located within the field-of-view of the collimator/detector. It was not expected that the Co-57 would still be visible in the reconstructed images. The increase in image quality is clear to the eye, with the Cd-109 source becoming sharper when more masks were used. For a future test, the source of background radiation should be placed behind the detector to provide a source of uniform radiation.

5.4.4   Co-57 Intermittent Rod

With the intermittent rod, about 100,000 events were recorded by the detector in a given, total datarun. Two lead bricks were placed in front of the rod, which limited the width of the source plane to about 7 cm. This was done to remove counts that

would arise from portions of the source outside of the collimator's field-of-view. The rod has a width of 2 mm and has a dotted structure along its length. 1 cm long lead pieces are wrapped around the rod, spaced 1 cm from each other down the length of the rod. Moving down the length of the rod, γ-rays should be emitted for 1 cm, then blocked for 1 cm, then emitted for 1 cm, and so forth. With the lead bricks in place, only four emitting segments were visible to the detector. These four segments should be apparent in the reconstructed images.
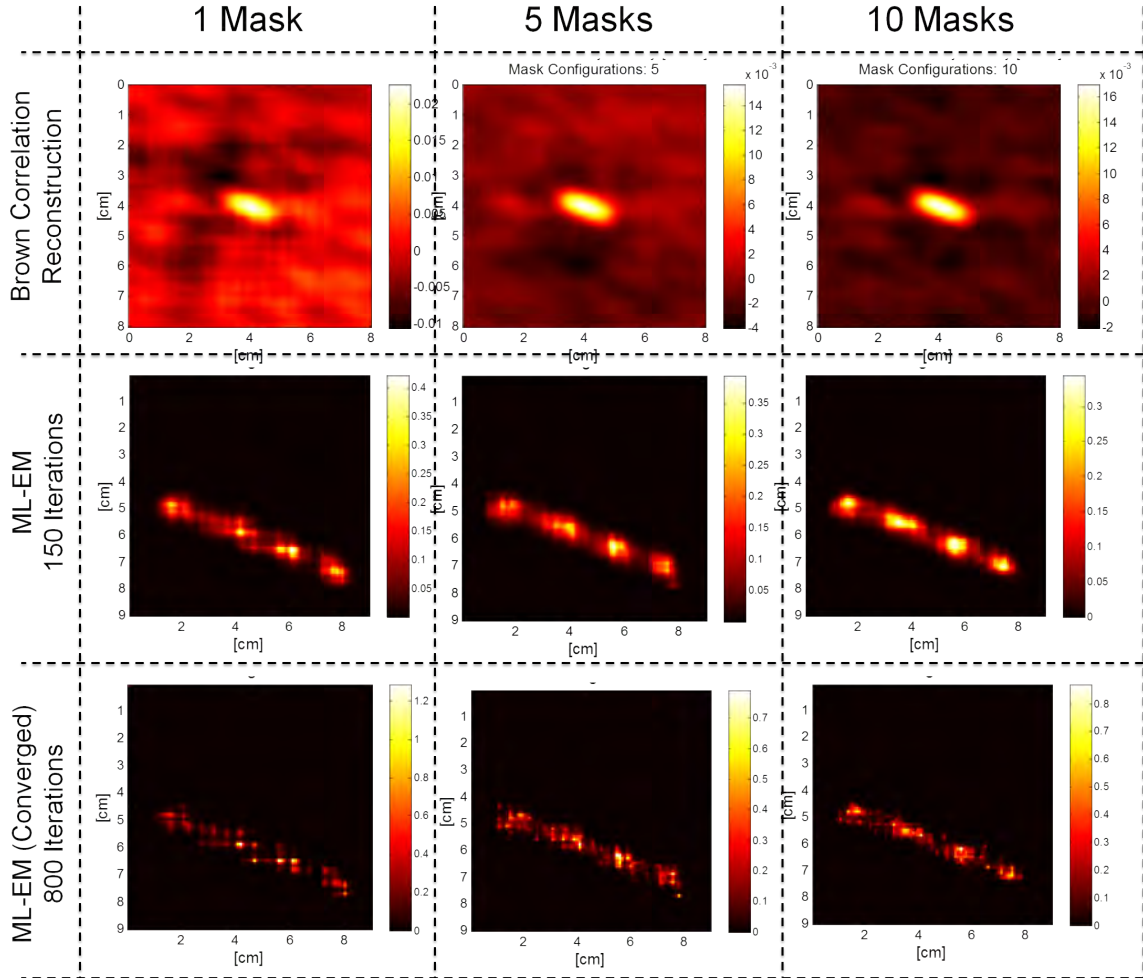
Figure 47. Images of the intermittent rod using Brown correlation, ML-EM with 150 iterations, and ML-EM with 800 iterations. 1, 5, and 10 mask sequences are shown.

The correlation methods poorly reconstruct the images of the rod. The inherent noise does decrease when more mask pattens are used, but the signal portion is still not very good. The correlation techniques suffer drastically from the vignetting effects. Most coded-apertures are nowhere near as deep as the programmable collimator. Most of the effort for this project was given to the ML-EM method. Compensation for the vignetting effects in the correlation methods could be included in a future test, if desired.
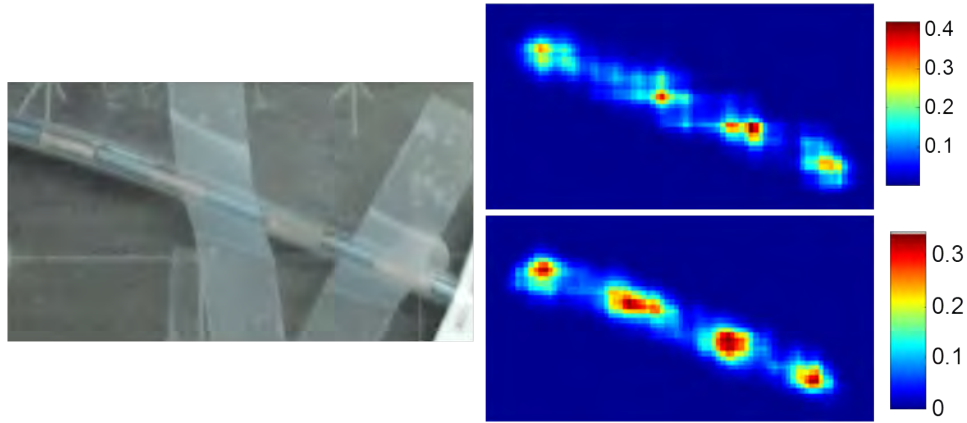
Figure 48. Left: Picture of the Rod. Top-Right: The ML-EM image reconstruction using 1 mask, zoomed. Bottom-Right: The ML-EM image reconstruction using 10 masks, zoomed.

The ML-EM reconstructed images are much better. With 1 mask some of the segmentation in the rod is visible. With 10 masks the emitting segments of the rod are clearly visible. The 10-mask image is a significant improvement. Notice also that the maximum value of the colorscale decreases when more masks are used. The 1-mask image is peaked in an unphysical way. The emitting segments emit uniformly across their lengths, as shown in the 10-mask image.

5.4.5   Co-57 Rope

The Co-57 rope was imaged, but only with up to a maximum of five masks. No shift correction was performed on the rope images. As with the intermittent rod, two lead bricks were placed in front of the rope, limiting the width of the source plane to about 7 cm. About 31,000 events were recorded for each total datarun, within the energy window. The rope lacks the intermittent structure of the rod. The width of the rope is 2 mm. Again, the correlation method did not perform very well. Inherent noise decreased when more mask patterns were used, but the source is only visible at the center of the reconstructed image because of vignetting effects. The ML-EM method reconstructed the image fairly well.
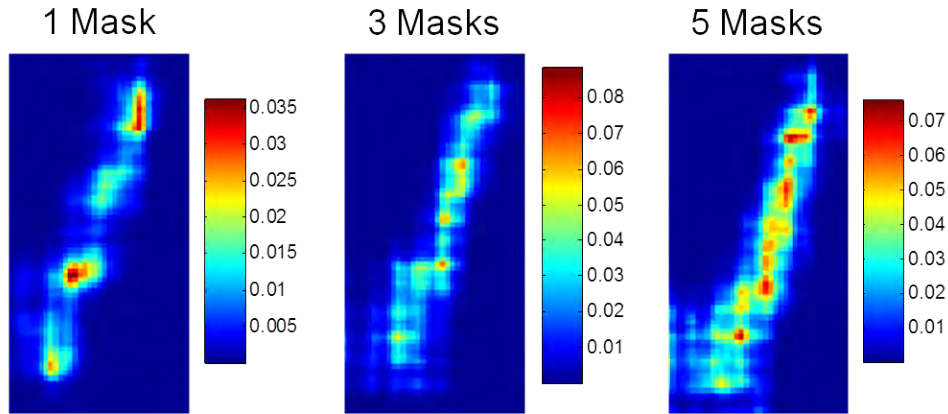
Figure 49. Zoomed view of the rope after 1, 3, and 5 masks, ML-EM, 150 iterations.

The 1-mask ML-EM reconstructed image is blotted in an unphysical way. The source strength should be uniform along the length of the rope. This blotting is less noticeable in the 5-mask image. In some ways the 3-mask image is better than the 5-mask image, especially with regard to the lower half of the rope. A zoomed version of this lower portion is given in Figure 49. Unfortunately, this source was only imaged with up to five masks. If ten masks had been used, the final image would have been

much better. In the case of the rod, most of the improvement occurred between 5 and 10 mask sequences.
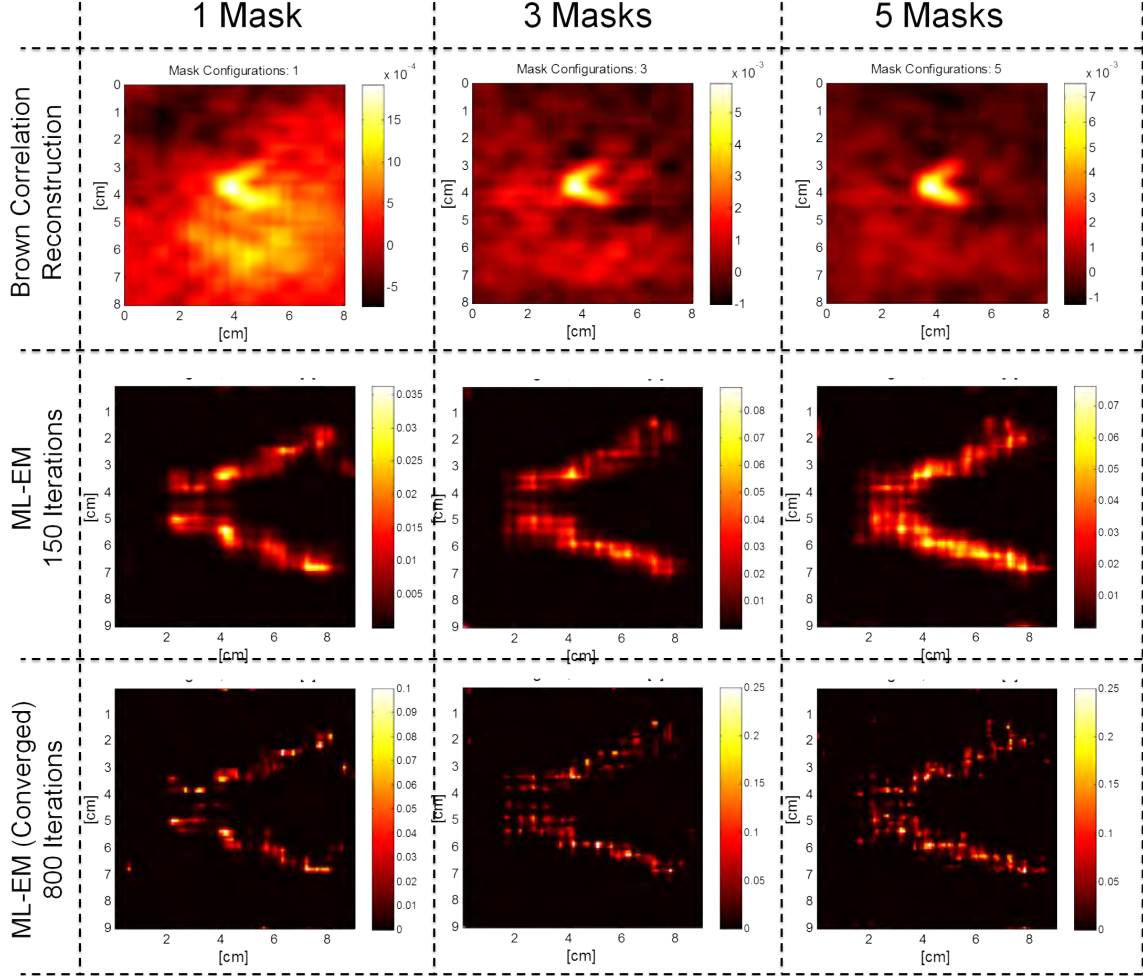
Figure 50. Images of the rope using Brown correlation, ML-EM with 150 iterations, and ML-EM with 800 iterations. 1, 3, and 5 mask sequences are shown.

The rope takes up more of the source plane than did the rod, resulting in more noise. The coded-aperture multiplex advantage decreases as a larger portion of the field of view is taken up by the source. Nevertheless the image did improve when more masks were used.

5.5 Discontinuities in the SNR from Correlation Decoding
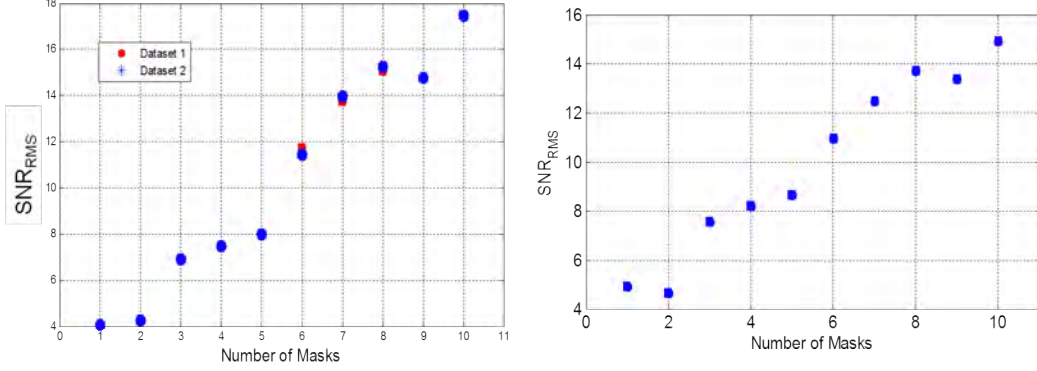
Figure 51. Left: SNR$_{\mathrm{RMS}}$ for the Co-57 button source, as a function of number of masks used, correlation decoding. Right: SNR$_{\mathrm{RMS}}$ for the Cd-109 source with background, as a function of number of masks used, correlation decoding.

Regarding images reconstructed with correlation methods, significant discontinuities are present in the plots of SNR$_{\mathrm{RMS}}$ versus the number of masks used. For both the Co-57 source and the Cd-109 source, these discontinuities occur between 2 and 3 masks and between 5 and 6 masks. First it was thought that this effect was caused by the way in which the signal circle was chosen. The circle which cuts out the signal portion of the image is chosen qualitatively. If this circle is too small, then the variations in the signal shape might cause a piece of the signal to lie outside of the circle, meaning that some of the signal would be counted as noise. To test for this effect, the radius of the circle was increased. The SNR$_{\mathrm{RMS}}$ results were about the same, though shifted downward due to more noise being included in the signal list. Ultimately, the actual sizes of the sources were used for the signal circle.

Another possibility considered was that masks 3 and 6, chosen at random, just so happened to have good correlation properties. Recall from Section 2.1 that the term $A \star G$ should approach a δ-function as nearly as is possible, where A is the mask

87
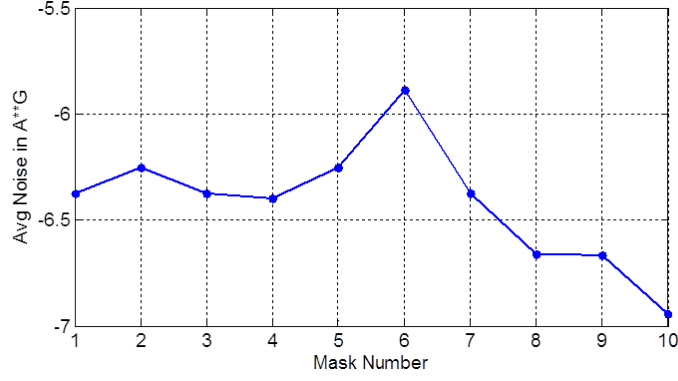
Figure 52. The average noise in $A \star G$ versus the number of masks used. Here lower values mean that $A \star G$ is closer to a δ-function

pattern, G is the Brown matched filter, and $\star$ is the 2D cross-correlation operator. The correlation of each mask pattern with its matched filter was calculated. When a Brown filter is used, the central spike of $A \star G$ always will be zero. As the noise in the rest of the matrix decreases, becoming more negative, the term more closely approximates a δ-function. These results are shown in Figure 52. Certainly some of the mask patterns have better correlation properties than others. This can be considered in future work. However, the shape of the curve in Figure 52 does not explain the discontinuities in Figure 51.
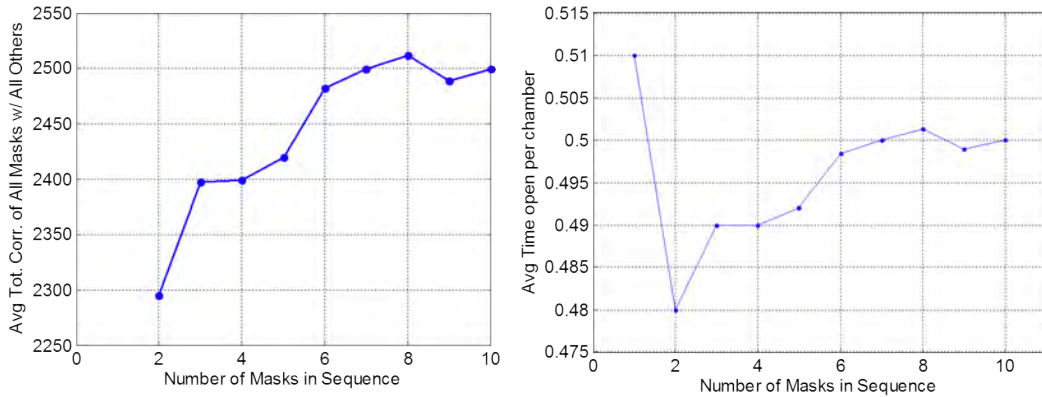
Figure 53. Left: The average correlation of a given mask and all other masks versus the number of masks used. Right: The fraction of time in which the average chamber is open to γ-rays versus the number of masks used.

In fact, the data presented in Figure 53 are needed to explain the discontinuities. The left-hand plot shows the average cross-correlation between one mask and all of the other masks in the sequence. The right-hand plot shows the fraction of time in which the average chamber is open, as a function of the number of masks used. Notice that for sequences greater than 1 mask, the two plots are identical but for ordinate scaling. This is not surprising, given the relationship that was established between mask independence and the fractional time that each chamber is open, as explained in Section 3.3. It was shown that the least correlated sequence, or the sequence in which the mask patterns were most independent, is that in which each chamber is "on" and "off" for equal durations. To have non-trivial mask patterns, the "on" and "off" durations cannot be guaranteed as equal except at the end sequence with the maximum number of masks.
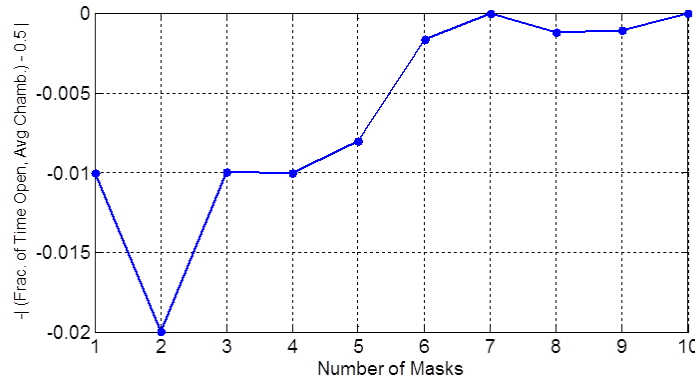
Figure 54. The fraction of time in which the average chamber is open was subtracted from the ideal fractional duration, 0.5. The negative of the absolute value was plotted.

Perhaps the most enlightening version of the data is given by Figure 54. In this case, the fractional time in which the average collimator chamber was "on" was subtracted from the ideal fractional duration of 0.5. The negative absolute value of this difference was then taken. Notice how similar Figure 54 is to Figure 51. Clearly

89

the fractional duration for which the average chamber is "on" implicitly drives the degree to which SNR increases.

5.6 MCST Uncollimated Forward Problem

5.6.1 Results

The different metal samples were examined for different periods of time. It was found empirically that about 24 hours of data were required to get significant Gaussians in each of the subpixels, given the setup used. In the first test to be evaluated, a copper strip was secured to the fishing line and data were taken for 24 hours.

An energy spectrum for each of the detector pixels was required from the detector software. In one mode the software will export all of the events that it detects, between a certain energy window, into a text file. Originally the window was set so that events with energies between 60 keV and 80 keV were recorded. Later this was changed to accept events between 53 keV and 83 keV, so as to allow the Gaussian fit routine to have a better baseline. Each line of the file corresponds to a given detector event and gives energy, event pixel, etc. A parser was written in MATLAB® to transform the data from the raw events into energy histograms for each detector pixel. These data were stored as a three-dimensional mat-file.

MATLAB® is equipped with a built-in function for fitting a Gaussian distribution to data points using a least-squared algorithm. The function does not allow for an offset in the data, however. Another script was written which first imports the mat-file containing the energy spectra. For each spectrum, the script finds the average of the first ten data points as well as the average of the last ten data points. A line is made between the two averages, and this line is subtracted from all of the data. Next, the Gaussian fit function is performed for all spectra. The line is then added back to both the fit and the raw data. The Gaussian function outputs the Full Width at
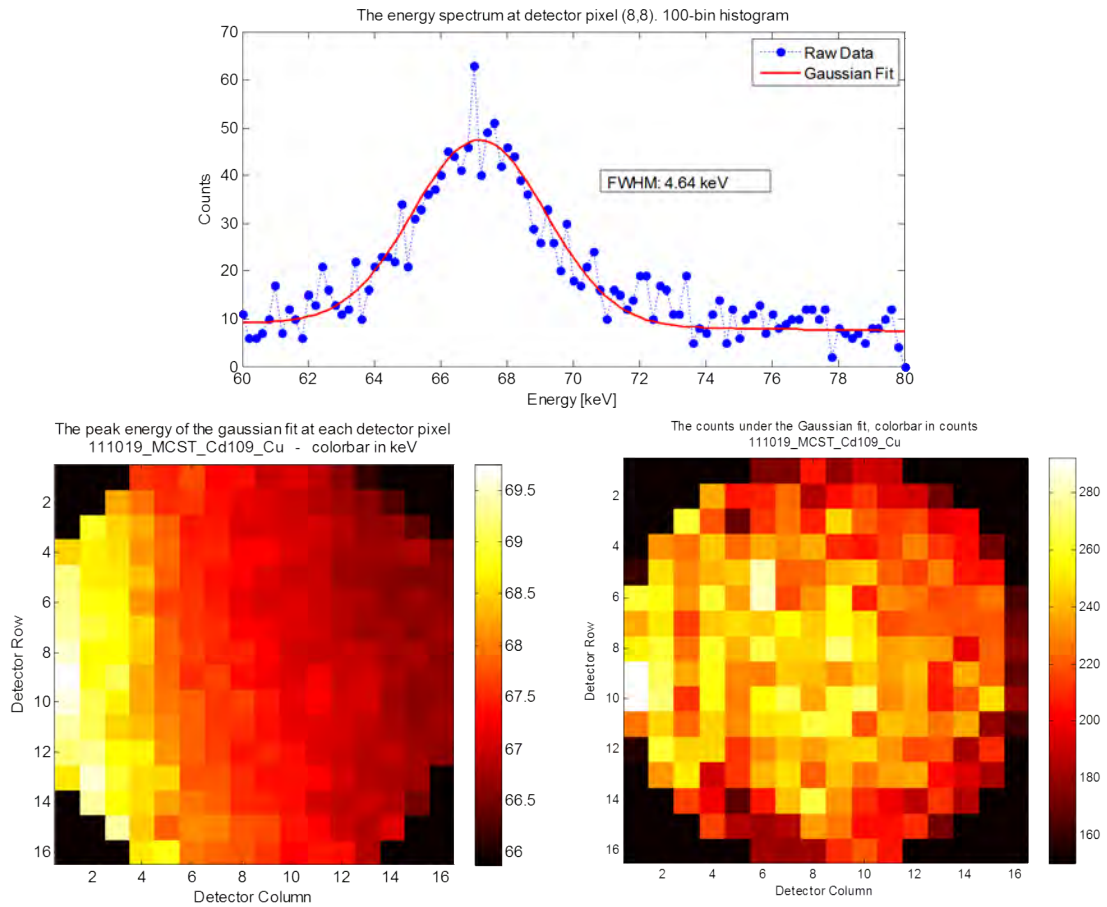
Figure 55. Selected data from a test using a single copper sample. Compare with the model predictions shown in Figure 16. Top: The energy spectrum from a single detector pixel, with its Gaussian fit. Left: The energy of the peak of the fitted Gaussian in each detector pixel. Right: The number of counts under each fitted Gaussian for each detector pixel.

Half Maximum (FWHM) and the Root Mean Squared (RMS) error of the fit, among other things. The number of counts for each pixel is an important number for MCST. The Gaussian fit is integrated using an adaptive quadrature method, also built-in to MATLAB® . This integration gives the number of counts attributable to Compton events in the sample.

The pixels that lie on the corners of the detector will receive significantly lower counts than the rest of the pixels, because they are physically smaller. For the experiments conducted, these corner pixels typically received too few counts for a Gaussian fit to be reliable. Thus, the data and the fits from these pixels were discarded. With higher count rates these pixels could be utilized. However, the model must first take their lower effective efficiencies into account.
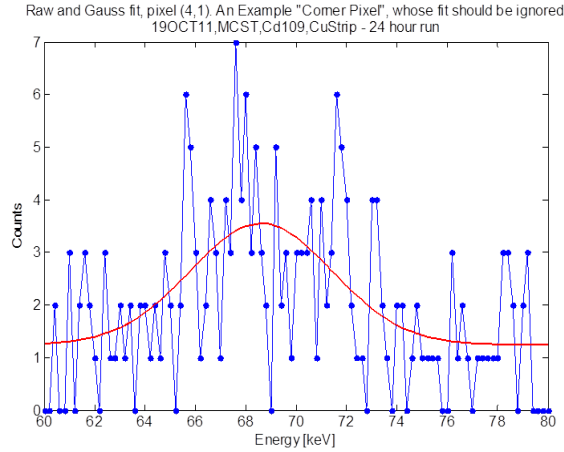
Figure 56. One of the corner pixels, for the same data shown in Figure 55. Notice the low number of counts.

In the results shown in Figure 55, where a copper sample was examined, the average FWHM of the Gaussian fits was found to be 4.91 keV. The average RMS error of the fits was 5.36 counts. The average number of counts into each pixel was 366. Something to consider is that the samples used are not as small as the potential

resolution of the system. FHWM values add in quadrature. That is,

$$R_{\mathtt{tot}} = \sqrt{R_1^2 + R_2^2} \tag{32}$$

where R stands for resolution, given here by the FWHM. The detector has an energy resolution of about 1.4 keV at 88 keV, as was found in a test. The size of the metal could be reduced substantially before the limits of the detector are reached.

In another test the copper sample was cut down to a quarter of its former area. All other parameters were held fixed. It was thought that the FWHM would decrease. However, the average FWHM was calculated as 5.74 keV, with a fit RMS error of 5.44 counts. The average number of counts was 288. And so, by quartering the size of the copper strip, the resolution did not change much, although the number of counts received by the detector did change. This means that the resolution of an MCST system could be very small, if perfected.

In a further experiment aluminum was used instead of copper. Aluminum has a significantly lower Z than copper (13 versus 29). One would expect the counts received from the aluminum to be significantly lower than from copper. Two tests were conducted, both over 24 hours, with the same geometry. The resolution and RMS error between the two tests was comparable. The average number of counts received from the aluminum sample was found to be 272 which is substantially lower than the 366 counts received by the average detector pixel in the copper test. These results indicate that the system could successfully differentiate between materials with different electron densities.

A CuCu and an AlCuCu (Figure 20) phantom were tested using the system, as described in section 4.3. The results from each are comparable, with those from the AlCuCu phantom shown in Figure 57. The built-in MATLAB® routine has the ability to fit multiple Gaussian distributions to data. However, it was wholly unsuccessful at

fitting multiple Gaussian distributions to these data. The Gaussian distributions are simply too close together, in energy, for that routine to work. More robust methods are necessary. The PWLS algorithm is one choice, although ML-EM may be usable as well.
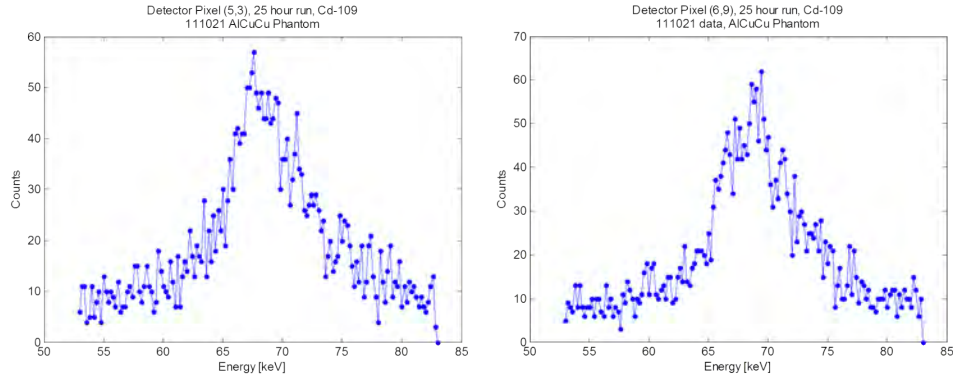
Figure 57. Spectra received from the AlCuCu phantom, taken from two different detector pixels.

5.6.2 Discussion

The results found from the basic MCST setup are in good agreement with the MCST forward model predictions. A change in detected photon energy across the face of the detector crystal is certainly apparent. The coded-aperture results give some insight into how the programmable collimator might help with MCST. In MCST, photons are scattered within the sample and the scattered photons are then detected. Effectively the sample can be thought of as an extended source, similar to the rod and the rope as presented in Section 5.4.5. Just as the programmable collimator improved the images of the rod and rope, so it would improve the images of an MCST source.

In the coded-aperture experiments, photon energy is removed from consideration. The energy of the photons emitted from the radionuclide was known, and the detector

94

was set only to record photons of that energy (plus or minus a few keV). In this way, Compton scattered photons were removed from consideration, resulting in less noisy images. In MCST, however, the photon energy is needed in the reconstruction process. This requirement introduces another dimension of complexity that was not considered in the coded-aperture experiments.

The HPGe strip detector used in this study is uniquely suited to handle MCST. HPGe detectors have very good energy resolution [37]. The pixel size and number of pixels is comparable to detectors made of other materials. Both position sensitivity and precise energy sensitivity are required for MCST. The one disadvantage of the HPGe strip detector is its low efficiency. Perhaps the efficiency could be increased using Compton rescue [67].

Evans discovered that for three-dimensional MCST, some sort of physical constraint was required, typically taking the form of collimation [25]. Without collimation, the ill-conditioned matrices would not converge during the image reconstruction process. With collimation, the parameters could be sufficiently bounded to allow for convergence. This is where the programmable collimator applies to MCST. The term multiplexing has been used throughout this document. When applied to MCST, multiplexing simply means that each detector pixel receives information about more than one pixel in the sample. The sample is discretized, and if any of the detector pixels detect scattered photons from more than one of the sample pixels, then multiplexing is occurring.

A balance must be struck between multiplexing and the reconstruction program's ability to converge on a solution. More multiplexing means lower detection time. In medical imaging, more multiplexing means a lower patient dose rate of ionizing radiation. In materials investigation, more multiplexing could mean real-time images with good quality. On the other hand, as mentioned above, if the multiplexing becomes
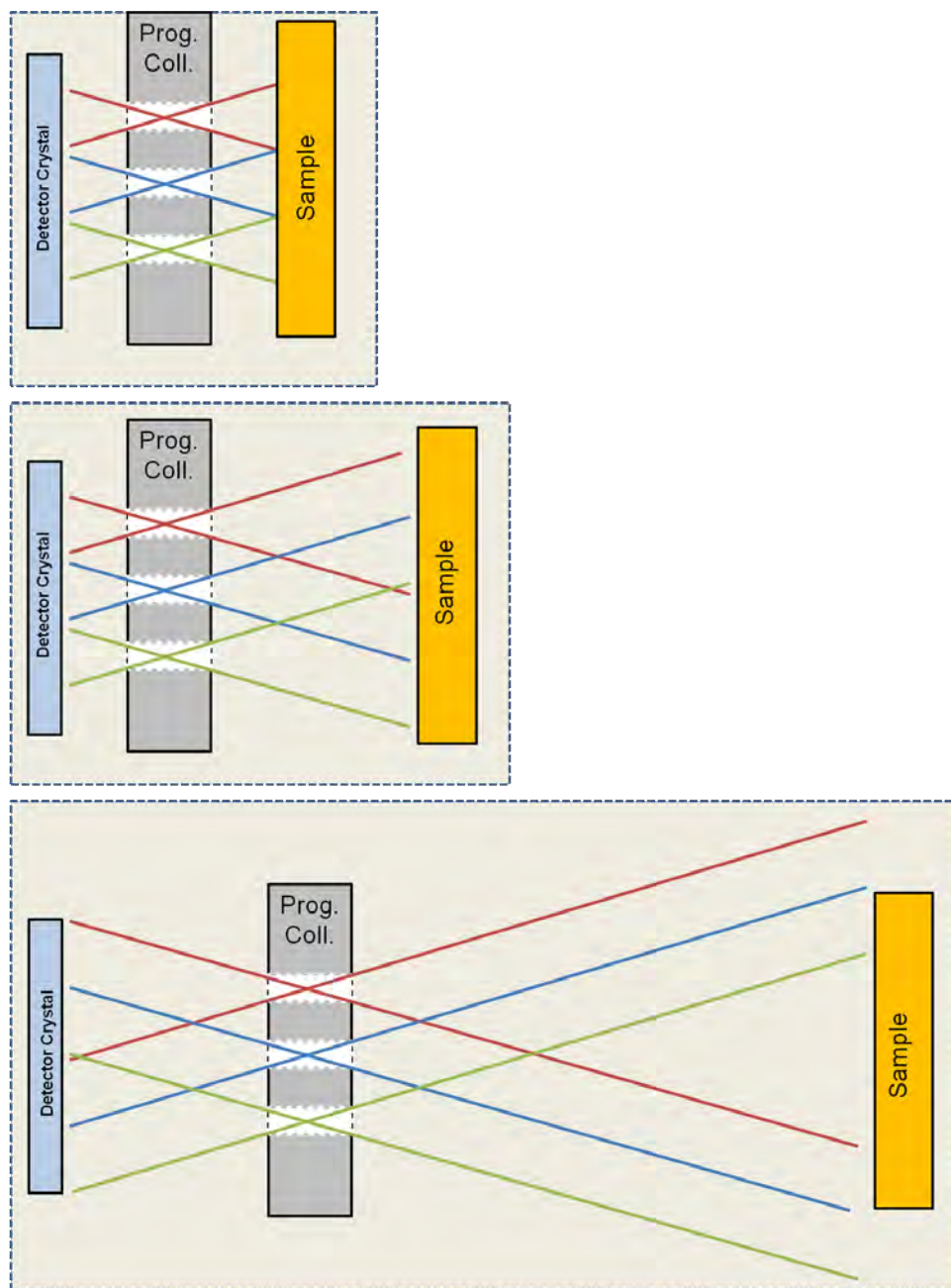
Figure 58. The level of multiplexing is determined by the sample-collimator and collimator-detector distances. Top: little to no multiplexing. Middle: medium multiplexing. Bottom: High multiplexing.

too great, the ill-conditioned matrices will not converge during the image reconstruction process. Or, if convergence does occur, the images might be noisy and unusable if there is too much multiplexing.

The programmable collimator could be used to limit the problem while still allowing for multiplexing. In the coded-aperture experiments, the collimator depth was a detriment. In MCST, the collimator's depth could be used as an advantage, providing geometric constraints. By adjusting the sample-collimator and collimator-detector distances, the level of multiplexing is adjusted. The multiplexing can be tinkered with by the experimenter until the optimal setup is found. Then, by using the programmable collimator, the overall SNR should increase because of the multiple, semi-independent views afforded to the detector. Just as the images of the extended sources in the coded-aperture experiments improved, so would the MCST images improve when multiple mask patterns are used. The multiple masks would further chop up the isogonic arcs found from the Compton formula (Figure 7).

5.7   Programmable Collimator Physical Performance

The use of the programmable collimator was hampered by several factors throughout its life. First, the square chambers were a bit more difficult to machine than circular chambers would have been. It was impossible for the wire EDM to cut chambers with perfectly square cross sections into the grid block. The corners were rounded. The square PEEK plugs had to be filed and broached individually. In effect, each plug was custom-made for its particular chamber. Although the square chambers are better for calculations and allow more throughput, circular holes might be considered in future designs to decrease construction time.

Secondly, the plugs had to fit tightly into the chambers to prevent AIM-70 from leaking out of the front of the device. Often they were so tight that the plugs would

break when being pulled. There was a danger of pulling a given plug all the way out of its chamber, as described in Section 4.4. To prevent spillage of AIM-70, the collimator was evacuated of AIM-70 before the mask pattern was reconfigured. The collimator was then refilled with AIM-70. The entire process of changing the mask configuration took from 1-2 hours. Such a lengthy procedure is tolerable for a proof-of-concept experiment, but a better system is desirable.

Finally, portions of the grid block cracked and chipped away during the programmable collimator's use. This was probably due to the stress placed on the grid walls when the AIM-70 cooled and expanded. Potential solutions are given in Section 6.4.

VI. Conclusion and Path Forward

6.1 Summary

The first fully reconfigurable programmable collimator using a liquid attenuator was designed, built, and tested. The programmable collimator was considered in two modes, as a coded-aperture and as a problem constraining device for MCST. For the coded-aperture application, an MCNP simulation was conducted in order to better understand the problem. A MATLAB® script was written to find the sequence of least-correlated random mask patterns, so as to have the most independent views possible of the object plane. A ray-tracing model was created in MATLAB® to characterize the forward problem, providing the necessary information to the ML-EM algorithm. Vignetting effects, the shape of the detector crystal and dead subpixels were factored in to the forward problem, increasing accuracy. An experiment was constructed to test the device as a coded-aperture.

Three decorrelation techniques were evaluated using the experimental data. The decorrelation techniques were useful because of their simplicity and computational speed. The ML-EM method was also evaluated. It generally performed better than the decorrelation techniques with respect to SNR, though the greater number of tweak-able parameters makes the method significantly more complex. ML-EM is also much more computationally expensive than the correlation methods. Regardless of the method, the programmable collimator is demonstrably effective as a coded-aperture. A sequence of ten mask patterns was used, and the SNR increased with the number of mask patterns used. This promising result suggests that the programmable collimator could significantly improve coded-aperture technology. A sequence with twenty or more mask patterns should be tested in the future in order to determine at how many masks the SNR will peak over a constrained, total detection time.

A model was developed for MCST, based on the Compton equation and the Klein-Nishina formula. An experiment was conducted in which small samples were placed in front of a mono-energetic source and the scattered photons were measured. The experimental results suggest that Compton scatter tomography is possible with the PHDs DSSD. A robust method like PWLS would have to be used in order to unfold the individual responses from all of the sample voxels. In the past, MCST has failed because it is too highly multiplexed and thus becomes ill-conditioned and unsolvable. The programmable collimator may be able to physically constrain the problem, allowing convergence on a solution. The problem would still be multiplexed to some extent, but not so multiplexed as to be unsolvable. By having some multiplexing, performance would increase relative to the highly collimated systems used today.

6.2 Practical Uses

Please see Sections 2.5 and 2.6.5 for background information.

6.2.1 MCST

The programmable collimator should be a viable constraining device for MCST. MCST has several potential uses. In medical imaging, Compton scatter dominates as the mode of interaction in the patient's body [7]. Most systems ignore and attempt to filter out the photons that were Compton scattered within the subject. If those events were utilized, image fidelity would increase and/or dose to the patient would decrease. 3-dimensional images could be made more readily with the additional information gained from Compton scatter events. Likely, a conventional system would be augmented with a programmable collimator detector.

Another potential system would measure Compton scattered photons exclusively. Such a system would be useful for industrial cases in which access to only one side

of a sample is available. In this case the physical collimation from the programmable collimator would be a necessity. Without collimation, the problem is too multiplexed to solve. The programmable collimator would help to decrease detection time or source intensity.

6.2.2   Unmanned robots or UAVs

A detection system utilizing programmable collimation would be useful for UAV and unmanned robot applications. The unmanned vehicles could be used to survey large areas after a nuclear explosion or subsequent to wide-area dispersion of nuclear material following a dirty bomb attack or a reactor accident. Inexpensive position sensitivity would help to limit the time required to map the contamination over a large area. Lower detection times are especially enticing given battery life constraints in remotely controlled devices. Unmanned vehicles could also be used to sniff out nuclear weapons before they are used, if other intelligence provides a general location for the nuclear device. Inexpensive position sensitivity would help to find the nuclear material more quickly. Also, collection of radioactive effluents is an important component of several treaty-monitoring organizations. A position-sensitive system would help to guide members of these organizations toward the proper locations where effluent content is highest.

6.2.3   Space Surveillance

Programmable collimation would not be advantageous for space-based detection of nuclear events on the ground. The duration of γ-ray output from a nuclear weapon is too short for a changing collimator to be of any real use. However, the idea of using multiple masks is still valid. Several small satellites could be equipped with collimators that have different mask patterns. The mask patterns would be

chosen such that each satellite would receive the most unique information possible. Knowing the location of each satellite precisely, the images from each satellite could be combined to form a better image than could be found from a single satellite.

6.2.4 Space-based Gamma-Ray Astronomy

Programmable collimation most certainly could be useful for γ-ray astronomy. Gamma Ray Bursts (GRBs) have durations on the order of minutes, meaning that many mask patterns could be used as the event occurs. SNR and image resolution of the GRBs would thus increase significantly relative to current imaging systems. For many years coded-apertures have been used aboard satellites for astronomy, successfully. Programmable coded-apertures are a logical next-step. An array of smaller satellites equipped with programmable coded-apertures could outperform the massive, bulky satellites used currently. The reconfigurability of the collimator would eliminate the need for the satellite rotation.

6.2.5 Medical Nuclear Imaging

Coded-apertures have been effectively demonstrated in Single Photon Emission Computed Tomography (SPECT) and Positron Emission Tomography (PET). Programmable coded-apertures represent a logical progression in that branch of imaging. Regardless of the coded-aperture setup used, programmable collimation can increase the image resolution. In medical situations there is adequate time for multiple mask patterns to be used. The ultimate result of programmable collimation would be better images or lower dosage given to patients.

6.2.6 Position Sensitivity from a Single Detector Crystal

Perhaps the most enticing application for the programmable collimator is that it could give position sensitivity to a single detector. If this could be achieved, the price for a position-sensitive detector could be reduced substantially. An ideal setup would be to combine a NaI detector and a programmable collimator. The NaI detector has relatively good energy resolution. For many applications, cost is the limiting factor with regard to position sensitive detectors. An inexpensive, position and energy sensitive detector would be helpful in all of the applications listed above. For the space-based astronomy application, NaI detectors also have much lower power requirements than HPGe strip detectors and are more resistant to vibration.

The ease with which the programmable collimator was modeled suggests that position sensitivity could be given to single detector. Only iterative methods could be used for that type of problem.

6.3 Future Work

Throughout this project, several areas have been highlighted which would benefit from further investigation. Based on the current setup, one could:

- Characterize the efficiency of each subpixel in the HPGe strip detector. In this work, all subpixels were assumed to have equal efficiencies. This is not the case due to constructional variations, varying pixels sizes, and nonuniform charge movements. A characterization experiment would require that a highly collimated source be precisely moved such that one subpixel is irradiated at a time [75]. Comparison of counts would provide efficiency.

- Incorporate more effects into the forward model. In this work Compton scattering within the programmable collimator was ignored, as well as attenuation

through the PEEK plugs. If the ML-EM algorithm is supplied with a more accurate model that includes those factors, and others, it would provide a better estimation of the source plane.

- Use more active sources or longer detection times so as to have better counting statistics. In this research, data and collection times were limited. An increase in either of those areas would help to rule out poor counting statistics as a cause for artifacts in the reconstructed images. Counting statistics were especially poor in the MCST testing.

- Perform an experiment to determine the limit on the number of mask patterns used, given a constant total detection time. In this work, the image quality increased as more mask patterns were used. However, if the overall detection time is limited, then each mask is used for a shorter duration as the number of masks increases. Eventually, if too many masks were used, there would be too little time to formulate an image through each mask. Thus, the performance increase has a peak with respect to the number of mask patterns used.

- Image γ-rays of higher energies. A dynamic collimator was considered necessary for high energy γ-rays that are able to penetrate the "off" portions of the collimator [16]. Multiple mask patterns should effectively overcome the noise introduces because of penetration through the AIM-70, but that experiment needs to be performed.

- Determine how to choose mask patterns on the fly. A computer routine could be developed to use incoming data in order to make an educated decision on the remaining mask patterns. The collimator could start with a high pinhole density, allowing maximum throughput. Then, as a rough source position is determined, pinhole density would decrease so as to increase resolution. In this

104

way a sharp image could be found in minimal time even when viewing a wide area.

Changing the experimental configuration, one could:

- Place the programmable collimator in front of a single, NaI detector. It may be best to perform simulations first, in order to understand the best setup that would provide position sensitivity to the single detector.

- Use a setup similar to that presented in Section 4.3, testing the programmable collimator as a physical constraint on the MCST problem. A forward model would have to be developed first, analogous to that presented in Section 3.1.

- Image a three-dimensional source. In the forward model for ML-EM, the source region would be divided into 3D voxels, rather than 2D pixels. Multiple mask patterns and changes in magnification would allow a 3D source to be imaged without moving the collimator-detector assembly. In other words tomography could be performed without rotating the detector around the sample.

6.4 The Future of Programmable Collimation

The next design would be similar to the current design, with a few notable differences. The collimator would have a greater number of smaller holes, with each chamber being about 2 mm wide so as to better conform to current coded-aperture designs. With more chambers, the URA and MURA mask patterns could be attempted, although it is unclear whether or not those classes of mask patterns would be optimal for ML-EM. It may be that a better class of mask patterns exists for ML-EM. Secondly, the collimator could be made with less depth, reducing vignetting. Thirdly, the holes could be made round, to substantially reduce construction time.

105

High temperature O-rings could be placed around the plugs to prevent leakage and to allow easy movement of the plugs. Fourthly, screw patterns could be tapped into each plug, so that the actuator rod could screw into the plugs to move them. This might prevent the plugs from breaking, though stripping might be an issue.

A different liquid attenuator should be considered prior to the construction of the next device. Mercury is ideal. It has a high Z (80), making it a good γ attenuator. Plus, mercury is already a liquid at room temperature, removing the need for heating apparatuses. Unfortunately, mercury is difficult to procure, due to its toxicity. Other eutectics or near-eutectics could be a possibility. A few are shown in Table 7. The lack of toxicity would be helpful, in order to eliminate the need for a hood or breathing equipment. A lower melting point would be useful. A material that does not expand upon solidification is desired, in order to prevent long-term damage to the programmable collimator.

Table 7. Potential Candidates for the liquid γ attenuator [13, 6, 76].

Name	Melting Point [C]	Expansion After Solidifying [inch per inch]	Toxic?
AIM-70	70	+0.005	Fumes,Ingest
Mercury	-38.83	-	Yes
AIM-47	47	+0.0002	Fumes,Ingest
AIM-58	58	+0.0002	Ingest

The ultimate goal for the programmable aperture is a device with many more smaller chambers that is fully computer-automated. Toward that goal an experimental system could be built where pipettes full of the liquid attenuator are used. The liquid attenuator could manually be squeezed in and out of the chambers. Holes perpendicular to the chambers would be drilled in the PEEK (or another lightly at-

106

tenuating, machinable plastic) on each side of the chamber block, forming two mani-
folds. The manifolds would allow the liquid to be pumped either into the chambers
or out and away from the grid block. Eventually a pump system would be needed
to fully automate the system. The attenuator could be a molten metal, as in this
study, a liquid metal like mercury or something else entirely. The chambers would
be fabricated to a small enough diameter so that the capillary action in the liquid
attenuator would match gravity, ensuring that each chamber is filled vertically. This
would allow for any possible orientation of the device. Either positive air pressure or
a non-attenuating liquid would be needed on both sides to hold the liquid attenuator
in the chamber. Low cohesion between the liquid attenuator and the other parts is
desired so that when a given chamber is evacuated no liquid attenuator remains.
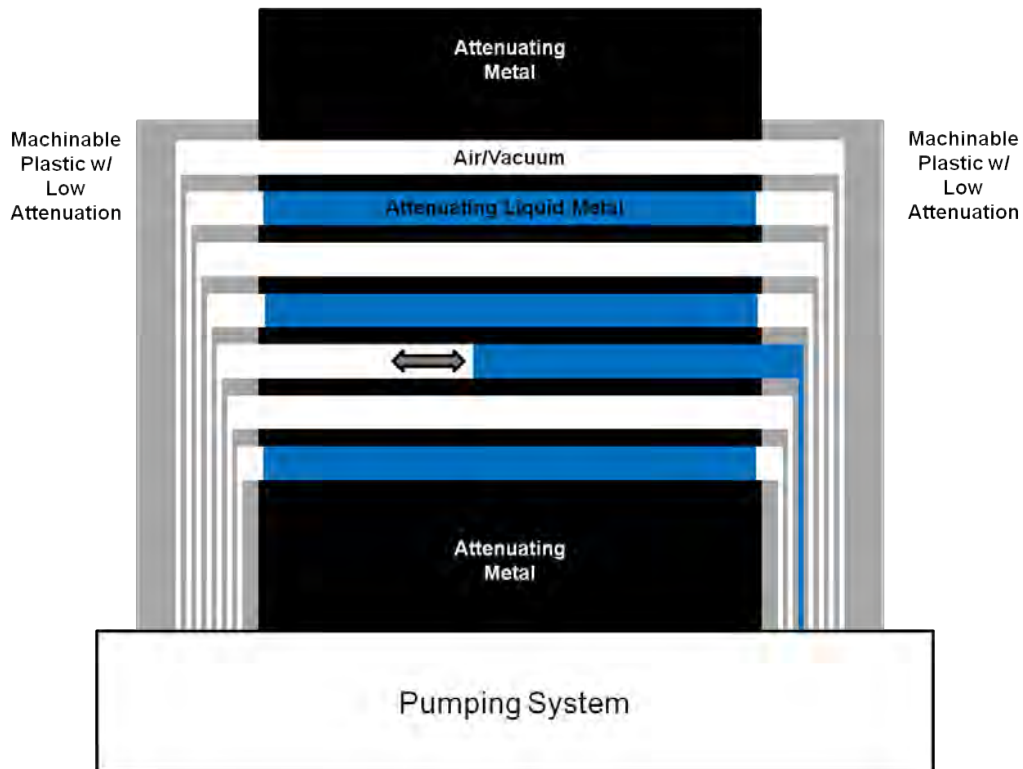
**Figure 59. A future programmable collimator. A pumping system would fill or evacuate
each chamber with an attenuating liquid. Plastic manifolds on each end of the grid
block would guide the liquid from the pumping system into the chambers.**

A device that can quickly switch to new mask configurations would allow different views to be made of the object. With an automated coded-aperture, hundreds of different mask configurations could be used in short order. Though each configuration would not be fully independent from the others, the sheer number of different perspectives would certainly increase the resolution and accuracy of the imaging system. The programmable collimator could be fabricated in a converging or diverging pattern in order to make a coded-aperture that zooms in or out on a scene, *à la* Rothenbush [58].

Appendix A. MATLAB Code

Following is a list of MATLAB code used for this research. Note: Indentation has been removed for brevity. If the user presses ctrl+a and then ctrl+i in MATLAB® the indentation will be automatically restored.

1.1   The Least Correlated Mask Sequence

Listing A.1.

```matlab
1 % Mask Sequence that is least correlated with the least user ...
     movements
  % In this script, a sequence is first constructed where each ...
     element is on
  % and off for equal periods of time. The masks are otherwise ...
     random. The
  % code will then look at this sequence, and reorder the masks so ...
     that the
  % programmable collimator user will have the least amount of ...
     switched
6 % elements
  % 2d Lt Jack FitzGerald, AFIT/ENP, 18OCT11

  clear all
  close all
11 clc

  NumSeq = 4;     %number of masks in the sequence MUST BE EVEN
  MaskSize = 10;  % length of row/column in masks MUST BE EVEN, ...
     SINCE LOOKING AT CENTER ELEMENT IN CORRELATION MATRIX
  rho_min = 0.5; % minimum pinhole density (open elements divided by...
     total elements)
16 rho_max = 0.5; % max pinhole density

  %% Create a mask in which all elements are "on" and "off" for ...
     equal periods
  % of time
  for i = 1:MaskSize
21 for j = 1:MaskSize

  halfcheck = 0;
  while(halfcheck == 0)
  TimeArray = round(rand(NumSeq,1));  %Make time array to populate ...
     sequence
26 OpenElement = 0;
  for time = 1:NumSeq
  if(TimeArray(time) == 1)
```

```matlab
        OpenElement = OpenElement + 1;
    end
31  end

    if (sum(OpenElement)) == (NumSeq / 2)    %Check to see if time ...
        array is "on" and "off" for equal durations
    halfcheck = 1;
    end
36  end

    for time = 1:NumSeq
    Seq(time,i,j) = TimeArray(time); %Populate sequence with time ...
        arrays
    end
41  end
    end

    %% Check correlation between one mask and all others in the ...
        sequence

46  for i=1:NumSeq
    for j = 1:(i-1)
    CorrOldMat = xcorr2(reshape(Seq(i,:,:),MaskSize,MaskSize),reshape(...
        Seq(j,:,:),MaskSize,MaskSize));
    CorrOld(i,j) = CorrOldMat(MaskSize,MaskSize);
    CorrOldCoeff(i,j) = sum(sum(corrcoef(reshape(Seq(i,:,:),MaskSize,...
        MaskSize),reshape(Seq(j,:,:),MaskSize,MaskSize))));
51  end
    for j = (i+1):NumSeq
    CorrOldMat = xcorr2(reshape(Seq(i,:,:),MaskSize,MaskSize),reshape(...
        Seq(j,:,:),MaskSize,MaskSize));
    CorrOld(i,j) = CorrOldMat(MaskSize,MaskSize);
    CorrOldCoeff(i,j) = sum(sum(corrcoef(reshape(Seq(i,:,:),MaskSize,...
        MaskSize),reshape(Seq(j,:,:),MaskSize,MaskSize))));
56  end
    end

    OldSeq = Seq;
    CorrOldTot = sum(sum(CorrOld));
61  CorrOldCoeffTot = sum(sum(CorrOldCoeff));

    %Find time open and closed for average element
    OpenElements = zeros(MaskSize);
    for time = 1:NumSeq
66  for row = 1:MaskSize
    for col = 1:MaskSize
    if(OldSeq(time,row,col)==1)
    OpenElements(row,col) = OpenElements(row,col) + 1;
    end
71  end
    end
    end
```

```matlab
   OpenElements = OpenElements ./ NumSeq;

76 %% Reorder the sequence so that the user has the least number of ...
      element changes

   Permut = perms(1:NumSeq);   %Make matrix of all permutations
   NumPerms = numel(Permut(:,1));  % Find number of permutations

81 for i = 1:NumPerms
   changes = 0;
   for j = 1:(NumSeq-1)
   for row = 1:MaskSize
   for col = 1:MaskSize % Check to see if each element changes from ...
      one mask to the next in the seq
86 if ((OldSeq(Permut(i,j),row,col) == 1) && (OldSeq(Permut(i,j+1),...
      row,col)==0))
   changes = changes + 1;
   elseif ((OldSeq(Permut(i,j),row,col) == 0) && (OldSeq(Permut(i,j...
      +1),row,col)==1))
   changes = changes + 1;
   end
91 end
   end
   end
   ChangeTracker(i) = changes;
   end
96
   [MinChanges,MinChangeInd] = min(ChangeTracker); % Find permutation...
       with least element changes

   % Create the sequence with the least number of element changes
   for i = 1:NumSeq
101 LeastChangeSeq(i,:,:) = reshape(OldSeq(Permut(MinChangeInd,i),1:...
      MaskSize,1:MaskSize),MaskSize,MaskSize);
   end
```

1.2   ML-EM

Listing A.2.
```matlab
   % Programmable Collimator as a Coded Aperture - Forward Problem ...
      Simulation
 2 % Use same coordinate system as the MCST work
   % 2d Lt Jack FitzGerald, AFIT/ENP, 05DEC11
   % Outputs the A parameter for the ML-EM algorithm

   % Updated on 19DEC11 to over-resolve the detector, to account for
 7 % vignetting

   % For use with coarser simulations
   % Outputs A to a text file

12 % All distances in cm
```

```matlab
% Source is in "front", detector is "rear"

clear all
close all
clc

tic

%% Parameters
% DetResFact = the resolution of the simulated detector plane, D, ...
    relative
% to the actual detector  subpixel resolution
DetResFact = 10;
DetUnitFact = 20; %cm to 0.5 mm
%    Assume the detector is not crooked relative to crystal
ColXPos = 4.54; % Distance from front of crystal to back of ...
    collimator
ColZPos = 1.5; % Distance from bottom of crystal to bottom of ...
    collimator
ColYPos = 1.5;
DetZDim = 8; % Crystal is 8 cm tall
DetYDim = 8; % Crystal is 8 cm wide
SourceXDist = 52.6;  % distance of source plane from detector ...
    plane
SourceYDist = -1; %
SourceZDist = -1; % From Bottom of detector crystal to bottom of ...
    source plane
SourceZDim = 10; % Source plane height
SourceYDim = 10; % Source plane width
SourceResFact = 5; % change from cm to other resolution

InitCounts = 1000000;  %Counts from source, isotropic, arbitrary ...
    period of time
SteelAtten = 0.93;    % Attenuation through steel chamber dividers...
    (100 keV gamma through 0.05 cm of steel)

% Input the mask pattern
%{
G(1,:) = [0 0 1 0 1 0 0 0 0 1];
G(2,:) = [0 1 1 1 1 0 1 1 0 1];
G(3,:) = [1 1 0 1 1 0 1 1 1 1];
G(4,:) = [1 0 0 0 1 1 1 0 0 1];
G(5,:) = [1 1 0 0 1 0 0 1 1 0];
G(6,:) = [0 0 1 0 1 0 0 0 1 0];
G(7,:) = [1 0 1 1 0 1 1 1 1 1];
G(8,:) = [1 0 0 0 0 1 0 0 1 0];
G(9,:) = [0 1 0 1 1 1 1 1 1 1];
G(10,:) = [1 0 0 1 0 0 0 0 0 0];
%}

% Save parameters as a structure
% Removed for brevity
```

```matlab
    %%
    % Discretize the detector plane , D.
    %    1600x1600 = ten times actual resolution
62  % DetResFact = the resolution of the simulated detector plane , D, ...
        relative
    % to the actual detector   subpixel resolution

    D = zeros(DetZDim*DetUnitFact*DetResFact,DetYDim*DetUnitFact*...
        DetResFact);
    S = zeros(SourceZDim*SourceResFact,SourceYDim*SourceResFact);
67
    troubcount = 0;

    NumSrcRow = numel(S(:,1));
    NumSrcCol = numel(S(1,:));
72  NumDetRow = numel(D(:,1));
    NumDetCol = numel(D(1,:));
    A_NParam = 25600;
    A_MParam = NumSrcRow*NumSrcCol;
    ForwProbParameters.NumSrcRow = numel(S(:,1));
77  ForwProbParameters.NumSrcCol = numel(S(1,:));
    ForwProbParameters.NumDetRow = numel(D(:,1));
    ForwProbParameters.NumDetCol = numel(D(1,:));
    ForwProbParameters.A_NParam = 25600;
    ForwProbParameters.A_MParam = NumSrcRow*NumSrcCol;
82
    clear D S

    today = date;
    filename = [date '_MLEMForwSim_SrcX' num2str(SourceXDist) '_SrcRes...
        ' num2str(SourceResFact) '_Atten' num2str(SteelAtten*100) '_N' ...
        num2str(A_NParam) '_M' num2str(A_MParam) 'MaskNum' num2str(...
        MaskNum)];
87
    fprintf('Computing Forward Problem simulation\n\n')

    A = zeros(A_NParam,A_MParam,'single');

92  for SrcCol = 1:NumSrcCol
    for SrcRow = 1:NumSrcRow
    CurrSrcZPos = SourceZDist+SourceZDim-(SrcRow-1)/SourceResFact-1/...
        SourceResFact/2;    %Find the current source position , in cm
    CurrSrcYPos = SourceYDist+(SrcCol-1)/SourceResFact+1/2/...
        SourceResFact;   % Find the current source position , in cm

97  DetResponse = zeros(NumDetRow,NumDetCol,'single');
    DetResponse2 = zeros(160,160,'single');


    for DetCol = 1:NumDetCol
102 for DetRow = 1:NumDetRow
```

```matlab
    CurrDetZPos = DetZDim - (DetRow -1)/DetUnitFact/DetResFact - 1/2/...
        DetUnitFact/DetResFact;
    CurrDetYPos = (DetCol -1)/DetUnitFact/DetResFact +1/2/DetUnitFact/...
        DetResFact;

    DetToSrcVertAngle = atan2((CurrSrcZPos -CurrDetZPos),SourceXDist);
    DetToSrcHorizAngle = atan2((CurrSrcYPos -CurrDetYPos),SourceXDist);
    CollFrontPlaneVert = CurrSrcZPos - tan(DetToSrcVertAngle)*(...
        SourceXDist -ColXPos -5);
    CollFrontPlaneHoriz = CurrSrcYPos - tan(DetToSrcHorizAngle)*(...
        SourceXDist -ColXPos -5);
    CollRearPlaneVert = CurrSrcZPos - tan(DetToSrcVertAngle)*(...
        SourceXDist -ColXPos);
    CollRearPlaneHoriz = CurrSrcYPos - tan(DetToSrcHorizAngle)*(...
        SourceXDist -ColXPos);

    CollFrontRow = 10-floor((CollFrontPlaneVert -ColZPos)*2);     % ...
        Collimator row that gamma goes through, front
    CollFrontCol = ceil((CollFrontPlaneHoriz -ColYPos)*2);  %Collimator...
         column that gamma goes through, front
    CollRearRow = 10-floor((CollRearPlaneVert -ColZPos)*2);     % ...
        Collimator row that gamma goes through, rear
    CollRearCol = ceil((CollRearPlaneHoriz -ColYPos)*2);  %Collimator ...
        column that gamma goes through, rear

    SameChamber = 0;
    inside = 1;

    % See if gamma travels through the same chamber, from src
    % to det
    if (CollFrontRow == CollRearRow) && (CollFrontCol == CollRearCol)
    SameChamber = 1;
    end

    %Check to see if gamma is within collimator
    if (CollFrontRow > 10)
    inside = 0;
    end
    if (CollFrontRow < 1)
    inside = 0;
    end
    if (CollFrontCol > 10)
    inside = 0;
    end
    if (CollFrontCol < 1)
    inside = 0;
    end
    if (CollRearRow > 10)
    inside = 0;
    end
```

```matlab
    if (CollRearRow < 1)
    inside = 0;
147 end
    if (CollRearCol > 10)
    inside = 0;
    end
    if (CollRearCol < 1)
152 inside = 0;
    end

    if (SameChamber == 1) && (inside == 1)
    if G(CollFrontRow,CollFrontCol) == 1
157 CurrSrcDetDist = norm([CurrSrcZPos-CurrDetZPos SourceXDist ...
        CurrSrcYPos-CurrDetYPos]);    %Dist b/t src pix and Det pix, cm
    DetResponse(DetRow,DetCol) = InitCounts/CurrSrcDetDist^2; % 1/r^2 ...
        attenuation of radiation

    end
    else
162 DetResponse(DetRow,DetCol) = 0;
    end

    if (SameChamber == 0) && (inside == 1)
    RowChanges = abs(CollFrontRow - CollRearRow);
167 ColChanges = abs(CollFrontCol - CollRearCol);
    TotalChanges = RowChanges + ColChanges;
    LowRow = min([CollFrontRow CollRearRow]);
    LowCol = min([CollFrontCol CollRearCol]);
    RowsAllOpen = 1;
172 ColsAllOpen = 1;

    for testrow = LowRow:(LowRow+RowChanges)
    if G(testrow,CollFrontCol) == 0
    RowsAllOpen = 0;
177 end
    end
    for testcol = LowCol:(LowCol+ColChanges)
    if G(CollFrontRow,testcol) == 0
    ColsAllOpen = 0;
182 end
    end

    if (TotalChanges ~= 0) && (RowsAllOpen == 1) && (ColsAllOpen == 1)
    CurrSrcDetDist = norm([CurrSrcZPos-CurrDetZPos SourceXDist ...
        CurrSrcYPos-CurrDetYPos]);    %Dist b/t src and Det, cm
187 DetResponse(DetRow,DetCol) = (InitCounts/CurrSrcDetDist^2)*(...
        SteelAtten^TotalChanges); % 1/r^2 attenuation of radiation
    else
    DetResponse(DetRow,DetCol) = 0;
    end

192 end
```

```matlab
    % Turn the dead subpixels separating strips to 0
    if (mod(DetRow/DetResFact ,10) == 0) || (mod(DetCol/DetResFact ,10) ...
        == 0)
197 DetResponse(DetRow ,DetCol) = 0;
    end


    %DetRow
    end
202 % DetCol
    end


    for tempDetRow = 1:160
    for tempDetCol = 1:160
207 DetResponse2(tempDetRow ,tempDetCol) = sum(sum(DetResponse((...
        DetResFact*tempDetRow -(DetResFact -1)):(DetResFact*tempDetRow) ,(...
        DetResFact*tempDetCol -(DetResFact -1)):(DetResFact*tempDetCol)))...
        );
    end
    end


    clear DetResponse
212
    % Remove the corners of the detector (set to zero)
    for tempDetRow = 1:(0.5/8*(8 *DetUnitFact))
    for tempDetCol = 1:(1.5/8*(8 *DetUnitFact))
    DetResponse2(tempDetRow ,tempDetCol)=0;
217 end
    for tempDetCol = 6.5/8*(8 *DetUnitFact):8/8*(8 *DetUnitFact)
    DetResponse2(tempDetRow ,tempDetCol)=0;
    end
    end
222 for tempDetRow = (0.5/8*(8 *DetUnitFact)):(1/8*(8 *DetUnitFact))
    for tempDetCol = 1:(1/8*(8 *DetUnitFact))
    DetResponse2(tempDetRow ,tempDetCol)=0;
    end
    for tempDetCol = 7/8*(8 *DetUnitFact):8/8*(8 *DetUnitFact)
227 DetResponse2(tempDetRow ,tempDetCol)=0;
    end
    end
    for tempDetRow = (1/8*(8 *DetUnitFact)):(1.5/8*(8 *DetUnitFact))
    for tempDetCol = 1:(0.5/8*(8 *DetUnitFact))
232 DetResponse2(tempDetRow ,tempDetCol)=0;
    end
    for tempDetCol = 7.5/8*(8 *DetUnitFact):8/8*(8 *DetUnitFact)
    DetResponse2(tempDetRow ,tempDetCol)=0;
    end
237 end
    for tempDetRow = (7.5/8*(8 *DetUnitFact)):(8/8*(8 *DetUnitFact))
    for tempDetCol = 1:(1.5/8*(8 *DetUnitFact))
    DetResponse2(tempDetRow ,tempDetCol)=0;
```

```
     end
242  for  tempDetCol  =  6.5/8*(8 *DetUnitFact):8/8*(8 *DetUnitFact)
     DetResponse2(tempDetRow,tempDetCol)=0;
     end
     end
     for  tempDetRow  =  (7/8*(8 *DetUnitFact)):(7.5/8*(8 *DetUnitFact))
247  for  tempDetCol  =  1:(1/8*(8 *DetUnitFact))
     DetResponse2(tempDetRow,tempDetCol)=0;
     end
     for  tempDetCol  =  7/8*(8 *DetUnitFact):8/8*(8 *DetUnitFact)
     DetResponse2(tempDetRow,tempDetCol)=0;
252  end
     end
     for  tempDetRow  =  (6.5/8*(8 *DetUnitFact)):(7/8*(8 *DetUnitFact))
     for  tempDetCol  =  1:(0.5/8*(8 *DetUnitFact))
     DetResponse2(tempDetRow,tempDetCol)=0;
257  end
     for  tempDetCol  =  7.5/8*(8 *DetUnitFact):8/8*(8 *DetUnitFact)
     DetResponse2(tempDetRow,tempDetCol)=0;
     end
     end
262
     AColNum  =  (SrcCol-1)*NumSrcRow+SrcRow;
     A(:,AColNum) =  reshape(DetResponse2,25600,1);

     clear DetResponse2
267

     end
     clc
     fprintf('Computing forward problem simulation.\n\nPercent complete...
         : %.2f',(SrcCol/NumSrcCol*100))
272
     end

     Normalize = max(max(A));
     A = A./Normalize;
277
     save(filename,'A','ForwProbParameters','-v7.3')

     toc
```

Listing A.3.

```
% ML-EM algorithm for the Programmable Collimator as a Coded ...
    Aperture
% Use with output from "ProgCollCodAp_ForwProbSimForMLEM_Try3.m"
% Include "RMC_MLEM", from Ben Kowash, in directory
% 2d Lt Jack FitzGerald, AFIT/ENP, 05DEC11
5
clear all
close all
clc
```

```matlab
10 NumIter = 100;    % Number of iterations in the ML-EM algorithm

   ForwFilename = '15-Dec -2011...
      _MLEMForwSim_SrcX76_SrcRes5_Atten93_N25600_M10000';
   load(ForwFilename);
   M = ForwProbParameters.A_MParam; % Number of source pixels
15 N = ForwProbParameters.A_NParam; % Number of detector pixels

   % ensure that A is normalized
   if max(max(A)) > 1
   norm = max(max(A));
20 A = A./norm;
   end

   % Load the raw data
   filename = '111214_Config1_Co57RodCo60Point_6hrs';
25 extension = '.txt';
   Raw = load([filename,extension]);
   Raw = rot90(Raw,3);
   Raw = fliplr(Raw);

30 % create the ML-EM variables
   lam = ones(M,1); %initial estimate of source plane, all ones
   y = reshape(Raw,numel(Raw),1);  % Raw data, 1xN array
   b = 1;     %uncorrelated background noise, per subpixel
   %a = A' * ones(N,1); % Normalization parameter for A
35
   clc
   fprintf('Parameters loaded. Beginning ML-EM iterative sequence\n\n...
      ')

   FigCount = 1;
40 for i = 1:NumIter
   lam = RMC_MLEM(lam, A, y, b, a);

   if mod(i,round(NumIter/25)) == 0
   fprintf('\nIterative sequence %.0f percent complete',i/NumIter...
      *100);
45 end
   end
```

<div align="center">

Listing A.4.

</div>

```matlab
   function lam_new = RMC_MLEM(lam_old, A, y, b, a)
   % Title: RMC ML-EM routine
   %
 4 % By: Ben Kowash
   % Date: 15 Oct 07
   %
   % Description: This routine takes input data and computes the ...
      estimate
```

```
   % lambda_new based on the properties of the system.  The method ...
      used is a
 9 % maximum-liklihood expectation-maximum iterative algorithm.
   lam_new = lam_old .* (A' * (y ./ (A * lam_old + b))) ./ a;
```

1.3   Coded-Aperture Decorrelation Code

Listing A.5.

```
   % Coded Aperture Decorrelation Code
   % 2d Lt Jack FitzGerald, AFIT/ENP, 21NOV11

 5 % updated on 02JAN11
   % This version includes the magnification of the shadow

   clear variables
   close all
10 clc

   % Input the matched filter

   G(1,:) = [0 1 0 1 1 1 1 0 1 1];
15 G(2,:) = [1 0 0 0 0 1 0 0 1 1];
   G(3,:) = [0 1 1 0 0 1 0 0 0 1];
   G(4,:) = [0 1 0 0 1 0 1 1 1 0];
   G(5,:) = [1 0 1 1 0 1 1 0 0 0];
   G(6,:) = [1 1 0 1 0 0 1 0 0 1];
20 G(7,:) = [0 0 0 0 0 0 1 0 0 0];
   G(8,:) = [1 1 1 1 0 0 1 1 0 0];
   G(9,:) = [1 0 1 1 0 0 0 1 1 0];
   G(10,:) = [1 1 1 0 1 1 1 1 1 1];

25 %% Try using raw, subpixel data
   filename = '111121_Co57_Config3_Pos1_1200sec';
   extension = '.txt';

   % load and plot the raw data
30 RawSub = load([filename,extension]);
   RawSub = rot90(RawSub,3);
   RawSub = fliplr(RawSub);

   %increase res for raw image
35 ResFactorR = 5;

   MaskDetDist = 8; %dist from mask to detector, cm
   MaskSrcDist = 52.6; %dist from mask to source, cm
   %MaskDetDist = 8; %dist from mask to detector, cm
40 %MaskSrcDist = 22.3; %dist from mask to source, cm
   M = (MaskDetDist+MaskSrcDist)/MaskSrcDist;

   for i = 1:160*ResFactorR
   for j = 1:160*ResFactorR
```

```
45 RawSub2(i,j) = RawSub(ceil(i/ResFactorR),ceil(j/ResFactorR));
   end
   end
   RawSub = RawSub2;
   clear RawSub2
50
   MaskElPix = round(10*M*ResFactorR); %Number of detector pixels the...
       shadow of one mask element will contain

   for i = 1:10*MaskElPix
   for j = 1:10*MaskElPix
55 GSub(i,j) = G(ceil(i/MaskElPix),ceil(j/MaskElPix));

   if GSub(i,j) == 0
   GSubBrown(i,j) = -1;
   else
60 GSubBrown(i,j) = 1;
   end
   end
   end

65 GSubCorrRawSub = xcorr2(GSub,RawSub);
   GCorrRWidth = numel(GSubCorrRawSub(1,:));
   lobesize = ((GCorrRWidth)-numel(RawSub(1,:)))/2;
   OHat = GSubCorrRawSub(round(lobesize):round(GCorrRWidth-lobesize),...
       round(lobesize):round(GCorrRWidth-lobesize));
   OHat = OHat ./ norm(norm(OHat));
70
   DecorrAxes = 1:numel(OHat(1,:));
   DecorrAxes = DecorrAxes ./ ResFactorR ./ 20;

   GCorrRBrown = xcorr2(GSubBrown,RawSub);
75 GCorrRBrnWid = numel(GCorrRBrown(1,:));
   lobesizeB = ((GCorrRBrnWid)-numel(RawSub(1,:)))/2;
   OHatBrown = GCorrRBrown(round(lobesizeB):round(GCorrRBrnWid-...
       lobesizeB),round(lobesizeB):round(GCorrRBrnWid-lobesizeB));
   OHatBrown = OHatBrown ./ norm(norm(OHatBrown));
```

1.4   MCNP Code

Listing A.6.

```
1 % MCNP Input File Generator
  % 2d Lt Jack FitzGerald, 27JULY11, AFIT/ENP/GNE
  % Thesis Work
  % Program to make an MCNP simulation of the dynamic, coded ...
      aperture
  % apparatus.
6 % Updated 19DEC11

  clear variables
  close all
  clc
```

```matlab
11
   filename = 'MCNPSimInput';
   extension = '.txt';
   fid = fopen([filename extension],'w');
   fprintf(fid,[filename '\n']);
16
   NumParticles = 100000;

   % Position of source and collimator, using "conventional" scheme ...
      used thus
   % far in testing
21 % Units in cm
   coll_x = 15;     % from detector plane to front of collimator
   coll_y = 1.5;
   coll_z = 1.5;
   src_x_conv = 75;
26 src_y_conv = 4;
   src_z_conv = 4;

   det_thick = 1;  % detector crystal thickness, cm
   det_height = 8;
31 det_width = 8;
   det_pixheight = 0.05; % detector pixel height
   det_pixwidth = 0.05; % detector pixel width

   %The mask configuration, hard coded for now
36 %1 means open to gammas, 0 means closed to gammas
   maskconfig(1,:) = [0 1 0 1 1 1 1 0 1 1];
   maskconfig(2,:) = [1 0 0 0 0 1 0 0 1 1];
   maskconfig(3,:) = [0 1 1 0 0 1 0 0 0 1];
   maskconfig(4,:) = [0 1 0 0 1 0 1 1 1 0];
41 maskconfig(5,:) = [1 0 1 1 0 1 1 0 0 0];
   maskconfig(6,:) = [1 1 0 1 0 0 1 0 0 1];
   maskconfig(7,:) = [0 0 0 0 0 0 1 0 0 0];
   maskconfig(8,:) = [1 1 1 1 0 0 1 1 0 0];
   maskconfig(9,:) = [1 0 1 1 0 0 0 1 1 0];
46 maskconfig(10,:) = [1 1 1 0 1 1 1 1 1 1];
   maskconfig = flipud(maskconfig);

   %% Convert src, collimator and detector positions
   det_x = -coll_y;
51 det_y = -coll_z;
   det_z = -coll_x;
   src_z = src_x_conv - coll_x;
   src_y = src_z_conv - coll_z;
   src_x = src_y_conv - coll_y;
56
   %% Define the cells ...
      ----------------------------------------------------

   %Regions of apparatus != grid block
   fprintf(fid,'1 2 -9.38 -1 5 10 -11 110 -13 IMP:P=1\n');
```

```matlab
61 fprintf(fid,'2 2 -9.38 -1 5 10 -200 100 -110 IMP:P=1\n');
   fprintf(fid,'3 2 -9.38 -1 5 210 -11 100 -110 IMP:P=1\n');
   fprintf(fid,'4 2 -9.38 -1 5 10 -11 12 -100 IMP:P=1\n');

   i=1;
66
   for j = 0:9
   for k = 0:9

   if maskconfig(j+1,k+1) == 0
71 mat = 3;  %material number for PEEK
   dens = -1.32; %g/cm^3
   else
   mat = 1;  % material number for air
   dens = -0.001293;  %g/cm^3
76 end

   if j == 9
   if k == 9
   fprintf(fid,'%i%i%i %i %1.6f -%i %i 10%i -1%i 20%i -2%i IMP:P=1\n'...
       ...
81 ,i,j,k,mat,dens,i,(i+1),j,(j+1),k,(k+1)) ;
   else
   fprintf(fid,'%i%i%i %i %1.6f -%i %i 10%i -1%i 20%i -20%i IMP:P=1\n...
       ' ...
   ,i,j,k,mat,dens,i,(i+1),j,(j+1),k,(k+1)) ;
   end
86 else
   if k == 9
   fprintf(fid,'%i%i%i %i %1.6f -%i %i 10%i -10%i 20%i -2%i IMP:P=1\n...
       ' ...
   ,i,j,k,mat,dens,i,(i+1),j,(j+1),k,(k+1)) ;
   else
91 fprintf(fid,'%i%i%i %i %1.6f -%i %i 10%i -10%i 20%i -20%i IMP:P=1\...
       n' ...
   ,i,j,k,mat,dens,i,(i+1),j,(j+1),k,(k+1)) ;
   end
   end
   end
96 end

   i=2;

   for j = 0:9
101 for k = 0:9

   if maskconfig(j+1,k+1) == 0
   mat = 2;  %material number for CerroBEND
   dens = -9.38; %g/cm^3
106 else
   mat = 1;  % material number for air
   dens = -0.001293;  %g/cm^3
```

```matlab
    end

111 if j == 9
    if k == 9
    fprintf(fid,'%i%i%i %i %1.6f -%i %i 10%i -1%i 20%i -2%i IMP:P=1\n'...
        ...
    ,i,j,k,mat,dens,i,(i+1),j,(j+1),k,(k+1));
    else
116 fprintf(fid,'%i%i%i %i %1.6f -%i %i 10%i -1%i 20%i -20%i IMP:P=1\n...
    ' ...
    ,i,j,k,mat,dens,i,(i+1),j,(j+1),k,(k+1));
    end
    else
    if k == 9
121 fprintf(fid,'%i%i%i %i %1.6f -%i %i 10%i -10%i 20%i -2%i IMP:P=1\n...
    ' ...
    ,i,j,k,mat,dens,i,(i+1),j,(j+1),k,(k+1)) ;
    else
    fprintf(fid,'%i%i%i %i %1.6f -%i %i 10%i -10%i 20%i -20%i IMP:P=1\...
        n' ...
    ,i,j,k,mat,dens,i,(i+1),j,(j+1),k,(k+1)) ;
126 end
    end
    end
    end

131 i=3;

    for j = 0:9
    for k = 0:9

136 if maskconfig(j+1,k+1) == 0
    mat = 2;  %material number for CerroBEND
    dens = -9.38; %g/cm^3
    else
    mat = 3;  % material number for PEEK
141 dens = -1.32;  %g/cm^3
    end

    if j == 9
    if k == 9
146 fprintf(fid,'%i%i%i %i %1.6f -%i %i 10%i -1%i 20%i -2%i IMP:P=1\n'...
        ...
    ,i,j,k,mat,dens,i,(i+1),j,(j+1),k,(k+1)) ;
    else
    fprintf(fid,'%i%i%i %i %1.6f -%i %i 10%i -1%i 20%i -20%i IMP:P=1\n...
    ' ...
    ,i,j,k,mat,dens,i,(i+1),j,(j+1),k,(k+1)) ;
151 end
    else
    if k == 9
```

```matlab
        fprintf(fid,'%i%i%i %i %1.6f -%i %i 10%i -10%i 20%i -2%i IMP:P=1\n...
            ' ...
        ,i,j,k,mat,dens,i,(i+1),j,(j+1),k,(k+1)) ;
156 else
        fprintf(fid,'%i%i%i %i %1.6f -%i %i 10%i -10%i 20%i -20%i IMP:P=1\...
            n' ...
        ,i,j,k,mat,dens,i,(i+1),j,(j+1),k,(k+1)) ;
        end
        end
161 end
        end

        i=4;

166 for j = 0:9
        for k = 0:9

        mat = 3;  %material number for PEEK
        dens = -1.32; %g/cm^3
171
        if j == 9
        if k == 9
        fprintf(fid,'%i%i%i %i %1.6f -%i %i 10%i -1%i 20%i -2%i IMP:P=1\n'...
            ...
        ,i,j,k,mat,dens,i,(i+1),j,(j+1),k,(k+1)) ;
176 else
        fprintf(fid,'%i%i%i %i %1.6f -%i %i 10%i -1%i 20%i -20%i IMP:P=1\n...
            ' ...
        ,i,j,k,mat,dens,i,(i+1),j,(j+1),k,(k+1));
        end
        else
181 if k == 9
        fprintf(fid,'%i%i%i %i %1.6f -%i %i 10%i -10%i 20%i -2%i IMP:P=1\n...
            ' ...
        ,i,j,k,mat,dens,i,(i+1),j,(j+1),k,(k+1));
        else
        fprintf(fid,'%i%i%i %i %1.6f -%i %i 10%i -10%i 20%i -20%i IMP:P=1\...
            n' ...
186 ,i,j,k,mat,dens,i,(i+1),j,(j+1),k,(k+1));
        end
        end
        end
        end
191
        mat = 4;    %mat number for Ge
        dens = -5.232;   %g/cm^3

        % Define the detector cells
196 for col = 1:160
        for row = 1:160
        fprintf(fid,'%05.0f 0 -6 7 %i %i %i %i IMP:P=1\n',((col-1)*160+row...
            +10000),-(row-1+2000),(row-1+2001),(col-1+1000),-(col-1+1001));
```

124

```matlab
        end
    end
201
    % Cell inside the universe sphere
    %fprintf(fid,'997 1 -0.001293 -1999 8 #(-1 5 10 -11 12 -13) IMP:P...
        =1\n'); %Air
    %fprintf(fid,'998 1 -0.001293 -1999 -8 #(-6 7 1000 -1160 -2000 ...
        2160) IMP:P=1\n'); % vacuum
    fprintf(fid,'997 0 -1999 8 #(-1 5 10 -11 12 -13) IMP:P=1\n');
206 fprintf(fid,'998 0 -1999 -8 #(-6 7 1000 -1160 -2000 2160) IMP:P=1\...
        n');

    %Cell outside the universe sphere
    fprintf(fid,'999 0 1999 IMP:P=0\n');

211 fprintf(fid,'\n');


    %% Block 2, define the surfaces ...
        -----------------------------------------

216 %Planes for the PEEK or CerroBEND limits in z
    fprintf(fid,'1 pz 0\n');
    fprintf(fid,'2 pz -1\n');
    fprintf(fid,'3 pz -4.5\n');
    fprintf(fid,'4 pz -5.5\n');
221 fprintf(fid,'5 pz -6\n');
    fprintf(fid,'6 pz %s\n',num2str(det_z + det_thick/2 ));
    fprintf(fid,'7 pz %s\n',num2str(det_z - det_thick/2));
    fprintf(fid,'8 pz %s\n',num2str(det_z + det_thick/2 + 0.5));

226 %Planes for the outer edges of the apparatus
    fprintf(fid,'10 px -5\n');
    fprintf(fid,'11 px 10\n');
    fprintf(fid,'12 py -5\n');
    fprintf(fid,'13 py 10\n');
231
    % form the planes that make the grid block
    for i = 100:110
    fprintf(fid,'%i py %.1f\n',i,((i-100)*0.5));
    end
236
    for i = 200:210
    fprintf(fid,'%i px %.1f\n',i,((i-200)*0.5));
    end

241 % form the planes of the detector
    for i = 1000:1160
    fprintf(fid,'%i px %.2f\n',i,(det_x+(i-1000)*det_pixwidth));
    end

246 for i = 2000:2160
```

```matlab
    fprintf(fid,'%i py %.2f\n',i,(det_y+det_height-(i-2000)*...
        det_pixheight));
    end

    %Define the universe sphere, radius 300
251 fprintf(fid,'1999 so 200 $universe sphere\n');

    fprintf(fid,'\n');


256 % Block 3, Data Specs...
        ------------------------------------------------------
    fprintf(fid,'mode p\n');

    %Define the air, material 1
    fprintf(fid,'m1 7000 -0.78 $ Nitrogen\n'); %Nitrogen, by atom ...
        fraction
261 fprintf(fid,'     8000 -0.22 $ Oxygen\n'); %Oxygen, by atom ...
        fraction

    %Define the CerroBEND, material 2, from wiki, "wood's metal"
    fprintf(fid,'m2 83000 -0.500 $ bismuth\n'); %bismuth, by atom ...
        fraction
    fprintf(fid,'     82000 -0.267 $ oxygen\n'); % lead, by atom ...
        fraction
266 fprintf(fid,'     50000 -0.133 $ tin\n'); % tin, by atom fraction
    fprintf(fid,'     48000 -0.100 $ cadmium\n'); % cadmium, by atom ...
        fraction

    %Define the PEEK
    fprintf(fid,'m3 6000 -0.7889 $ Carbon\n'); %carbon, by atom ...
        fraction
271 fprintf(fid,'     8000 -0.1661 $ Oxygen\n');  %oxygen, by atom ...
        fraction
    fprintf(fid,'     1000 -0.045 $ Hydrogen\n');

    %Define the Germanium
    fprintf(fid,'m4 32000 -1 $ Germanium\n');    %Germanium
276
    %define the source
    %fprintf(fid,'sdef pos %f %f %f par=2 erg=.122\n',src_x,src_y,srcz...
        ); % point isotropic

    % source emitting cone into collimator
281 fprintf(fid,'sdef pos %f %f %f par=2 erg=.122\n',src_x,src_y,src_z...
        );
    vec_x = 2.5 - src_x;
    vec_y = 2.5 - src_y;
    vec_z = 0 - src_z;
    fprintf(fid,'     VEC=%f %f %f DIR=d1\n',vec_x,vec_y,vec_z);
286 cone_rad = 7; %cm of cone
    theta = atan(cone_rad/src_z);
```

```matlab
   fprintf(fid,'SI1 -1 %f 1\n',cos(theta));
   fprintf(fid,'SP1 0 %f %f\n',1-2*pi*(1-cos(theta))/4/pi,2*pi*(1-cos...
      (theta))/4/pi);
   fprintf(fid,'SB1 0. 0. 1.\n');

   %define the number of particles
   fprintf(fid,'nps %i\n',NumParticles);

   %kill photons with energy less than 117 keV
   fprintf(fid,'CUT:p j 0.117\n');

   %define the PTRAC
   fprintf(fid,'PTRAC FILTER=.117,.127,ERG EVENT=SUR MAX=1000000000\n...
      ');
   fprintf(fid,'        FILE=ASC WRITE=POS TYPE=P CELL=10001,\n        ')...
      ;

   for i=10001:35599

   if mod(i,10) == 0
   fprintf(fid,'\n');
   fprintf(fid,'        ');
   end
   fprintf(fid,'%i,',i);
   end

   fprintf(fid,'35600');

   clc
   fprintf(['Finished writing to file: ' filename extension '\n']);

   fclose('all');
```

Listing A.7.

```matlab
   % PTRAC Reader for Coded Aperture Forward Problem Simulation
   % 2d Lt Jack FitzGerald, AFIT/ENP, 19DEC11

   clear all
   close all
   clc

   fid = fopen('ptrac_6','r');
   HistList = zeros(35600,1);

   for i = 1:2571  %skip the header
   line = fgetl(fid);
   end

   eventcount = 0;

   while ischar(line)  %check to see if the line has characters
   if strcmp(line(7:11),' 3000')
```

```matlab
       eventcount = eventcount + 1;
       CellNum = str2double(line(46:51));    % Find the cell number for ...
           the event
       CellList(eventcount) = CellNum;
       end

       if strcmp(line(17:21),' 3000') == 1
       for i = 1:eventcount
       HistList(CellList(i)) = HistList(CellList(i)) + 1/eventcount;    % ...
           weight the hist by number of events in history
       end
       eventcount = 0;
       clear CellList
       end
       line = fgetl(fid);
       end
       fclose('all')

       HistList2 = HistList(10001:35600);
```

Bibliography

[1] "The Third Small Astronomy Satellite", 2003. URL http://heasarc.nasa.gov/docs/sas3/sas3.html.

[2] Ables, J. G. "Fourier transform photography: a new method for X-ray astronomy". *Proceedings of the Astronomical Society of Australia*, 1:172, December 1968. URL http://adsabs.harvard.edu/abs/1968PASAu...1..172A.

[3] Accorsi, R. and R.C. Lanza. "High-sensitivity dynamic coded aperture imaging". *Nuclear Science Symposium Conference Record, 2003 IEEE*, volume 3, 1833 – 1837. oct. 2003.

[4] Accorsi, Roberto, Luigi Celentano, Paolo Laccetti, Richard C. Lanza, Marcello Marotta, Giovanni Mettivier, Maria Cristina Montesi, Giuseppe Roberti, and Paolo Russo. "High-resolution 125i small animal imaging with a coded aperture and a hybrid pixel detector". *IEEE Transactions on Nuclear Science*, 55(1):481 – 490, 2008.

[5] Accorsi, Roberto, Francesca Gasparini, and Richard C. Lanza. "Optimal Coded Aperture Patterns for Improved SNR in Nuclear Medicine Imaging". *Nuclear Instruments and Methods in Physics Research A*, 474:273–284, 2001.

[6] Alloys, HiTech. "HiTech Alloy Products", 2003. URL http://hitechalloys.com/hitechalloys_002.htm.

[7] Arendtsz, N.V. and E.M.A. Hussein. "Energy-spectral Compton scatter imaging. I. Theory and mathematics". *IEEE Transactions on Nuclear Science*, 42(6):2155 – 2165, 1995.

[8] AS and E. "Z Backscatter: Power, Effectiveness and Safety", 2011. URL http://www.as-e.com/products_solutions/z_backscatter.asp.

[9] Barrett, Harrison H. and William Swindell. *Radiological Imaging*. Academic Press, second edition, 1981.

[10] Brown, Christopher M. *Multiplex Imaging with Random Arrays*. Ph.D. thesis, University of Chicago, Dec. 1972.

[11] Burks, M., E. Jordan, E. Hull, L. Mihailescu, and K. Vetter. "Signal Interpolation in Germanium Detectors for Improved 3-D Position Resolution". *2004 IEEE Nuclear Science Symposium Conference Record (Italy)*. 2004.

[12] Calabro, D. and J. K. Wolf. "On Synthesis of Two-Dimensional Arrays with Desirable Correlation Properties". *Information and Control*, 11:537–560, Nov. 1967.

[13] Castings, Alchemy. "Bismuth Alloys, Cerro Alloys", 2011. URL http://alchemycastings.com/lead-products/fusible.htm.

[14] Choi, Kerkil and David J. Brady. "Coded aperture computed tomography". *Proceedings of SPIE - The International Society for Optical Engineering*, 7468, 2009.

[15] Clarke, R. L., E. N. C. Milne, and G. Van Dyk. "The use of Compton-scattered gamma-rays for tomography". *Investigated Radiology*, 11:225–235, 1976.

[16] Clinthorne, N.H., W.L. Rogers, Zhong He, and D.K. Wehe. "Time-coded apertures for imaging in high-background environments". *Nuclear Science Symposium and Medical Imaging Conference Record, IEEE*, 70–74. oct 1995.

[17] Cook, W. R., M. Finger, T. A. Prince, and E. C. Stone. "Gamma-Ray Imaging with a Rotating Hexagonal Uniformly Redundant Array". *IEEE Transactions on Nuclear Science*, NS-31(1):771–775, 1984.

[18] Cubesat. "CubeSat in the News", 2012. URL http://www.cubesat.org/.

[19] Cunningham, M.F., E. Blakeman, L. Fabris, F. Habte, and K. Ziock. "Active-mask coded-aperture imaging". *Nuclear Science Symposium Conference Record, 2007. NSS '07. IEEE*, volume 2, 1217 –1221. 2007.

[20] Deslattes, R.D., E.G. Kessler Jr., P. Indelicato, L. de Billy, E. Lindroth, J. Anton, J.S. Coursey, D.J. Schwab, J. Chang, R. Sukumar, K. Olsen, and R.A. Dragoset. "X-ray transition energies: new approach to a comprehensive evaluation". *Reviews of Modern Physics*, 2003. URL http://www.nist.gov/pml/data/xraytrans/index.cfm.

[21] Dicke, R. H. "Scatter-Hole Cameras for X-Rays and Gamma Rays". *The Astrophysical Journal*, 153:101, August 1968. URL http://adsabs.harvard.edu/abs/1968ApJ...153L.101D.

[22] Driol, Clemence, Mai K. Nguyen, and Tuong T. Truong. "Modeling and Simulation Results on High Sensitivity Scattered Gamma-Ray Emission Imaging". *Simulation Modelling Practice and Theory*, 16:1067–1076, 2008.

[23] Driol, Clemence, M.K. Nguyen, and T.T. Truong. "On high sensitivity emission imaging by scattered gamma radiation". *Annual International Conference of the IEEE Engineering in Medicine and Biology - Proceedings*, 759–762. 2007.

[24] Eckhardt, Roger. "Stan Ulam, John von Neumann, and the Monte Carlo method". *Los Alamos Science*, 15:131–137, 1987.

[25] Evans, B. L. *Fan-Beam Multiplexed Compton Scatter Tomography for Single-Sided Noninvasive Inspection*. Ph.D. thesis, Air Force Institute of Technology, 1999.

[26] Fenimore, E.E. and T.M. Cannon. "Coded aperture imaging with uniformly redundant arrays." *Applied Optics*, 17(3):337 – 347, 1978.

[27] Gottesman, S. R. "Coded apertures: past, present, and future application and design". *Society of Photo-Optical Instrumentation Engineers (SPIE) Conference Series*, volume 6714 of *Society of Photo-Optical Instrumentation Engineers (SPIE) Conference Series*. October 2007.

[28] Guerin, Bastien and Georges El Fakhri. "Novel Scatter Compensation of List-Mode PET Data Using Spatial and Energy Dependent Corrections". *IEEE Transactions on Medical Imaging*, 30(3), 2011.

[29] Hansen, William L. and Eugene E. Haller. "Amorphous Germanium as an Electron or Hole Blocking Contact on High-Purity Germanium Detectors". *Nuclear Science, IEEE Transactions on*, 24(1):61 –63, feb. 1977.

[30] Harding, G. and E. Harding. "Compton Scatter Imaging: A tool for historical exploration". *Applied Radiation and Isotopes*, 68:993–1005, 2010.

[31] Holman, Gordon D. *Overview of Solar Flares*. Technical report, NASA: RHESSI, 2008. URL http://hesperia.gsfc.nasa.gov/hessi/flares.htm.

[32] Holman, Gordon D. "RHESSI Home Page", 2010. URL http://hesperia.gsfc.nasa.gov/hessi/.

[33] Hong, Baoming, Zhiping Mu, and Yi-Hwa Liu. "A new approach of 3D SPECT reconstruction for near-field coded aperture imaging". *Progress in Biomedical Optics and Imaging - Proceedings of SPIE*, volume 6142 III, SPIE –. 2006.

[34] Hubbell, J. H. and S. M. Seltzer. *Tables of X-Ray Mass Attenuation Coefficients and Mass Energy-Absorption Coefficients from 1 keV to 20 MeV for Elements Z = 1 to 92 and 48 Additional Substances of Dosimetric Interest*. Technical report, Ionizing Radiation Division, Physics Laboratory, NIST, 1996. URL http://www.nist.gov/pml/data/xraycoef/index.cfm.

[35] Hull, Ethan L. and Richard H. Pehl. "Amorphous germanium contacts on germanium detectors". *Nuclear Instruments and Methods in Physics Research, Section A: Accelerators, Spectrometers, Detectors and Associated Equipment*, 538(1-3):651 – 656, 2005.

[36] Hussein, E. M. A., D. A. Meneley, and S. Banerjee. "On the solution of inverse problem of radiation scatter imaging". *Nucl. Sci. Eng.*, 92(1):341–349, 1986.

[37] Knoll, Glenn F. *Radiation Detection and Measurement*. John Wiley and Sons, Inc., fourth edition, 2010.

[38] Kowash, Benjamin R. "Coded Aperture Analysis Tool", 2011. MATLAB code.

[39] Lale, P. G. "The examination of internal tissues, using gamma-ray scatter with a possible extension to megavoltage radiography." *Phys. Med. Bio.*, 4:159–167, 1959.

[40] Lange, K. and R. Carson. "EM Reconstruction Algorithms for Emission and Transmission Tomography". *J. Comput. Assist. Tomogr.*, 8:306–316, 1984.

[41] Lange, Matthew A. *Single-sided nonivasive inspection of multielement sample using fan-beam multiplexed compton scatter tomography.* Master's thesis, Air Force Institute of Technology, 2001.

[42] Lee, Wonho, Taewoong Lee, Manhee Jeong, and Ho Kyung Kim. "Evaluation of dual -ray imager with active collimator using various types of scintillators". *Applied Radiation and Isotopes*, 69(10):1560 – 1567, 2011.

[43] Limited, Barnard Microsystems. "Nuclear Radiation Monitoring Using Unmanned Aircraft", 2011. URL http://www.barnardmicrosystems.com/L4E_gamma_ray.htm.

[44] Luke, P.N., C.P. Cork, N.W. Madden, C.S. Rossington, and M.F. Wesela. "Amorphous Ge bipolar blocking contacts on Ge detectors." *IEEE Transactions on Nuclear Science*, 39(4):590 – 594, 1992.

[45] Macrander, Albert T., Hanfei Yan, Hyon Chol Kang, Jorg Maser, Chian Liu, Ray Conley, and G. Brian Stephenson. "Nanofocusing of Hard X-Rays with Multilayer LAUE Lenses". *Handbook of Optics*, 42.1–42.18. McGraw-Hill, 2010. URL http://www.accessengineeringlibrary.com/mghpdf/007173824X_ar042.pdf.

[46] Mattson, Barbara. "Gamma-ray Astronomy Satellites and Missions", 2008. URL http://imagine.gsfc.nasa.gov/docs/sats_n_data/gamma_missions.html.

[47] Meng, L.J. and N.H. Clinthorne. "A modified uniform Cramer-Rao bound for multiple pinhole aperture design". *Medical Imaging, IEEE Transactions on*, 23(7):896 –902, july 2004.

[48] Milne, G. W. A. *Gardner's Chemical Synonyms and Trade Names.* John Wiley and Sons, eleventh edition, 1999.

[49] Monte, E. Del, E. Costa, G. Di Persio, I. Donnarumma, Y. Evangelista, M. Feroci, I. Lapshov, F. Lazzarotto, M. Mastropietro, E. Morelli, L. Pacciani, M. Rapisarda, A. Rubini, P. Soffitta, M. Tavani, A. Argan, and A. Trois. "Rolling and tumbling: status of the SuperAGILE experiment". *Space Telescopes and Instrumentation 2010: Ultraviolet to Gamma Ray*, 7732(1), 2010.

[50] Mu, Zhiping and Yi-Hwa Liu. "Aperture collimation correction and maximum-likelihood image reconstruction for near-field coded aperture imaging of single

photon emission computerized tomography". *Medical Imaging, IEEE Transactions on*, 25(6):701 –711, june 2006.

[51] Nguyen, Mai K., Tuong T. Truong, Clemence Driol, and Habib Zaidi. "On a Novel Approach to Compton Scatter Imaging". *IEEE Transactions on Nuclear Science*, 56(3), 2009.

[52] Nguyen, M.K., R., T.T. Truong, and H. Zaidi. "Compton scattered imaging based on the V-line radon transform and its medical imaging applications". *Engineering in Medicine and Biology Society (EMBC), 2010 Annual International Conference of the IEEE*, 4300 –4303. 2010.

[53] Nuyts, J., C. Michel, and P. Dupont. "Maximum-likelihood expectation-maximization reconstruction of sinograms with arbitrary noise distribution using NEC-transformations". *Medical Imaging, IEEE Transactions on*, 20(5):365 –375, may 2001.

[54] Pavlinsky, M., S. Grebenev, P. Mazov, I. Dekhanov, D. Ryvkin, R. Sunyaev, V. Surtaev, N. Mokrousov, A. Glushenko, S. Yampolskii, and A. Novikov. "The Spin-X wide-field X-ray monitor of the Spectrum-X-Gamma astrophysical observatory". *Astronomy Letters*, 26:779–787, 2000.

[55] Plastics, Boedecker. "PEEK PolyEtherEtherKetone Datasheet", 2011. URL http://www.boedeker.com/peek_p.htm.

[56] Prettyman, T. H., R. P. Gardner, J. C. Russ, and K. Verghese. "A combined transmission and scattering tomographic approach to composition and density imaging". *Appl. Radiat. Isot.*, 4:1327–1341, 1993.

[57] Protic, D. and T. Krings. "Microstructures on Ge detectors with amorphous Ge contacts". *Nuclear Science Symposium Conference Record, 2002 IEEE*, volume 1, 473 – 474 vol.1. nov. 2002.

[58] Rothenbush, F. D. *Improved multinuclide imaging of special nuclear material using a high purity germanium double sided strip detector*. Master's thesis, Air Force Institute of Technology, 2005.

[59] Sands, Marc J. *An investigation into the noninvasive assessment of bone density using Multiplexed Compton Scattered Tomography*. Master's thesis, Air Force Institute of Technology, 1999.

[60] Schanne, S., J.-L. Atteia, D. Barret, S. Basa, M. Boer, B. Cordier, F. Daigne, A. Ealet, P. Goldoni, A. Klotz, O. Limousin, P. Mandrou, R. Mochkovitch, S. Paltani, J. Paul, P. Petitjean, R. Pons, and G. Skinner. "The ECLAIRs micro-satellite for multi-wavelength studies of gamma-ray burst prompt emission". *Nuclear Science Symposium Conference Record, 2004 IEEE*, volume 1, 301 – 308. 2004.

[61] Shepp, L. A., Y. Vardi, J. B. Ra, S. K. Hilal, and Z. H. Cho. "Maximum Likelihood PET with Real Data". *Nuclear Science, IEEE Transactions on*, 31(2):910 –913, april 1984.

[62] Shepp, L. S. and Y. Vardi. "Maximum-Likelihood Reconstruction for Emission Tomography". *IEEE Transactions on Medical Imaging*, MI-1:113–122, 1982.

[63] Shultis, J. K. and R. E. Faw. *An MCNP Primer*. Technical report, Kansas State University, 2006.

[64] Skoog, Douglas A., James F. Holler, and Stanley R. Crouch. *Principles of Instrumental Analysis*. Brooks Cole, 6 edition, 2006.

[65] Smith, Warren E., Harrison H. Barrett, and John N. Aarsvold. "Coded-aperture imaging in nuclear medicine". *NASA, Langley Research Center, Visual Information Processing for Television and Telerobotics*, 33–45, Nov. 1989.

[66] Sponder, L. *An Assessment of COMSCAN, A Compton Backscatter Imaging Camera, for the One-Sided Non-Destructive Inspection of Aerospace Components*. Technical report, Australian Department of Defense Defense Science and Technology Organisation Aeronautical Research Laboratory, 1993.

[67] Stevenson, Alex W. *Improving the Efficiency of Photon Collection By Compton Rescue*. Master's thesis, Air Force Institute of Technology, 2011.

[68] Taylor, John R. *An Introduction to Error Analysis: The Study of Uncertainties in Physical Measurement*. University Science Books, 2 edition, 1997.

[69] Team, X-5 Monte Carlo. *MCNP - A General Monte Carlo N-Particle Transport Code, Version 5*. Technical Report LA-UR-03-1987, Los Alamos National Laboratory, 2005.

[70] Tsoulfanidis, Nicholas and Sheldon Landsberger. *Measurement and Detection of Radiation*. CRC Press, 3 edition, 2010.

[71] Van Giessen, John W., Max A. Viergever, Cornelis N. De Graaf, and Huib J. Dane. "TIME-CODED APERTURE TOMOGRAPHY: EXPERIMENTAL RESULTS." *IEEE Transactions on Medical Imaging*, MI-5(4):222 – 228, 1986.

[72] Vedrenne, Gilbert and Jean-Luc Atteia. *Gamma-Ray Bursts*. Springer, 2009.

[73] Wade, Mark, 2012. URL http://www.astronautix.com/craft/vela.htm.

[74] Willcox, D.T., B.R. Kowash, and D.K. Wehe. "Adaptive imaging using a Rotating Modulation Collimator (RMC)". *Nuclear Science Symposium Conference Record (NSS/MIC), 2010 IEEE*, 1531 –1535. 30 2010-nov. 6 2010.

[75] Williams, Christopher S. *Three Dimensional Positron Annihilation Momentum Measurement Technique Applied to Measure Oxygen-Atom Defects in 6H Silicon Carbide*. Ph.D. thesis, Air Force Institute of Technology, 2010.

[76] Winter, Mark. "WebElements", 2011. URL http://www.webelements.com/mercury/physics.html.

[77] Woods, J. W., M. P. Ekstrom, T. M. Palmieri, and R. E. Twogood. "Best Linear Decoding of Random Mask Images". *Nuclear Science, IEEE Transactions on*, 22(1):379 –383, feb. 1975. ISSN 0018-9499.

[78] Ziock, Klaus-Peter, Chris Boehnen, Jason Hayward, and Ana C. Raffo-Caiado. *A Mechanically-Cooled, Highly-Portable, HPGe-Based, Coded-Aperture Gamma-Ray Imager*. Technical report, Oak Ridge National Laboratory, 2011.

Vita

    2d Lt Jack FitzGerald was born and raised in Wichita, KS. After graduating from the International Baccalaureate program at Wichita High School East, he received an appointment to the United States Air Force Academy. He majored in physics at the Academy, worked on a space-based plasma characterization instrument called WISPERs as part of FalconsSat-5, and was a sailplane instructor pilot for the 94th FTS. After commissioning in May of 2010, he was sent to the Air Force Institute of Technology at Wright-Patterson AFB to be a full-time graduate student. After graduation from AFIT, he will be assigned to the Defense Threat Reduction Agency at Fort Belvoir, near Washington, D.C., where he will serve as a physicist and program manager.

REPORT DOCUMENTATION PAGE

1. REPORT DATE *(DD–MM–YYYY)*	2. REPORT TYPE	3. DATES COVERED *(From — To)*
22–03–2012	Master's Thesis	Aug 2010 — Mar 2012

4. TITLE AND SUBTITLE

A Programmable Liquid Collimator for Both Coded Aperture Adaptive Imaging and Multiplexed Compton Scatter Tomography

5a. CONTRACT NUMBER

5b. GRANT NUMBER

5c. PROGRAM ELEMENT NUMBER

6. AUTHOR(S)

FitzGerald, Jack G. M., 2d Lt, USAF

5d. PROJECT NUMBER

5e. TASK NUMBER

5f. WORK UNIT NUMBER

7. PERFORMING ORGANIZATION NAME(S) AND ADDRESS(ES)

Air Force Institute of Technology
Graduate School of Engineering and Management (AFIT/EN)
2950 Hobson Way
WPAFB OH 45433-7765

8. PERFORMING ORGANIZATION REPORT NUMBER

AFIT/NUCL/ENP/12-M01

9. SPONSORING / MONITORING AGENCY NAME(S) AND ADDRESS(ES)

MAJ Doug Rothenbush
Combating WMD Capabilities Branch, J852, USSTRATCOM
(402) 232-3391, DSN 272-3391, rothenbf@stratcom.mil

10. SPONSOR/MONITOR'S ACRONYM(S)

USSTRATCOM/J852

11. SPONSOR/MONITOR'S REPORT NUMBER(S)

12. DISTRIBUTION / AVAILABILITY STATEMENT

APPROVED FOR PUBLIC RELEASE; DISTRIBUTION UNLIMITED

13. SUPPLEMENTARY NOTES

14. ABSTRACT   A novel, fully reconfigurable collimator device for γ-ray and X-ray imaging was built and tested as a coded aperture. The device consisted of 10x10, 5x5x5 mm^3 chambers. Each chamber either was filled with an attenuating liquid, stopping photons, or evacuated of the attenuating liquid, allowing the photons to pass through. As the pattern of "on" and "off" chambers was manipulated, different, semi-independent views of the γ-ray source were found. Noise in reconstructed images decreased in all tests. Image reconstruction was performed with correlation methods and Maximum Likelihood Expectation Maximization (ML-EM). Using ten mask patterns, the signal-to-noise ratio (SNR) in images of a Co-57 point source increased by a factor of 4.3 using correlation methods and by a factor of at least 50 with ML-EM. SNR in images of a Cd-109 source with high background increased by a factor of 3.0 using correlation methods and by a factor of 1.8 with ML-EM. Two extended sources were imaged, and the images improved when more masks were used. The Multiplexed Compton Scatter Tomography (MCST) forward problem using a PHDs Co high purity germanium (HPGe) detector was tested and evaluated. Potential applications are discussed in detail.

15. SUBJECT TERMS

coded aperture, gamma ray imaging, adaptive imaging, X-ray imaging, Compton scatter, modulation collimator, liquid collimator, programmable collimator, multiplexed Compton scatter tomography, high purity germanium, maximum likelihood, mcnp, ray tracing

16. SECURITY CLASSIFICATION OF:			17. LIMITATION OF ABSTRACT	18. NUMBER OF PAGES	19a. NAME OF RESPONSIBLE PERSON
a. REPORT	b. ABSTRACT	c. THIS PAGE			Dr. Larry Burggraf
U	U	U	U	156	19b. TELEPHONE NUMBER *(include area code)* (937) 255-3636, x4507; larry.burggraf@afit.edu